Rho GTPase signaling and mDia facilitate endocytosis via presynaptic actin

Kristine Oevel[1], Svea Hohensee[1], Atul Kumar[2], Irving Rosas-Brugada[1#], Francesca Bartolini[2], Tolga Soykan[1*], and Volker Haucke[1,3,4*]

[1] Leibniz-Forschungsinstitut für Molekulare Pharmakologie (FMP), 13125 Berlin, Germany.

[2] Department of Pathology and Cell Biology, Columbia University Medical Center, New York, NY 10032, USA.

[3] Faculty of Biology, Chemistry, Pharmacy, Freie Universität Berlin, 14195 Berlin, Germany.

[4] NeuroCure Cluster of Excellence, Charité Universitätsmedizin Berlin, 10117 Berlin, Germany.

*Correspondence: haucke@fmp-berlin.de (V.H.) or soykan@fmp-berlin.de (T.S.).

[#] deceased

ABSTRACT

Neurotransmission at synapses is mediated by the fusion and subsequent endocytosis of synaptic vesicle membranes. Actin has been suggested to be required for presynaptic endocytosis but the mechanisms that control actin polymerization and its mode of action within presynaptic nerve terminals remain poorly understood. We combine optical recordings of presynaptic membrane dynamics and ultrastructural analysis with genetic and pharmacological manipulations to demonstrate that presynaptic endocytosis is controlled by actin regulatory diaphanous-related formins mDia1/3 and Rho family GTPase signaling. We show that impaired presynaptic actin assembly in the near absence of mDia1/3 and reduced RhoA activity is partly compensated by hyperactivation of Rac1. Inhibition of Rac1 signaling further aggravates impaired presynaptic endocytosis elicited by loss of mDia1/3. Our data suggest that interdependent mDia1/3-Rho and Rac1 signaling pathways cooperatively act to facilitate synaptic vesicle endocytosis by controlling presynaptic F-actin.

INTRODUCTION

Synaptic transmission relies on the release of neurotransmitters by calcium-triggered exocytic fusion of synaptic vesicles (SVs) at specialized active zone release sites within presynaptic nerve terminals. Following fusion, compensatory endocytosis retrieves SV proteins and lipids from the presynaptic plasma membrane and SVs are reformed (Chanaday *et al*, 2019; Gan & Watanabe, 2018; Kononenko & Haucke, 2015; Saheki & De Camilli, 2012; Soykan *et al*, 2016), e.g. by clathrin-mediated vesicle budding (Kononenko *et al*, 2014; Watanabe *et al*, 2014) (but see (Wu *et al*, 2014) for evidence in favor of clathrin-independent SV reformation). Endocytosis relies on mechanical forces to enable membrane deformation and eventually fission (Engqvist-Goldstein & Drubin, 2003). In many biological systems, actin and actin-associated myosin motors appear to provide such mechanical force to facilitate vesicle formation (Anes *et al*, 2003; Marston *et al*, 2003). For example, the function of actin for endocytosis is well-established in yeast, whereas differential requirements for actin in distinct forms of endocytosis have been described in various types of mammalian cells including neurons (Boulant *et al*, 2011; Merrifield *et al*, 2005; Saffarian *et al*, 2009; Saheki & De Camilli, 2012). Pharmacological inhibition of actin assembly by latrunculin has been shown to cause the accumulation of endocytic intermediates at lamprey giant synapses (Shupliakov *et al*, 2002) and interfere with ultrafast endocytosis in response to single optical action potentials (APs) at hippocampal synapses (Watanabe *et al*, 2013; Watanabe *et al.*, 2014; Wu & Chan, 2022) and with fast endocytosis at cerebellar mossy fiber boutons (Delvendahl *et al*, 2016). The same treatment does not hamper endocytosis of SV proteins at hippocampal synapses stimulated with trains of APs (Sankaranarayanan *et al*, 2003; Soykan *et al*, 2017). Genetic interference with actin function by conditional knockout (KO) of β- or γ-actin genes has suggested a crucial role for actin in all kinetically distinguishable forms of endocytosis (Wu *et al*, 2016) at hippocampal synapses and the calyx of Held, a fast giant synapse in the auditory

53 brain stem (Borst & Soria van Hoeve, 2012). However, in the same preparations actin loss also
54 affected SV exocytosis (Wu *et al.*, 2016), suggesting a more general requirement of actin for
55 presynaptic function. Consistently, actin has been shown to surround clusters of reserve pool SVs
56 in lamprey (Bloom *et al*, 2003), to facilitate the replenishment of fast releasing vesicles in various
57 models (Sakaba *et al*, 2013; Sakaba & Neher, 2003), to be involved in Tau pathology (Zhou *et al*,
58 2017), to induce spine growth and plasticity, (Cingolani & Goda, 2008) and to steer neuronal
59 migration (Shinohara *et al*, 2012) among various other roles.

60 We have previously demonstrated that pharmacological interference with the function of
61 formins, a group of Rho family-associated proteins that nucleate linear filamentous (F) actin,
62 kinetically delays SV endocytosis at hippocampal boutons and blocks compensatory endocytosis
63 at the calyx of Held in pre-hearing rats (Soykan *et al.*, 2017). Capacitance measurements at the
64 calyx of Held in post-hearing rodents suggest a less stringent requirement for formin-mediated
65 actin assembly for endocytosis (Hori *et al*, 2022). The latter observation may reflect the operation
66 of compensatory pathways for actin assembly, e.g. via Rac1 or Cdc42 Rho-family GTPases that
67 promote branched actin networks (Eisenmann *et al*, 2005; Goode & Eck, 2007; Hodge & Ridley,
68 2016).

69 In contrast to the vast body of literature regarding the role of actin and actin-associated
70 proteins at the postsynapse [(Cingolani & Goda, 2008; Colgan & Yasuda, 2014) and references
71 therein], most notably the actin-rich mesh of the postsynaptic density of glutamatergic synapses,
72 comparably little is known about the signaling pathways (e.g. via guanine nucleotide exchange
73 factors and GTPase activating proteins for Rho family small GTPases (Muller *et al*, 2020)) that
74 mediate actin assembly at the presynapse. Recent work has suggested that presynaptic Rac1
75 negatively regulates synaptic strength and release probability by altering SV priming and
76 replenishment at central synapses (O'Neil *et al*, 2021) including the calyx of Held (Keine *et al*,

77 2022). These data suggest a negative regulatory role for Rac1 in SV exocytosis. The abundance of
78 postsynaptic actin (Chen *et al*, 2020; Cingolani & Goda, 2008; Colgan & Yasuda, 2014) has
79 hampered the analysis of the nanoscale localization of actin at presynaptic nerve terminals and of
80 the actin-regulatory proteins that control its dynamics. KO of Dynamin, the main enzyme for
81 endocytic membrane fission (Ferguson *et al*, 2007; Imoto *et al*, 2022; Raimondi *et al*, 2011), has
82 been shown to cause the accumulation of F-actin at and around stalled endocytic intermediates in
83 non-neuronal cells (Ferguson *et al*, 2009) but this phenotype seems less overt at hippocampal
84 synapses (Raimondi *et al.*, 2011). Hence, actin in addition to a possible local role at endocytic
85 invaginations might serve a more general function in endocytosis at synapses, for example by
86 modulating plasma membrane tension or contractility, by providing a restrictive membrane
87 scaffold that promotes membrane fission by keeping endocytic invaginations under longitudinal
88 tension (Boulant *et al.*, 2011; Roux *et al*, 2006; Wu & Chan, 2022), or via formation of an F-actin
89 ring around the active zone that mechanically couples exocytic membrane compression to
90 endocytic pit formation (Ogunmowo *et al*, 2023).
91 Here we combine optical recordings of SV exo-/ endocytosis and ultrastructural analysis
92 with genetic and pharmacological manipulations to show that interdependent mDia1/3-Rho and
93 Rac1 signaling pathways cooperate to facilitate SV endocytosis by controlling presynaptic F-actin.
94

95 **RESULTS**

96 *Actin dynamics and actin nucleating mDia1/3 proteins facilitate presynaptic endocytosis and SV*
97 *recycling*

98 Previous studies using pharmacological inhibitors of actin polymerization and
99 depolymerization have yielded inconclusive, often conflicting data regarding the function of actin
100 in SV endocytosis and recycling in different models (Bleckert *et al*, 2012; Del Signore *et al*, 2021;

101 Piriya Ananda Babu *et al*, 2020; Sankaranarayanan *et al.*, 2003; Shupliakov *et al.*, 2002; Wu &
102 Chan, 2022). In contrast, genetic ablation of β- or γ-actin genes in mouse neurons suggests that
103 actin is required for all forms of endocytosis at several types of synapses (Wu *et al.*, 2016).
104 Prompted by these findings we revisited the role of actin in presynaptic endocytosis by analyzing
105 the effects of impaired F-actin dynamics in the combined presence of the G-actin sequestering
106 drug latrunculin A, the F-actin stabilizer jasplakinolide, and Y-27632, an inhibitor of ROCK kinase
107 signaling. This cocktail was shown to preserve the existing cytoskeleton architechture while
108 blocking actin assembly, disassembly and rearrangement (Peng *et al*, 2011). We optically recorded
109 the stimulation-induced exo-endocytosis of the SV protein Synaptophysin (Syph) fused to a pH-
110 sensitive super-ecliptic green fluorescent protein (pHluorin) (Miesenbock *et al*, 1998) that is de-
111 quenched during exocytosis and undergoes re-quenching as SVs are internalized and re-acidified
112 in hippocampal neurons at physiological temperature. Under these conditions (i.e. trains of APs,
113 37°C), SV endocytosis occurs on a timescale of > 10 seconds, e.g. a timescale that is slower than
114 re-quenching of pHluorin due to reacidification (Lopez-Hernandez *et al*, 2022; Soykan *et al.*,
115 2017). Hence, the decay of pHluorin signals can serve as a measure of the time course of SV
116 endocytosis. Perturbation of actin dynamics in the combined presence of latrunculin A,
117 jasplakinolide, and Y-27632 significantly slowed down the endocytic retrieval of exogenously
118 expressed Syph-pHluorin (Figure 1A,B). Application of Y-27632 alone or a combination of
119 latrunculin A and jasplakinolide had no effect on SV endocytosis kinetics, whereas combined use
120 of Y-27632 together with jasplakinolide displayed a mild inhibitory effect (Figure 1- Supplement
121 1C-F). Impaired actin dynamics in the presence of latrunculin A, jasplakinolide, and Y-27632 did
122 not impact the apparent level of SV exocytosis indicated by the maximal amplitude of Syph-
123 pHluorin fluorescence (Figure 1-Supplement 1A). As optical imaging of pHluorin reporters may
124 lead to artifacts, we analyzed the internalization kinetics of the endogenous vesicular γ-

125 aminobutyric acid transporter (vGAT) using antibodies directed against its luminal domain
126 coupled to the pH-sensitive fluorophore CypHer5E (Hua *et al*, 2011; Lopez-Hernandez *et al.*,
127 2022). The cyanine-based dye CypHer5E is quenched at neutral pH but exhibits bright
128 fluorescence when present in the acidic lumen of SVs and, thus can serve as a tracer for the exo-
129 endocytic cycling of endogenous SV proteins. Perturbation of actin dynamics significantly delayed
130 the endocytic retrieval of endogenous vGAT in response to train stimulation with 200 APs at
131 physiological temperature (Figure 1C,D), consistent with the results from exogenously expressed
132 Syph-pHluorin. vGAT exocytosis proceeded unperturbed (Figure 1-Supplement 1B). Hence, a
133 dynamic actin cytoskeleton facilitates presynaptic endocytosis in hippocampal neurons.

134 Previous studies have suggested that formins, in particular mDia1, promote SV
135 endocytosis (Soykan *et al.*, 2017), likely by inducing F-actin assembly (Ganguly *et al*, 2015). We
136 confirmed that shRNA-mediated depletion of mDia1 from hippocampal neurons led to
137 significantly delayed Syph-pHluorin endocytosis and re-acidification in response to stimulation
138 with 200 APs. Re-expression of shRNA-resistant wild-type mDia1 fully restored normal
139 endocytosis kinetics (Figure 1E,F). Impaired SV endocytosis in lentivirus-mediated mDia1-
140 depleted neurons (Figure 1-Supplement 1H) was also observed, if SV exo-/ endocytosis was
141 triggered by stimulation with 40 APs or 80 APs and probed with vesicular glutamate transporter 1
142 (vGLUT1)-pHluorin (Figure 1G,H and Figure 1-Supplement 1I,K). Exocytic fusion of vGLUT1-
143 pHluorin-containing SVs was unaffected (Figure 1-Supplement 1G). Co-depletion of the closely
144 related mDia3 isoform tended to further aggravate this phenotype (Figure 1G,H and Figure 1-
145 Supplement 1I,K) without impacting the apparent number of fused SVs (Figure 1- Supplement
146 1J,L), but not vGAT exocytosis (Figure 1-Supplement 1M). Furthermore, mDia1/3 depletion
147 significantly delayed the endocytic retrieval of endogenous vGAT (Figure 1I,J). Conversely,
148 application of IMM-01, a small molecule activator of mDia-related formins that acts by relieving

149 autoinhibition (Lash *et al*, 2013) (Figure 1-Supplement 1N), led to a moderate but significant
150 acceleration of SV endocytosis monitored by vGLUT1-pHluorin (Figure 1K,L) but no change in
151 apparent SV fusion (Figure 1- Supplement 1O). Ultrastructural analysis of hippocampal synapses
152 from mDia1/3-depleted neurons by electron microscopy revealed a reduction in SV density
153 compared to controls (Figure 2A,B). This phenotype was rescued upon prior silencing of
154 endogenous neuronal network activity in the presence of tetrodotoxin (TTX) (Figure 2C and Figure
155 2-Supplement 1A,B). A similar, slightly more pronounced depletion of SVs was observed in
156 hippocampal synapses from mDia1 knockout (KO) mice (Peng *et al*, 2007; Peng *et al*, 2003;
157 Shinohara *et al.*, 2012) (Figure 2D,E).

158 These data are consistent with a role for actin dynamics (see Fig. 1) and actin nucleating
159 mDia1/3 proteins in presynaptic endocytosis and SV recycling.

160

161 *mDia facilitates SV endocytosis by regulating presynaptic F-actin*

162 mDia1 in addition to its Rho binding domain and a C-terminal actin-assembling formin
163 homology 2 (FH2) domain comprises an unstructured N-terminal region involved in membrane
164 binding (Eisenmann *et al.*, 2005; Ramalingam *et al*, 2010) (Figure 3A). This architecture suggests
165 that mDia specifically promotes the nucleation of unbranched actin filaments at membranes, for
166 example to promote endocytosis at the presynaptic plasma membrane. To test this hypothesis, we
167 assayed the ability of mutant mDia1 lacking its N-terminal membrane-binding region (mDia1-ΔN)
168 (Ramalingam *et al.*, 2010) to rescue defective SV endocytosis in hippocampal neurons depleted of
169 endogenous mDia1. Mutant mDia1-ΔN displayed reduced association with membranes in
170 transfected HEK293T cells (Figure 3-Supplement 1A,B) and was unable to restore normal kinetics
171 of Syph-pHluorin endocytosis in hippocampal neurons transfected with mDia1-specific
172 microRNA (Figure 3B and Figure 3-Supplement 1C). Hence, mDia may act on SV endocytosis by

173 specifically promoting actin assembly at presynaptic membranes. We probed this model at several
174 levels. We analyzed the nanoscale localization and distribution of mDia1 via multicolor time-gated
175 stimulated emission depletion (gSTED) microscopy. Hippocampal neurons were stained for
176 mDia1, the presynaptic active zone marker Bassoon, and post-synaptic Homer1. The distributions
177 of all three proteins along line profiles perpendicular to the synaptic cleft (i.e. the space between
178 Bassoon and Homer1 clusters) were analyzed (Gerth *et al*, 2017) (Figure 3-Supplement 1H). This
179 analysis revealed that endogenous mDia1 is primarily localized to the presynaptic compartment,
180 where it is concentrated at or very close to the plasma membrane (Figure 3C,D), i.e. < 50 nm away
181 from the presynaptic membrane (see (Dani *et al*, 2010)). Prompted by these results we dissected
182 the interactome of mDia1 by unbiased quantitative proteomic analyses of immunoprecipiates from
183 detergent-extracted mouse synaptosomes (Figure 3-Supplement 1D). In addition to actin, we
184 identified a variety of additional actin-regulatory proteins including Myosin IIB (Chandrasekar *et*
185 *al*, 2013) and the small GTPase Rac1 (Figure 3E). We confirmed the association of mDia1 with
186 actin and Myosin IIB (Figure 3-Supplement 1E) and found Myosin IIB to be concentrated at or
187 near the presynaptic plasma membrane (Figure 3-Supplement 1F,G) akin to the localization of
188 mDia1. The association of mDia1 with Myosin IIB is consistent with the inhibitory effects of the
189 Myosin II inhibitor blebbistatin on SV endocytosis (Chandrasekar *et al.*, 2013; Soykan *et al.*,
190 2017). Interestingly, we also observed an enrichment of several endocytic proteins previously
191 implicated in SV recycling in mDia1 immunoprecipitates. These include the lipid phosphatase
192 Synaptojanin1, the bin-amphiphysin-rvs (BAR) domain proteins Amphiphysin, Endophilin A1,
193 and PACSIN1/2 and, the GTPase Dynamin1 (Chanaday *et al.*, 2019; Gan & Watanabe, 2018;
194 Saheki & De Camilli, 2012; Soykan *et al.*, 2016) (Figure 3E) as confirmed by immunoblotting
195 (Figure 3F). Based on the association of mDia1 with endocytic proteins including Dynamin1, we
196 hypothesized that mDia1 might get stalled at endocytic intermediates that accumulate under

197 conditions of perturbed Dynamin function (Ferguson *et al.*, 2009; Raimondi *et al.*, 2011).
198 Application of the partially non-selective Dynamin inhibitor Dynasore (Macia *et al*, 2006) (Figure
199 3C,H) or expression of dominant-negative mutant Dynamin1 K44A (Figure 3G,I) led to a
200 significant accumulation of mDia1 at presynaptic sites marked by Bassoon. mDia1 levels at the
201 postsynapse were also increased (Figure 3-Supplement 1I). Dynasore did not impact the levels
202 (Figure 3- Supplement 1J) or distribution of Bassoon or Homer1.

203 Based on these results we next investigated the relationship between mDia1/3 and
204 presynaptic actin. Multicolor gSTED imaging confirmed that F-actin labeled by phalloidin was
205 highly abundant at the postsynaptic compartment. In addition, F-actin was also visible, albeit at
206 reduced levels, in presynaptic boutons marked by Bassoon (Figure 4A,B). Inhibition of Dynamin
207 in the presence of Dynasore (Figure 4C and Figure 4-Supplement 1A) or expression of Dynamin1
208 K44A (Figure 4-Supplement 1B,C) significantly elevated presynaptic F-actin levels within the
209 Bassoon area. These data are consistent with a role for presynaptic actin in SV endocytosis. We
210 directly tested the role of mDia in presynaptic actin nucleation and actin-dependent SV endocytosis
211 in several ways. First, we generated a mutant version of mDia1 that lacks the ability to nucleate
212 F-actin due to site-specific inactivation of its FH2 domain (Daou *et al*, 2014; Higashi *et al*, 2008;
213 Xu *et al*, 2004). We found that actin polymerization-defective mutant mDia1 (K994A) failed to
214 restore delayed vGLUT1-pHluorin endocytosis in mDia1-depleted hippocampal neurons (Figure
215 4D and Figure 4-Supplement 1D). Second, we analyzed the effects of depleting hippocampal
216 neurons of mDia1/3 on presynaptic F-actin. We found that loss of mDia1/3 significantly reduced
217 the amount of detectable F-actin within the Bassoon area (Figure 4A,E). To unequivocally
218 distinguish between presynaptic actin at exo-/ endocytic sites and the abundant pool of
219 postsynaptic actin associated with the postsynaptic density, we used the ORANGE strategy for
220 CRISPR-based genome-engineering (Willems *et al*, 2020) to generate eGFP-β-actin knock-in (KI)

221 hippocampal neurons. Due to the low knockin efficiency, this strategy allowed us to visualize
222 endogenously tagged eGFP-β-actin by 2-color gSTED imaging exclusively in presynaptic boutons
223 marked by vGLUT1. This assay confirmed the significant reduction in endogenous β-actin at
224 presynapses from mDia1/3-depleted neurons (Figure 4F,G). Third, we reasoned that if loss of
225 presynaptic actin in mDia-depleted neurons was causal for the observed defect in SV endocytosis,
226 pharmacological stabilization of F-actin might rescue the endocytic phenotype. Treatment of
227 mDia1/3-depleted neurons with jasplakinolide indeed fully restored the kinetics of SV endocytosis
228 monitored by vGLUT1-pHluorin (Figure 4H and Figure 4-Supplement 1H) and rescued
229 presynaptic F-actin levels to that of controls (actin levels normalized to shCTR + DMSO set to
230 100: shCTR + DMSO = 100 ± 6.3; shmDia1+3 + DMSO = 47.7 ± 4.3; shCTR + Jasp = 150.6 ±
231 11.9; shmDia1+3 + Jasp = 94.3 ± 11.5) (Figure 4-Supplement 1G).
232 We conclude that mDia1/3 facilitates SV endocytosis by regulating presynaptic F-actin.
233
234 *mDia1/3-Rho and Rac1 signaling pathways cooperatively act to facilitate presynaptic endocytosis*
235 In non-neuronal cells mDia proteins have been shown to be disinhibited by active Rho
236 family GTPases, in particular RhoA (Otomo *et al*, 2005) (Figure 5A and Figure 1-Supplement
237 1N). We reasoned that Rho proteins might serve a similar function at presynaptic nerve terminals
238 in hippocampal neurons. Multicolor gSTED imaging revealed that endogenous RhoA was mostly
239 located within the presynaptic compartment (Figure 5B,C). Interference with Rho function by co-
240 expression of dominant-negative (DN) variants of RhoA and RhoB (Figure 5D and Figure 5-
241 Supplement 1A) or co-depletion of these Rho isoforms (Figure 5-Supplement 1C) delayed SV
242 endocytosis in response to stimulation with 200 APs without impacting the apparent levels of
243 exocytosis (Figure 5- Supplement 1B,D). These results are consistent with a model in which active
244 Rho promotes mDia function and, thereby F-actin nucleation.

245 F-actin dynamics are known to be controlled by interdependent signaling networks
246 characterized by feedback regulation between components within the same pathway and between
247 key regulatory switches (e.g. distinct Rho/Rac family members) that drive distinct forms of F-actin
248 (see below) (Lawson & Ridley, 2018). For example, active mDia is known to stimulate RhoA
249 activation (Kitzing *et al*, 2007) (Figure 5A). Consistently, we found that RhoA activity was
250 reduced in hippocampal neurons depleted of mDia1/3 (Figure 5E,F). Work in non-neuronal cells
251 has further revealed that RhoA activity antagonizes activation of Rac1 (Chauhan *et al*, 2011), a
252 key factor for promoting the formation of branched F-actin networks at the cell cortex (Hodge &
253 Ridley, 2016; Lawson & Ridley, 2018) (Figure 6A). We hypothesized that reciprocally
254 interdependent Rho/ Rac1 signaling might control presynaptic F-actin assembly and, thereby, SV
255 endocytosis. In agreement with the alleged antagonistic regulation of RhoA and Rac1 function
256 (Lawson & Ridley, 2018), we found Rac1 activity to be significantly elevated in hippocampal
257 neurons depleted of mDia1/3 (Figure 6B,C), e.g. under conditions of reduced Rho-GTP levels. A
258 similar increase in active Rac1 levels was observed upon pharmacological inhibition of RhoA/B
259 in the presence of Rhosin (Figure 6-Supplement 1A). Multicolor gSTED imaging showed that
260 Rac1 was equally distributed between pre- and postsynaptic compartments in unperturbed
261 hippocampal neurons (Figure 6D,E). Elevated active Rac1 levels might conceivably ameliorate
262 presynaptic endocytic phenotypes elicted by mDia1/3 loss. In support of this hypothesis, we found
263 that selective pharmacological inhibition of Rac1 reduced presynaptic actin levels (Figure 6-
264 Supplement 1B,C) and caused a delay in the endocytic retrieval of endogenous vGAT (Figure
265 6F,G). Moreover, Rac1 inhibition appeared to further aggravate impaired vGAT endocytosis in
266 mDia1/3-depleted neurons, although the effect remained below statistical significance. Expression
267 of constitutively active GTP-locked Rac1 (Rac1-CA) restored normal Syph-pHluorin endocytosis
268 kinetics in mDia1/3-depleted neurons, whereas Syph-pHluorin endocytosis was delayed upon

269 expression of dominant-negative Rac1 (Rac1-DN) and exacerbated the endocytic phenotype of
270 mDia1/3 loss (Figure 6H and Figure 6-Supplement 1E). No overt effect of Rac1 inhibition or
271 overexpression of either Rac1 form on SV exocytosis was observed (Figure 6-Supplement 1D,F).
272 Perturbation of the related Cdc42 protein, another actin regulatory GTPase (Lawson & Ridley,
273 2018) found at synapses (Figure 6-Supplement 1G-I), did not significantly affect the kinetics of
274 SV endocytosis in control or mDia1/3-depleted neurons (Figure 6- Supplement 1J,K). These data
275 suggest that interdependent mDia1/3 and Rac1-based pathways control SV endocytosis via
276 presynaptic actin.

277 We probed this model by analyzing the ultrastructure of synapses from hippocampal
278 neurons depleted of mDia1/3 or following inhibition of Rac1 activity. Synapses from mDia1/3-
279 depleted neurons displayed an accumulation of non-coated plasma membrane invaginations that
280 were found both in the vicinty of the active zone as well as distal from the synaptic contact area
281 (Figure 7A,B). Moreover, we observed elevated numbers of endosome-like vacuoles (ELVs)
282 (Figure 7A,C) that might serve as a donor membrane for SV reformation (Kononenko & Haucke,
283 2015; Kononenko *et al.*, 2014; Watanabe *et al.*, 2014) as suggested by the observed reduction in
284 SV numbers in mDia-depleted neurons (compare Figure 2). A prominent accumulation of plasma
285 membrane invaginations (Figure 7-Supplement 1A) and endosome-like vacuoles (Figure 7-
286 Supplement 1B) was similarly found in hippocampal neurons from mDia1 KO mice. Inhibition of
287 Rac1 function by EHT 1864 also led to the accumulation of non-coated plasma membrane
288 invaginations (Figure 7A,D), whereas the number of endosome-like vacuoles was not significantly
289 altered (Figure 7A, E). Pharmacological blockade of Rac1 activity in neurons depleted of mDia1/3
290 further increased the number of plasma membrane invaginations significantly, while the additional
291 effect on the number of endosome-like vacuoles remained insignificant (Figure 7F,G,H). mDia1/3

292 loss and Rac1 perturbation exhibited similar phenotypes with respect to the length and width of
293 tubular membrane invaginations (Figure 7-Supplement 1C,D).
294 Collectively, these findings demonstrate that mDia1/3-Rho and Rac1 signaling pathways
295 cooperatively act to facilitate presynaptic endocytosis and SV recycling.
296
297 **DISCUSSION**
298 We found that loss of mDia1 either alone or in conjunction with the closely related mDia3 isoform
299 slows the kinetics of SV endocytosis of exogenous pHluorin-tagged SV proteins and of
300 endogenous vGAT without perturbing exocytic SV fusion. These phenotypes are accompanied by
301 the accumulation of plasma membrane invaginations and vacuolar structures as well as an activity-
302 dependent reduction of the total SV pool (Figures 1, 2, and 7). Furthrmore, we observe that
303 interdependent mDia1/3-Rho and Rac1 signaling pathways cooperatively act to facilitate
304 presynaptic endocytosis (Figures 5, 6 and 7). Several lines of evidence indicate that these endocytic
305 phenotypes are a consequence of perturbed presynaptic actin levels or dynamics. (i) Endogenous
306 presynaptic F-actin is reduced in mDia1/3-depleted hippocampal synapses (Figure 4) and (ii) actin
307 polymerization-defective mDia1 fails to restore normal endocytosis kinetics in hippocampal
308 neurons depleted of mDia1 (Figure 4). Conversely, (iii) pharmacological stabilization of F-actin
309 by jasplakinolide (Figure 4) or (iv) expression of constitutively-active Rac1 to drive compensatory
310 actin polymerization (for example via other formins and/ or ARP2/3) (Figure 6) rescues
311 endocytosis in mDia1/3-KD hippocampal neurons. Moreover, (v) we find mDia1 (Figure 3) and
312 F-actin (Figure 4) to accumulate at presynapses under conditions of impaired dynamin-dependent
313 endocytosis. Together with the observation that inhibition of F-actin dynamics (Peng *et al.*, 2011)
314 in the combined presence of latrunculin A, jasplakinolide, and Y-27632 (Figure 1) slows the

315 kinetics of SV endocytosis, our data support the hypothesis that presynaptic actin facilitates SV
316 endocytosis downstream of mDia/ RhoA and Rac1-based signaling pathways.

317 Our data extend previous studies using conditional genetics that have identified an actin
318 requirement for SV endocytosis (Wu *et al.*, 2016). The endocytic phenotype described here for
319 loss of mDia1/3, however, is substantially milder than that elicited by complete loss of β– or γ-
320 actin, likely reflecting the fact that several partially redundant pathways cooperate to promote
321 F-actin assembly at synapses (see below). In contrast to β- or γ-actin KO hippocampal neurons
322 (Wu *et al.*, 2016) we did not observe strong exocytic depression in response to train stimulation in
323 mDia-depleted neurons (e.g. Figure 1-Supplement 1A-M) although we cannot rule out mild
324 differences in synaptic strength and/ or release probability as observed in Rac1 KO hippocampal
325 neurons and at the calyx of Held (Keine *et al.*, 2022; O'Neil *et al.*, 2021).

326 At the ultrastructural level, we find that genetic (KO) or lentiviral induced (KD) loss of
327 mDia1 or mDia1/3 partially phenocopies acute perturbation of formin-mediated actin assembly
328 (Soykan *et al.*, 2017) with respect to the accumulation of plasma membrane invaginations. Unlike
329 acute formin inhibition (Soykan *et al.*, 2017), we find elevated numbers of post-fission endosome-
330 like vacuoles in mDia-depleted hippocampal synapses. The latter correlate with a mild reduction
331 of SV numbers, suggesting that mDia may have a further role in SV reformation downstream of
332 the actual endocytosis reaction (Chanaday *et al.*, 2019; Gan & Watanabe, 2018; Kononenko *et al.*,
333 2014). The identified function of mDia1/3-mediated presynaptic actin assembly in presynaptic
334 endocytosis and SV recycling is consistent with the actin binding properties of many endocytic
335 proteins including Dynamin (Ferguson *et al.*, 2009; Gu *et al*, 2014), PACSINs (Kessels &
336 Qualmann, 2006), or Epsins, among others (McMahon & Boucrot, 2011; Merrifield *et al.*, 2005;
337 Saheki & De Camilli, 2012). How exactly actin functions to facilitate endocytosis of SV
338 membranes remains to be fully understood. The comparably small size of the membrane

339 invaginations that accumulate following pharmacological inhibition of formins (< 100 nm) or Rac1
340 or upon genetic loss of mDia1 (typically < 150 nm, although larger ones are observed) render an
341 actomyosin-based constriction mechanism for SV endocytosis unlikely (consistent with
342 (Sankaranarayanan *et al.*, 2003)). We rather favor a - possibly indirect - function of F-actin in
343 presynaptic endocytosis via formation of an F-actin ring that couples exocytic membrane
344 compression to endocytic pit formation (Ogunmowo *et al.*, 2023). Such a model is supported by
345 the abundance of large plasma membrane invaginations distal from the active zone where SV
346 fusion occurs at synapses following mDia1/3 and Rac1 loss of function (Figure 7). Consistent with
347 this, it has been shown that mDia1 controls presynaptic membrane contractility (Deguchi *et al*,
348 2016), e.g. via the recently identified presynaptic actin corrals visualized in genome-engineered
349 rat hippocampal neurons (Bingham *et al*, 2023).

350 A key result from our study is the finding that presynaptic endocytosis is regulated by
351 interdependent, yet partially redundant signaling for F-actin assembly downstream of Rho and
352 Rac1, e.g. pathways known to control linear and branched F-actin networks (Lawson & Ridley,
353 2018; Muller *et al.*, 2020) that were shown to co-exist within hippocampal presynaptic boutons
354 (Bingham *et al.*, 2023). We demonstrate that loss of mDia1/3 or inhibition of Rho cause the
355 hyperactivation of the actin-promoting GTPase Rac1 and that dual loss of mDia1/3 loss and Rac1
356 function results in synergistic inhibitory effects with respect to presynaptic endocytosis and
357 ultrastructural defects (Figures 5-7). These findings suggest that the signaling network that
358 regulates presynaptic actin assembly may have been evolutionary selected for plasticity and
359 resilience. A resilient network for the control of actin dynamics at the presynapse may also help
360 to explain the partially contradicting results from drug-based manipulations of actin and actin
361 regulatory factors in different models of presynaptic neurotransmission reported in the past
362 (Bleckert *et al.*, 2012; Del Signore *et al.*, 2021; Hori *et al.*, 2022; Piriya Ananda Babu *et al.*, 2020;

363 Richards *et al*, 2004; Sankaranarayanan *et al.*, 2003; Shupliakov *et al.*, 2002; Wu & Chan, 2022;
364 Wu *et al.*, 2016). Moreover, accumulating evidence indicates that different pools of actin might be
365 differentially amenable to drug treatments (Bleckert *et al.*, 2012), e.g. as a consequence of the
366 association of actin filaments with molecules such as tropomyosin (Gormal *et al*, 2017) that render
367 them resistant to drugs, and/ or variations in the fraction of F-actin *vs*. monomeric actin pools
368 (Higashida *et al*, 2008), providing a possible explanation for previously discrepant results.

369 A number of open questions remain. We predict that presynaptic actin assembly via mDia/
370 Rho and Rac1 facilitates all forms of presynaptic endocytosis that operate on timescales of
371 milliseconds to seconds (Chanaday & Kavalali, 2018; Clayton & Cousin, 2009; Watanabe &
372 Boucrot, 2017) and at many types of synapses (e.g. small central synapses, ribbon synapses, the
373 neuromuscular junction), but further studies will be needed to test this hypothesis. We note that
374 fast endophilin-mediated endocytosis (FEME), a process with resemblance to endocytosis at
375 synapses (Watanabe & Boucrot, 2017), has been shown to be differentially regulated by actin and
376 Rho GTPase family members (Boucrot *et al*, 2015; Renard *et al*, 2015). At present we do not
377 understand if and how RhoA/B and Rac1 GTPase activation is nested into the SV cycle and
378 whether these GTPases operate at the same or different nanoscale sites and on the same or different
379 membranes. Future studies will be required to tackle these questions.
380
381

382 **MATERIALS AND METHODS**

Key Resources Table

Reagent type (species) or resource	Designation	Source or reference	Identifiers	Additional information
genetic reagent (Mus musculus)	C57BL/6N wild type	Leibniz Research Institute for Molecular Pharmacology	RRID:IMSR_JAX:000664	
genetic reagent (Mus musculus)	mDia1 KO	Bartolini Lab, Columbia University		
cell line (Homo sapiens)	HEK293T	American Type Culture Collection	Cat# CRL-3216; RRID:CVCL_0063	
antibody	β-Actin (mouse monoclonal)	Sigma-Aldrich	Cat# A5441; RRID:AB_476744	IB (1:5000)
antibody	Bassoon (guinea pig monoclonal)	Synaptic Systems	Cat# 141 318; RRID:AB_2927388	IC (1:100)
antibody	CDC42 (rabbit polyclonal)	Abcam	Cat# ab64533; RRID:AB_1310067	IB (1:1000); IC (1:100)
antibody	Dynamin1 (rabbit polyclonal)	Pietro D. Camilli	Shupliakov et al., 1997; DOI: 10.1126/science.276.5310.259	IB (1:2000)
antibody	GFP (mouse monoclonal)	Thermo Fisher Scientific	Cat# A-11120; RRID:AB_221568	IC (1:2500)
antibody	Homer1 (mouse monoclonal)	Synaptic Systems	Cat# 160 011; RRID:AB_2120992	IC (1:200)

antibody	Homer1 (rabbit polyclonal)	Synaptic Systems	Cat# 160 003; RRID:AB_887730	IC (1:200)
antibody	LAMP1 (rabbit monoclonal)	Cell Signaling Technology	Cat# 9091; RRID:AB_2687579	IB (1:1000)
antibody	mDia1 (mouse monoclonal)	BD Biosciences	Cat# 610848; RRID:AB_398167	IB (1:500); IP (2µg)
antibody	mDia1 (rabbit monoclonal)	Abcam	Cat# ab129167; RRID:AB_11143749	IC (1:100)
antibody	mDia3 (rabbit polyclonal)	Sigma-Aldrich	Cat# HPA005647; RRID:AB_1078657	IB (1:1000)
antibody	Myosin IIb (mouse monoclonal)	Abcam	Cat# ab684; RRID:AB_305661	IC (1:100)
antibody	Myosin IIb (rabbit polyclonal)	Cell Signaling Technology	Cat# 3404; RRID:AB_126421	IB (1:2000)
antibody	Rac1 (mouse monoclonal)	BD Biosciences	Cat# 610650; RRID:AB_397977	IB (1:1000); IC (1:50)
antibody	RFP (rabbit polyclonal)	Takara Bio	Cat# 632496; RRID:AB_10013483	IC (1:500)
antibody	RhoA (rabbit monoclonal)	Cell Signaling Technology	Cat# 2117; RRID:AB_10693922	IB (1:1000); IC (1:100)
antibody	α-Tubulin (mouse monoclonal)	Sigma-Aldrich	Cat# T9026; RRID:AB_47759	IB (1:5000)

antibody	IgG control (mouse monoclonal)	Thermo Fisher Scientific	Cat# 31903; RRID:AB_10959891	IP (2 µg)
antibody	vGAT-CypHer5E (rabbit polyclonal)	Synaptic Systems	Cat# 131 103CpH; RRID:AB_2189809	Live-imaging (1:500)
antibody	Anti-mouse IgG Atto542 (donkey polyclonal)	Martin Lehmann	Gonschior et al., 2022; https://doi.org/10.1038/s41467-022-32533-4	IC (1:400)
antibody	Anti-rabbit IgG Atto542 (donkey polyclonal)	Martin Lehmann	Gonschior et al., 2022; https://doi.org/10.1038/s41467-022-32533-4	IC (1:400)
antibody	Anti-mouse Alexa Fluor™ 594 (goat polyclonal)	Thermo Fisher Scientific	Cat# A-11032; RRID:AB_2534091	IC (1:200)
antibody	Anti-rabbit Alexa Fluor™ 594 (goat polyclonal)	Thermo Fisher Scientific	Cat# A-11037; RRID:AB_2534095	IC (1:200)
antibody	Anti-guinea pig Atto647N (camelid monoclonal)	Synaptic Systems	Cat# N0602-At647N-S; RRID:AB_2744576	IC (1:200)
antibody	Anti-mouse Alexa Fluor™ 647 (goat polyclonal)	Thermo Fisher Scientific	Cat# A-21235; RRID:AB_2535804	IC (1:200)

antibody	Anti-mouse IRDye® 680RD (goat polyclonal)	LI-COR Biosciences	Cat# 925-68070; RRID:AB_2651128	IB (1:10000)
antibody	Anti-rabbit IRDye® 680RD (goat polyclonal)	LI-COR Biosciences	Cat# 926-68071; RRID:AB_10956166	IB (1:10000)
antibody	Anti-mouse IgG, IRDye® 800CW (goat polyclonal)	LI-COR Biosciences	Cat# 926-32210; RRID:AB_621842	IB (1:10000)
antibody	Anti-rabbit IgG, IRDye® 800CW (goat polyclonal)	LI-COR Biosciences	Cat# 926-32211; RRID:AB_621843)	IB (1:10000)
chemical compound, drug	Phalloidin-Alexa FluorTM 594	AAT Bioquest	Cat# ABD-23158	IC (1:1000)
recombinant DNA reagent	Synaptophysin-pHluorin	Leon Lagnado	Granseth et al., 2006; DOI: 10.1016/j.neuron.2006.08.029	Expresses rat Synaptophysin-2xpHluorin (inserted between Asn183 – Thr184) under a CMV promotor
recombinant DNA reagent	vGlut1-pHluorin	Volker Haucke	Bolz et al., 2023; https://doi.org/10.1016/j.neuron.2023.08.016	Expresses rat vGlut1-pHluorin (inserted between Gly99 – Gly100) under a hSyn1 promotor; lentiviral plasmid
recombinant DNA reagent	mCherry	Clontech	Cat# 632523	Expresses mCherry under a CMV promotor
recombinant DNA reagent	mDia1-WT-mCherry	This study	-	Expresses mouse mDia1-WT-mCherry under a CMV promotor
recombinant DNA reagent	mDia1-ΔN -mCherry	This study	-	Expresses truncation (first 60 AA) variant of mouse mDia1-mCherry under a CMV promotor

recombinant DNA reagent	mDia1-WT-SNAP	This study	-	Expresses mouse mDia1-WT-SNAP under a hSyn1 promotor; lentiviral plasmid
recombinant DNA reagent	mDia1-K994A-SNAP	This study	-	Expresses K994A variant of mDia1-SNAP under a hSyn1 promotor; lentiviral plasmid
recombinant DNA reagent	Dynamin1-WT-SNAP	This study	-	Expresses mouse Dynamin1-WT-SNAP under a hSyn1 promotor; lentiviral plasmid
recombinant DNA reagent	Dynamin1-K44A-SNAP	This study	-	Expresses K44A variant of mouse Dynamin1-SNAP under a hSyn1 promotor; lentiviral plasmid
recombinant DNA reagent	vGlut1-mCherry	Franck Polleux	Kwon et al., 2016; https://doi.org/10.1371/journal.pbio.1002516	Expresses rat vGlut1-mCherry under a CAG promotor
recombinant DNA reagent	RhoA-WT	Theofilos Papadopoulos	Reddy-Alla et al. 2010; https://doi.org/10.1111/j.1460-9568.2010.07149.x	Expresses human 3xHA-RhoA-WT under a CMV promotor
recombinant DNA reagent	RhoA-DN	Theofilos Papadopoulos	Reddy-Alla et al. 2010; https://doi.org/10.1111/j.1460-9568.2010.07149.x	Expresses T19N variant of human 3xHA-RhoA under a CMV promotor
recombinant DNA reagent	RhoB-WT	Harry Mellor	Mellor et al., 1998; https://doi.org/10.1074/jbc.273.9.4811	Expresses human myc-RhoB-WT under a CMV promotor

recombinant DNA reagent	RhoB-DN	Harry Mellor	Mellor et al., 1998; https://doi.org/10.1074/jbc.273.9.4811	Expresses T19N variant of human myc-RhoB under a CMV promotor
recombinant DNA reagent	shCTR (transfected)	Sigma-Aldrich	Cat# SHC016	No murine targets
recombinant DNA reagent	shmDia1 (transfected)	Sigma-Aldrich	Cat# TRCN0000108685	Targets 3'UTR of NM_007858
recombinant DNA reagent	shRhoA (transfected)	Sigma-Aldrich	Cat# TRCN0000302388	Targets CDS of NM_016802
recombinant DNA reagent	shRhoB (transfected)	Sigma-Aldrich	Cat# TRCN0000294874	Targets CDS of NM_007483
recombinant DNA reagent	shCTRmiR	This study	-	Expresses rat Synaptophysin-2xpHluorin under a CMV promotor and shRNA embedded into a microRNA (shRNAmiR) with no murine targets
recombinant DNA reagent	shmDia1miR	This study	-	Expresses rat Synaptophysin-2xpHluorin under a CMV promotor and shRNAmiR against the CDS of mouse mDia1
recombinant DNA reagent	shCTR (transduced)	Christian Rosenmund	Watanabe et al., 2014; https://doi.org/10.1038/nature13846	Expresses NLS-RFP or BFP under a hSyn1 promotor and shRNA against no murine target (msClathrin scrambled) under a U6 promotor
recombinant DNA reagent	shmDia1 (transduced)	This study	-	Expresses NLS-RFP or BFP under a hSyn1 promotor and shRNA against the 3'UTR of

				mouse mDia1 under a U6 promotor
recombinant DNA reagent	shmDia3 (transduced)	This study	-	Expresses NLS-RFP or BFP under a hSyn1 promotor and shRNA against the CDS of mouse mDia3 under a U6 promotor
recombinant DNA reagent	MD2.G	Addgene	Cat# 12259; RRID:Addgene_12259	Expresses lentiviral VSV-G envelope protein
recombinant DNA reagent	psPAX2	Addgene	Cat# 12260; RRID:Addgene_12260	Expresses lentiviral packaging protein
recombinant DNA reagent	pOrange GFP-β-Actin KI	Addgene	Cat#131479; RRID:Addgene_131479	gRNA and GFP donor for endogenous N-terminal tagging of β-Actin (amino acid position: D2)
chemical compound, drug	Dynasore	Sigma-Aldrich	Cat# D7693	80 µM 10 min
chemical compound, drug	EHT 1864	MedChemExpress	Cat# HY-16659	10 µM acute (CypHer); 2 h (IC/EM)
chemical compound, drug	IMM-01	Sigma-Aldrich	Cat# SML1064	10 µM acute
chemical compound, drug	Jasplakinolide	Sigma-Aldrich	Cat# J4580	8 µM acute (JLY); 1 µM 30 min
chemical compound, drug	Latrunculin A	Cayman Chemical	Cat# CAY10684	5 µM acute (JLY)
chemical compound, drug	ML141	MedChemExpress	Cat# HY-12755	10 µM acute
chemical compound, drug	Rhosin	MedChemExpress	Cat# HY-12646	10 µM 2 h
chemical compound, drug	Tetrodotoxin	Carl Roth	Cat# 6973.1	1 µM 36 h
chemical compound, drug	Y-27632	Tocris	Cat# 1254	1 µM acute (JLY)

commercial assay or kit	Rhotekin-Rho binding domain (RBD) beads	Cytoskeleton Inc.	Cat# RT02	60 µg
commercial assay or kit	PAK-p21 binding domain (PBD) beads	Cytoskeleton Inc.	Cat# PAK02	20 µg
commercial assay or kit	ProFection Mammalian Transfection System – Calcium Phosphate	Promega	Cat# E1200	
commercial assay or kit	Gibson Master Mix	New England Biolabs Inc.	Cat# E2611L	
commercial assay or kit	Q5 site-directed mutagenesis kit	New England Biolabs Inc.	Cat# E0552S	
software, algorithm	Fiji	NIH	RRID:SCR_002285	
software, algorithm	Prism	GraphPad	RRID:SCR_002798	Version 9.5.1.
software, algorithm	Image Lab Software	Bio-Rad	RRID:SCR_014210	Version 6.0.1
software, algorithm	Image Studio Lite	LI-COR Biosciences	RRID:SCR_013715	Version 5.2.5
software, algorithm	pHluorin ROI sector	Github	https://github.com/DennisVoll/pHluorin_ROI_selector/; RRID:SCR_002630	
software, algorithm	SynActJ	Martin Lehmann	Schmied et al., 2021;	

			https://doi.org/10.3389/fcomp.2021.777837	
software, algorithm	Macro_plot_lineprofile_multicolor	Kees Straatman	F. Gerth et al., 2019; https://doi.org/10.1016/j.str.2019.03.020	
software, algorithm	MaxQuant	Jürgen Cox	https://www.maxquant.org/maxquant/	Version 1.6.1.0

383

384 **Materials**

385 **Animals**

386 Primary neurons were obtained from either wild-type C57BL/6J (Charles River, RRID:
387 IMSR_JAX:000664) or mDia1 KO mice (Peng *et al.*, 2007; Peng *et al.*, 2003). All animal
388 experiments were reviewed and approved by the ethics committee of the *Landesamt für*
389 *Gesundheit und Soziales* (LAGeSo) Berlin or the Committee on the Ethics of Animal Experiments
390 of Columbia University and conducted according to the committees' guidelines (LAGeSo) or the
391 Guide for the Care and Use of Laboratory Animals of the National Institutes of Health (for mDia1
392 KO mice). At the facilities, animal care officers monitored compliance with all regulations. Mice
393 were group-housed under 12/12 h light/dark cycle with access to food and water *ad libitum*. Mice
394 from both genders were used and cultures were randomly allocated to experimental groups (e.g.,
395 different treatments). Multiple independent experiments using several biological replicates were
396 carried out as indicated in the Figure legends.

397

398 **Antibodies**

399 Antibodies and their working dilutions used in this study are denoted in the Key Resource Table
400 (IB: Immunoblot; IC: Immunocytochemistry; IP: Immunoprecipitation). Antibodies were stored
401 according to the manufacturer's recommendations. All secondary antibodies are species-specific
402 (highly cross-adsorbed).
403
404 **Cell lines**
405 Human embryonic kidney 293T (HEK293T) cells were obtained from the American Type Culture
406 Collection (Cat# CRL-3216; RRID:CVCL_0063). Cells were cultured in Dulbecco's modified
407 Eagle's medium supplemented with glucose (DMEM; 4.5 g/L; Thermo Fisher Scientific) and 10%
408 heat-inactivated fetal bovine serum (FBS; Gibco), penicillin (100 U/ml; Gibco), and streptomycin
409 (100 µg/ml; Gibco) at 37°C and 5% CO_2. Cells were routinely tested for mycoplasma
410 contamination.
411
412 **Chemicals**
413 Compounds were dissolved in dimethyl sulfoxide (DMSO), unless indicated otherwise, and
414 diluted 1: 1000 to their working concentrations (s. Key Resource Table). For acute
415 pharmacological treatment (in pHluorin/CypHer assays), drugs were added to the imaging buffer.
416 For longer incubations, the conditioned cell media was supplemented with the chemicals (s. Key
417 Resource Table for incubation time).
418 For silencing neuronal network activity, sodium channels were inhibited by addition of
419 tetrodotoxin (TTX; in 10 mM sodium acetate, pH 5.3) to the neuronal culture medium at day in
420 vitro (DIV) 12 for 36 h. As a control, cells from the same preparation were treated with equal
421 volumes of 10 mM sodium acetate (annotated as Vehicle).
422

423 **Plasmids**

424 All recombinant DNA reagents used for protein expression are listed in the Key Resource Table:
425 Synaptophysin-pHluorin was a kind gift from Dr. L. Lagnado (Univ. of Sussex, UK), vGLUT1-
426 pHluorin was generated in-house by Svenja Bolz as previously described, while vGLUT1-
427 mCherry was kindly provided by Dr. Franck Polleux (New York, USA). HA-tagged RhoA-WT
428 and RhoA-T19N were kind gifts from Dr. Theofilos Papadopoulos (Göttingen, Germany) and
429 myc-tagged RhoB-WT and RhoB-T19N were kindly gifted by Dr. Harry Mellor (Bristol, UK). All
430 other expression vectors were generated for this study. Plasmids based on pEGFP-C1, pmCherry-
431 N1, pCAG and pcDNA3 utilising a CMV or CAG promotor (s. Key Resource table) were used for
432 overexpression based on transfection of neuronal cells, while pFUGW vectors carrying a human
433 Synapsin1 promotor (hSyn1) were used for the generation of lentiviral particles for the
434 transduction of neurons (s. Key Resource Table annotated as "lentiviral plasmid"). In the course
435 of this study several approaches to deplete mDia1 have been carried out and are annotated in the
436 Figure legends: For knockdown of mDia1, RhoA and RhoB by transfection, commercially
437 available lentiviral small hairpin RNA (shRNA) vectors based on the pLKO.1 backbone (s. Key
438 Resource Table; annotated as "transfected") were purchased from Sigma-Aldrich. To reduce the
439 amount of DNA needed for transfection to perform pHluorin assays, vectors expressing shRNA
440 embedded into a microRNA (miRNA) context for mDia1 together with Synaptophysin-2x-
441 pHluorin as a reporter were cloned based on pRRLsinPPT-emGFP-miR Control, a kind gift of Dr.
442 Peter S. McPherson (Montreal, Canada). Finally, lentiviral vectors for knockdown of mDia1 and
443 mDia3 (annotated in Key Resource Table as "transduced") were generated based on the backbone
444 f(U6) sNLS-RFPw shCTR, a kind gift from Prof. Christian Rosenmund (Berlin, Germany). All
445 vectors used for genetic depletion via RNA interference are listed in the Key Resource Table and

446 express gene-specific shRNA under a U6 promotor, that either targets the coding sequence (CDS)
447 or the 3'-untranslated region (3'-UTR).
448
449 **Oligonucleotides**
450 Plasmids generated for this study were cloned using oligonucleotides (BioTez GmbH, Berlin,
451 Germany) listed in Supporting Table 1 (lower case denotes nucleotides that do not anneal to the
452 backbone; underlined nucleotides denote sense and antisense sequences of shRNA).
453
454 **Methods**
455 **Generation of expression plasmids**
456 Expression plasmids generated for this study were cloned by PCR amplification (Phusion^{TM} High-
457 Fidelity DNA polymerase) and restriction enzyme (Thermo Fisher Scientific; Fast digest) digest
458 according to the manufacturers' manual. pSNAP-N1 was generated in-house by Hannes Gonschior
459 by sub-cloning pSNAP$_f$ (New England BioLabs Inc., Cat#N9183S) via PCR and the restriction
460 enzymes *AgeI* and *NotI* into pmCherry-N1. pFUG_hSyn_MCS was cloned by Amirreza Ohadi to
461 enable simple insertion of SNAP-tagged proteins by inserting a multiple cloning site (MCS) on
462 annealed oligonucleotides into a pFUG_hSyn1 backbone (a gift from Christian Rosenmund,
463 Berlin, Germany) cut by *AgeI* and *EcoRI*. To generate mDia1-WT-mCherry, the coding sequence
464 of mDia1 was cut from mDia1-mEmerald-N1 (Addgene, Cat#54157) and pasted into pmCherry-
465 N1 by *AgeI* and *XhoI* digestion. mDia1-WT-SNAP was cloned by cutting out the coding sequence
466 of mDia1 from mDia1-mEmerald-N1 and pasting it into pSNAP-N1 by *AgeI* and *NheI* digest of
467 both vector and insert. To subclone mDia1-SNAP into a lentiviral vector the coding sequence of
468 mDia1-SNAP was pasted from mDia1-WT-SNAP-N1 into pFUG_hSyn1_MCS utilizing common
469 cut sites for *NheI* and *NotI* digest. For the generation of a lentiviral vector expressing Dynamin-

470 WT, the coding sequence of Dynamin1 was first extracted from Dynamin1-pmCherry-N1
471 (Addgene; Cat#27697) by *EcoRI* and *XmaI* digestion and cloned into pSNAP-N1 with the same
472 enzymes. Subsequently, Dynamin1-SNAP was isolated by *NheI* and *NotI* digest and transformed
473 into pFUG_hSyn1_MCS. The mDia1- ΔN truncation variant was generated by introducing a new
474 start codon on a primer shifted by 60 amino acids (s. Supporting Table 1), PCR amplifying the
475 truncated DNA and subcloning the template into pmCherry-N1 by *BglII* and *AgeI* digest. For
476 introducing point mutations in mDia1 (Lysine-994 to Alanine; K994A) and Dynamin1 (Lysine-44
477 to Alanine; K44A), the Q5 site-directed mutagenesis kit (New England Biolabs Inc.; E0552S) was
478 used according to the manufacturer's manual and oligonucleotides listed in Supporting Table 1.
479 All vectors were confirmed by Sanger sequencing (LGC Genomics, Berlin, Germany)
480 and amplified by self-made chemically competent TOP10 *E.coli* before purifying respective
481 endotoxin-free DNA by 2-propanole precipitation.
482
483 **Isolation, culture and transfection of primary hippocampal neurons**
484 Neuronal hippocampal cell cultures were prepared as described before (Lopez-Hernandez *et al.*,
485 2022; Soykan *et al.*, 2017). In short, hippocampi from postnatal mice (p0-p3) were surgically
486 isolated and dissociated into single cells by trypsin (5 g/L, Sigma-Aldrich) digestion. Neurons
487 (100000 cells/ well of a 6-well) were plated onto poly-L-lysine-coated coverslips and grown in
488 modified Eagle medium (MEM; Thermo Fisher) supplemented with 5% FCS and 2% B-27 (Gibco)
489 and maintained at 5% CO_2 and 37°C in humidified incubators. In addition, 2 µM cytosine β-D-
490 arabinofuranoside (AraC) was added to the cell culture media in the first 2 days in vitro (DIV) to
491 limit glial proliferation. For transient protein expression, neurons were transfected on DIV 7-9
492 utilizing a Calcium phosphate transfection kit (Promega; Cat# E1200): In brief, 1-6 µg plasmid
493 DNA (per well of a 6-well plate) were mixed with 250 mM calcium phosphate ($CaCl_2$) in ultrapure

494 nuclease-free water. The resulting solution was added to equal volumes of 2x 4-(2-hydroxyethyl)-
495 1-piperazineethanesulfonic acid buffered saline (2x HEPES; 100 µL) and incubated at room
496 temperature for 20 min. Resulting precipitates were added dropwise to cells that had been
497 transferred to osmolarity-adjusted Neurobasal-A (NBA; Gibco) media to induce starvation. After
498 incubation at 37°C and 5% CO_2 for 30 min, neurons were washed thrice with osmolarity-adjusted
499 Hank's balanced salt solutions (HBSS; Gibco) and transferred back to their original conditioned
500 media.
501
502 **shRNA cloning and lentivirus production**
503 Knockdown of proteins was achieved through RNA interference either by $CaCl_2$ transfection of
504 gene-specific shRNA encoding vectors (pLKO.1; Sigma-Aldrich or shRNAmiR) on DIV 7 or by
505 transduction of cells with lentiviral particles harboring the gene-specific shRNA on DIV 2. The
506 respective method is indicated in the Figure legends as *transfected* or *transduced*. To reduce the
507 amount of DNA needed for transfection and to improve neuronal health, shRNAmiR were
508 expressed from the 3'UTR of Synaptophysin-pHluorin based on (Ritter *et al*, 2017): The reporter
509 protein/synthetic cassette was generated by PCR amplifying Synaptophysin-2x-pHluorin with
510 oligos (s. Supporting Table 1) harboring *XbaI* and *SalI* sites. The eGFP in the RRLsinPPT-eGFP-
511 miRCTR plasmid (a kind gift from Dr. Peter S. McPherson, McGill University, Canada) was
512 replaced by the PCR product through similar restriction digest to yield shCTRmiR. miRmDia1
513 (start position 4892, targeting sequence matches open-reading frame) was designed with BLOCK-
514 iT™ (Thermo Fisher Scientific) and subcloned into shCTRmiR to yield shmDia1miR following
515 protocol in (Ritter *et al.*, 2017).
516 As both transfection strategies were limited by low efficiency, lentiviral knockdown was
517 carried out: Lentiviral particles were based on a shuttle vector (pFUGw) driving the expression of

518 a nuclear-targeted red fluorescent protein (NLS-RFP) under a human Synapsin1 (hSyn1) promotor
519 to monitor infection efficiency in neurons and a scrambled mouse shRNA against Clathrin without
520 any murine targets, which was used as the control virus (f(U6) sNLS-RFPw shCTR). To prevent
521 crosstalk between the NLS-RFP and other mCherry constructs, a similar backbone expressing the
522 blue fluorescent protein (BFP) as a reporter was generated in house by Klaas Ypermann: The
523 backbone was digested by *XbaI* and *PacI*, the hSyn1 promotor and mTagBFP (Addgene; #Cat
524 105772) were amplified with oligos (s. Supporting Table 1), gel extracted and assembled utilizing
525 a Gibson master mix (New England BioLabs Inc.; Cat#E2611L) to yield f(U6) BFP shCTR. To
526 knockdown mDia1, a shRNA sequence based on 5'-GCCTAAATGGTCAAGGAGATA-3' as the
527 sense nucleotide corresponding to the 3'UTR of mouse mDia1 (NM_007858.4; Sigma-Aldrich,
528 Cat# TRCN0000108685) was designed as an oligonucleotide with overhangs (s. Supporting Table
529 1) and annealed into the f(U6) sNLS-RFPw shCTR backbone cut with *BamHI* and *PacI* to yield
530 the vector f(U6) sNLS-RFPw/BFP shmDia1. For mDia3 shRNA, a sense sequence based on
531 5'-GCCCTAATCCAGAATCTTGTA-3' corresponding to nucleotides 2473-2493 of mouse
532 mDia3 (DIAPH2; NM_172493.2; Sigma-Aldrich, Cat# TRCN0000108782) was used to construct
533 f(U6) sNLS-RFPw/BFP shmDia3 as described above. Production of lentiviral particles was
534 conducted using the second-generation packaging system: In brief, HEK293T were co-transfected
535 with lentiviral shRNA constructs and the packaging plasmids psPAX2 (Addgene; Cat# 12260) and
536 MD2.G (Addgene; Cat# 12259) using $CaCl_2$. After 12 h, the cell media was replaced. Virus-
537 containing supernatants were collected at 48 and 72 h after transfection, filtered to remove cell
538 debris and particles were concentrated (30-fold) via low-speed centrifugation (Amicon Ultra-15,
539 Ultracel-100; Merck Millipore; Cat# UFC9100) before aliquoting and storage at -70°C. For all
540 experiments, an infection rate of over 95% was achieved at DIV 14-16.
541

542 **Microscopy**

543 **Live-imaging of SV recycling**

544 For live-imaging of Synaptophysin and vesicular glutamate transporter 1 (vGLUT1) recycling, SV
545 proteins fused to the green-fluorescent protein-based pH-sensitive fluorescent reporter pHluorin at
546 their luminal domain were overexpressed by plasmid transfection (Synaptophysin-pHluorin; DIV
547 7) or lentiviral transduction (vGLUT1-pHluorin; DIV 2).

548 For following endogenous vesicular gamma-aminobutyric acid transporter (vGAT) recycling,
549 spontaneously active synaptic boutons were labeled by incubating cells with CypHer5E-
550 conjugated antibodies against the luminal domain of vGAT (1:500 from a 1 mg/ml stock; Synaptic
551 Systems; Cat#131,103CpH) for 2 h in their respective conditioned culture media at 37 °C and 5 %
552 CO_2 prior to imaging.

553 To investigate kinetics of SV recycling, neurons at DIV 14-16 were placed into an RC-
554 47FSLP stimulation chamber (Warner Instruments) in osmolarity-adjusted imaging buffer [170
555 mM sodium chloride (NaCl), 20 mM N-Tris(hydroxyl-methyl)-methyl-2-aminoethane-sulphonic
556 acid (TES), 5 mM Glucose, 5 mM sodium hydrogencabonate ($NaHCO_3$), 3.5 mM potassium
557 chloride (KCl), 1.3 mM $CaCl_2$, 1.2 mM sodium sulfate (Na_2SO_4), 1.2 mM magnesium chloride
558 ($MgCl_2$), 0.4 mM potassium dihydrogenphosphate (KH_2PO_4), 50 µM *(2R)*-amino-5-
559 phosphonovaleric acid (AP5) and 10 µM 6-cyano-7-nitroquinoxaline-2,3-dione (CNQX); pH 7.4]
560 at 37°C (Tempcontrol 37-2 digital). Cells were subjected to electrical field-stimulation (MultiStim
561 System-D330; Digimeter Ltd.) with annotated stimulation trains to evoke action potentials (APs)
562 [40 Hz, 5s (200 APs), 40 Hz, 2s (80 APs), 20 Hz, 2s (40 APs); at 100 mA]. Following changes in
563 fluorescence were tracked by an inverted Zeiss Axiovert 200M microscope, equipped with a 40x
564 oil-immersion EC Plan Neofluar objective (NA 1.30), an EM-CCD camera (Evolve Delta 512)
565 and a pE-300^{white} LED light source (CoolLED). The scanning format was set to 512 x 512 pixels

566 with 16-bit sampling. eGFP (Excitation: BP470-40; Emission: BP535-50; Zeiss filter set 38) or
567 Cy5 (Excitation: BP640-30; Emission: BP525-50; Zeiss filter set 50) filter sets were used for
568 pHluorin or CypHer assays, respectively. Images were acquired at 0.5 Hz frame rate for 100 s with
569 50 (Syph-pHluorin) or 100 (vGLUT1-pH, vGAT-CypHer) ms exposure with an electron
570 multiplying gain of 250 operated through Fiji-based MicroManager 4.11 software.

571 Analysis of responding boutons was performed through custom written macros to identify
572 regions of interest (ROIs) (https://github.com/DennisVoll/pHluorin_ROI_selector/) in an
573 automated manner using SynActJ (Schmied *et al*, 2021). Such analysis averaged fluorescence for
574 each time point in an image series (video) of at least > 20 responding boutons and corrected values
575 for background fluorescence yielding raw background-corrected fluorescence (F). The fold
576 increase of fluorescence after stimulation (F_{max}) can serve as a measure for exocytic fusion and is
577 calculated by normalising F by the mean intensity of F before stimulation (Baseline/basal
578 fluorescence (F_0) = mean intensity of first 5 frames for pHluorin; first 10 frames for CypHer) for
579 each time point (surface normalisation = F/F_0 for pHluorin; $F_0 – F_{min}$ for CypHer). To account for
580 boutons with varying pHluorin expression in one image series and to compare reacidification
581 kinetics, the fluorescence of each time point was subtracted by the basal fluorescence (F_0) to yield
582 ΔF ($F-F_0$), which was then normalised by its peak value (ΔF_{max}). Resulting peak normalised curves
583 ($\Delta F/ \Delta F_{max}$) are annotated as norm. ΔF. Endocytic decay constants (τ) were calculated by averaging
584 and then fitting the norm. ΔF ($\Delta F/\Delta F_{max}$) traces of all videos in one condition (N) to a mono-
585 exponential decay curve [$y_0 + A*e^{(-t/\tau)}$] with the constraints of $y_0 = 1$ and offset = 0 in Prism 9
586 (Graphpad).

587 CypHer-traces had to be corrected for photobleaching: The decay constant of the bleaching curve
588 was determined by fitting the data points of the first 10 frames (20 s, prior to stimulation) to a
589 mono-exponential decay curve. The corresponding value of the photobleaching curve at a given

590 time *t* was added to the raw fluorescence intensity measured at each corresponding time point to
591 correct for the loss of intensity due to bleaching.
592
593 **Immunocytochemistry**
594 For immunostainings, neuronal cultures were chemically fixed on DIV 14-16 using 4 % p-
595 formaldehyde (PFA) and 4 % sucrose in phosphate buffered saline (PBS) for 15 min at room
596 temperature (RT). For experiments in Figure 3C, G-I, cultures were stimulated with a 40 Hz train
597 for 5 s in imaging buffer before immediate fixation. After fixation, cells were washed thrice with
598 PBS and incubated with permeabilization buffer (10% normal goat serum, 0.3 % Triton X-100 in
599 PBS) for 30 min at RT, followed by primary antibody incubation of proteins of interest in
600 permeabilization buffer at indicated dilutions (see Key Resource Table) at 4°C overnight.
601 Subsequently, unbound antibodies were removed by three PBS washes while bound antibodies
602 were decorated by corresponding fluorophore-coupled secondary antibodies in permeabilization
603 buffer for 1h at RT. For F-Actin staining, Phalloidin-Alexa Fluor™ 594 (1:1000 stock; AAT
604 Bioquest; Cat# ABD-23158) was added in the secondary incubation step. Finally, neurons were
605 washed thrice with PBS, followed by two washes with ultra-pure water. Coverslips were dried for
606 2 h before mounting in ProLong™ Gold Antifade (Thermo Fisher Scientific; #P36934) on glass
607 slides (Thermo Fisher Scientific; VWR; Cat#630-1985). The slides were cured for at least 72 h at
608 RT before imaging.
609 **Multicolor time-gated STED imaging**
610 STED images were acquired from fixed samples by a HC PL APO CS2 100 x oil objective (1.40
611 NA) on a Leica SP8 TCS STED 3x microscope (Leica Microsystems) equipped with a pulsed
612 white-light excitation laser (WLL; ~ 80 ps pulse width, 80 MHz repetition rate; NKT Photonics)
613 and a STED laser for depletion (775 nm). The scanning format was set to 1024 x 1024 pixels, with

614 8-bit sampling, 4x line averaging, 4x frame accumulation and 6 x optical zoom, yielding a final
615 pixel size of 18.9 nm. Three-color imaging was performed by sequentially exciting following
616 fluorophores (excitation filter = Exf; emission filter = Emf): Atto647N (Exf: 640 nm; Emf: 650-
617 700 nm); Alexa Fluor™ 594 (Exf: 590 nm; Emf: 600-640 nm) and Atto542 (Exf: 540 nm; Emf:
618 550-580 nm) operated by the Leica Application Suite X (Leica Microsystems, 2020). For
619 stimulated depletion of the signal, the 775 nm STED laser was applied to all emissions. Detection
620 of the resulting signal was time-gated by 0.3-6 ns to allow enough time for stimulated depletion
621 and collected by two sensitive HyD detectors at appropriate spectral regions distinct from the
622 STED laser wavelength. Settings in independent experiments were similar between conditions to
623 allow quantification of signals. Raw data obtained from three-channel time-gated STED (gSTED)
624 imaging were analyzed with Fiji. For analysis, only synapses oriented in the xy-plane exhibiting a
625 clear separation of Bassoon (presynapse) and Homer1 (postsynapse) clusters were taken into
626 account. To determine synaptic localisation and presynaptic levels of proteins of interest,
627 multicolor line profiles were measured: A line (1.0 µm length, 0.4 µm width) perpendicular to the
628 synaptic cleft (space between Bassoon & Homer1 cluster) was drawn (Gerth *et al.*, 2017) and
629 fluorescence intensity of all three channels along this line was measured using a Fiji Macro
630 (Macro_plot_lineprofile_multicolor; Dr. Kees Straatman, University of Leicester, UK). Resulting
631 profiles were aligned to the maximum Bassoon intensity, which was set to 0 nm. For localization
632 analysis, all three profiles were normalized to their maxima, which were set to 1. For quantification
633 of presynaptic protein levels, only the fractions of the non-normalized line profiles of proteins of
634 interest overlapping with the normalized averaged Bassoon distribution (between 151.4 and -37.8
635 nm; Figure 3-Supplement 1H) were integrated. Intensities were normalized to controls (DMSO,
636 shCTR, WT) which were set to 100.
637

638 **Imaging of endogenous β-Actin levels**

639 To visualize endogenous β-Actin levels, eGFP knockin following the ORANGE method was
640 performed (Willems *et al.*, 2020): Neurons were transfected with vGLUT1-mCherry (Franck
641 Polleux) and pOrange GFP-β-Actin KI (Addgene; Cat#131479) by $CaCl_2$ on DIV 2. Directly
642 following transfection, cells were transduced with shCTR or shmDia1+3 lentiviral particles
643 carrying BFP as a reporter to prevent crosstalk between mCherry and NLS-RFP expression.
644 Neuronal cultures were chemically fixed on DIV 15. After fixation, endogenous GFP and
645 overexpressed vGLUT1-mCherry intensities were enhanced by additional antibody (anti-GFP and
646 anti-RFP; see Key Resource Table) incubation according to the immunocytochemistry protocol
647 described above. Images of neurons were taken on the STED microscope with and without
648 stimulated depletion (confocal) with the same settings as indicated above. For analysis, confocal
649 images were filtered by Gaussian blur (sigma = 2 pixel) and auto-thresholded using Otsu's method.
650 Whenever confocal vGLUT1 signal co-localized with confocal Actin clusters, the area was chosen
651 as a ROI. Actin intensity was then measured in the ROI applied to the STED image. The intensities
652 of β-Actin were normalized to shCTR which was set to 100.

653

654 **Transmission electron microscopy**

655 To investigate synaptic effects of F-actin manipulations at the ultrastructural level, cells on
656 coverslips were chemically fixed with 2 % glutaraldehyde in cacodylat buffer (CDB; 0.1 M sodium
657 cacodylat) for 1 h at RT. Coverslips were washed thrice with CDB before osmification by 1 %
658 (w/v) osmium tetroxide (OsO_4) and 1.5 % (w/v) potassium hexacyanoferrat ($K_3Fe(CN)_6$) in CBD
659 for 1 h at 4°C. After postfixation, cells were stained with 1 % (w/v) uranyl acetate, dehydrated by
660 methanol gradients and finally embedded by epoxy resin (Sigma Aldrich; Cat# 45359) infiltration.
661 After polymerization (60°C, 30 h), coverslips were removed and ultra-thin (70 nm) sections were

662 cut and contrasted with 2 % (w/v) uranyl acetate and 80 mM lead citrate. 8-bit Images were
663 obtained on a Zeiss 900 transmission electron microscope equipped with Olympus MegaViewIII
664 or Olympus Morada G2 digital cameras at 30000 x magnification yielding a pixel size of 1.07 nm.
665 Subsequently, morphometry (density of synaptic vesicles, endosome-like vacuoles, clathrin-
666 coated vesicles, clathrin-coated pits and non-coated invaginations) was analyzed from synaptic
667 profiles with clearly distinguishable active zones and adjacent synaptic vesicles in a blinded
668 manner.
669
670 **Biochemistry**
671 **Immunoblotting**
672 To compare protein levels between experimental conditions, immunoblotting was performed:
673 Protein concentrations in lysates were measured by BCA assay (Thermo Fisher Scientific;
674 Cat#23227) and equal protein amounts were diluted in Laemmli sample buffer [final (1 x)
675 concentration: 31.5 mM 2-Amino-2-(hydroxymethyl)propane-1,3-diol (Tris), 1 % (w/v) sodium
676 dodecyl sulfate (SDS), 10 % (v/v) glycerol, 0.001% (w/v) 3,3-Bis(3,5-dibromo-4-hydroxyphenyl)-
677 2,1λ^6-benzoxathiole-1,1(3*H*)-dione (bromophenol blue), 5 % (v/v) 2-mercaptoethanol; pH 6.8]
678 and denatured at 55°C for 20 min (unless indicated otherwise). Samples were resolved by SDS-
679 polyacrylamide gel electrophoresis (SDS-PAGE) with self-made Bis(2-hydroxyethyl)amino-
680 tris(hydroxymethyl)methan (BisTris; 250 mM) based 4-20 % polyacrylamide (Rotiphorese Gel
681 30; Carl Roth) gradient gels and run (80-120 V; 90 min) in NuPAGE MOPS SDS running buffer
682 (Thermo Fisher Scientific; Cat#NP000102) using Mini-PROTEAN Tetra Vertical Electrophoresis
683 Cells (Bio-Rad, Cat#1658004). For membrane fractionation experiments, RFP-fluorescence of
684 mDia1 variants in respective fractions was imaged in-gel on a ChemiDoc XRS+ (Bio-Rad)
685 controlled by the Image Lab software (version 6.0.1) utilizing the Alexa546 preset (605/50 Filter3;

686 Light Green Epi illumination). Separated proteins were wet-blotted (110 V; 90 min; 4°C) on
687 fluorescence-optimized polyvinylidene difluoride (PVDF) membranes (Immobilon-FL; Merck;
688 IPFL00010) in transfer buffer (25 mM Tris (pH 7.6), 192 mM glycine, 20% (v/v) methanol, 0.03%
689 (w/v) SDS). Subsequently, membranes were blocked with blocking buffer [5 % bovine serum
690 albumin (BSA), in Tris-buffered saline (TBS) containing 0.01% Tween 20 (TBS-T)] for 1 h at RT
691 and incubated (4 °C; overnight) with primary antibodies under constant agitation at indicated
692 dilutions (s. Key Resource Table) in blocking buffer. Membranes were washed thrice with TBS-T
693 and incubated with corresponding pairs of IRDye 680RD- or 800CW-conjugated secondary
694 antibodies in TBS-T for 1 h at RT. After three washes with TBS-T, bound antibodies were
695 visualized by the Odyssey Fc Imaging System (LI-COR Biosciences) controlled and analyzed by
696 Image Studio Lite (Version 5.2.5). For colorimetric analysis of protein levels, intensity of bands
697 was measured by assigning shapes of equal size to all lanes at similar heights and subtracting the
698 individual background for each shape. Signals were normalized to controls on the same blot. The
699 PageRuler Prestained (Thermo Fisher Scientific; Cat#26616) was used as a ladder to control for
700 protein size.
701
702 **Immunoprecipitation from synaptosomes**
703 To immunoprecipitate synaptic mDia1, synaptosomes (P2') were prepared as follows: One mouse
704 brain (p28) was homogenized (900 rpm; 12 strokes with glass-teflon homogenizer) in 7 mL of ice-
705 cold homogenization buffer [(320 mM sucrose, 4 mM HEPES; pH 7.4) supplemented with
706 mammalian protease inhibitor cocktail (PIC)] at 4°C. Large cellular debris and nuclei were
707 sedimented by centrifugation at 900 g for 10 min at 4°C. The supernatant was further centrifuged
708 at 12500 g for 15 min at 4°C. The resulting pellet (P2) was resuspended in 15 mL of
709 homogenization buffer and pelleted at 12500 g for 15 min at 4°C yielding the crude synaptosomal

710 fraction P2'. Subsequently, the pellet was resuspended in 2 mL of immunoprecipitation buffer [20
711 mM HEPES, 130 mM NaCl, 2 mM $MgCl_2$, 1 % (w/v)
712 3-[Dimethyl[3-(3α,7α,12α-trihydroxy-5β-cholan-24-amido)propyl]azaniumyl]propane-1-
713 sulfonate (CHAPS), PIC, phosphatase inhibitor cocktail II and III (Sigma-Aldrich); pH 7.4] and
714 lysed for 30 min at 4°C under light agitation. The lysate was cleared by centrifugation at 15000 g
715 at 4°C and protein concentration was measured using the BCA assay.

716 For identification of the protein environment of mDia1, P2' lysate (2 mg; 2 g/L) was
717 incubated with either 2 µg of anti-mDia1 antibody (BD Biosciences, Cat# 610848) or equal
718 amounts of immunoglobulin G (IgG) isotype control mouse antibody (Thermo Fisher Scientific;
719 Cat# 31903; RRID:AB_10959891) for 1 h at 4°C before the addition of 25 µL of Pierce Protein
720 A/G Magnetic Beads (Thermo Fisher Scientific) for an additional 2 h under constant rotation.
721 Subsequently, unbound proteins were removed from the beads by three consecutive wash cycles
722 with immunoprecipitation buffer. Bound proteins were eluted and boiled (10 min; 95°C) in 2x
723 Laemmli buffer, resolved by SDS-PAGE and analyzed by immunoblotting.

724

725 **LC-MS analysis of protein environment of mDia1**

726 For the analysis of interaction partners of synaptic mDia1, mDia1 was immunoprecipitated from
727 synaptosomes as described above. Eluted proteins were reduced (5 mM dithiothreitol; 30 min at
728 55°C), alkylated (15 mM iodoacetamide; 20 min at RT in the dark), and submitted to LC-MS
729 analysis: Proteins were subjected to SDS-PAGE following excision of 3 bands per lane and in-gel
730 digestion of proteins by trypsin (1:100 (w/w); overnight at 37°C). Resulting tryptic peptides were
731 separated by reverse-phase high-performance liquid chromatography (RP-HPLC; Ultimate™
732 3000 RSLCnano system; Thermo Scientific) using a 50 cm analytical column (in-house packed
733 with Poroshell 120 EC-C18; 2.7 µm; Agilent Technologies) with a 120 min gradient. RP-HPLC

734 was coupled on-line to an Orbitrap Elite mass spectrometer (Thermo Fisher Scientific) that
735 performed precursor ion (MS1) scans at a mass resolution of 60000, while fragment ion (MS2)
736 scans were acquired with an automatic gain control (AGC) target of 5 x 10^3 and a maximum
737 injection time of 50 ms. Data analysis including label free quantification was performed with
738 MaxQuant (version 1.6.1.0) using the following parameters: The initial maximum mass deviation
739 of the precursor ions was set at 4.5 parts per million (ppm), and the maximum mass deviation of
740 the fragment ions was set at 0.5 Da. Cysteine carbamidometyl and propionamide, Methionine
741 oxidation and N-terminal acetylation were set as variable modifications. For identification of
742 proteins, data were searched against the SwissProt murine database (Mouse_2016oktuniprot-
743 proteome%3AUP000000589.fasta). False discovery rates were < 1 % at the protein level based on
744 matches to reversed sequences in the concatenated target-decoy database. The statistical analysis
745 was done with Perseus (version 1.6.7.0).
746
747 **Effector pulldown assays**
748 To analyze the activity of small Rho GTPases, pulldowns utilizing effector protein domains which
749 exclusively bind to their GTP-bound forms were performed: Neurons (200 000 cells) were washed
750 with ice-cold PBS and harvested in GTPase lysis buffer (50 mM HEPES, 500 mM NaCl, 10mM
751 $MgCl_2$, PIC, phosphatase Inhibitor cocktails II + III; pH 7.4). Cells were lysed for 5 min under
752 repetitive mixing before centrifugation (15000 g; 5 min; 4°C). Cleared lysates were incubated with
753 Rhotekin-Rho binding domain (RBD) beads (60 µg; Cytoskeleton Inc.) or with PAK-p21 binding
754 domain (PBD) beads (20 µg; Cytoskeleton Inc.) at 4°C under constant rotation to bind active RhoA
755 or Cdc42 and Rac1, respectively. After 2 h, the beads were pelleted by centrifugation (1000 g; 1
756 min; 4°C) and washed with washing buffer (50 mM HEPES, 150 mM NaCl, 10 mM $MgCl_2$; pH
757 7.4). After repeated centrifugation, unbound proteins were discarded with the supernatant, while

758 bound proteins were eluted from the beads by addition of 2 x Laemmli buffer and boiling (10 min;
759 95°C). Finally, activity of small Rho GTPases was resolved by SDS-PAGE and analyzed by
760 immunoblotting input and pulldown samples.
761
762 **Membrane fractionation**
763 To characterize membrane association of the truncation mDia1 mutant, HEK293T cells were
764 transfected with wild-type (mDia1-WT) or mDia1 truncation mutant (mDia1-ΔN) using $CaCl_2$.
765 48 h after transfection cells were washed with ice-cold PBS and harvested in ice-cold resuspension
766 buffer (20 mM HEPES, 130 mM NaCl, PIC; pH 7.4). Cells were lysed by forcing the suspension
767 through 18-gauge syringes to crack the plasma membrane in between three freeze-thaw cycles in
768 liquid nitrogen. Nuclei were removed by centrifugation at 1000 g for 5 min at 4°C. The supernatant
769 (total lysate) was sedimented at 100000 g for 30 min at 4°C to yield the membrane fraction as the
770 pellet and the cytosolic fraction as the high-speed supernatant. The pellet was resuspended in
771 resuspension buffer to the same volume of the cytosolic fraction. Equal volumes of all fractions
772 were analyzed by SDS-PAGE and immunoblotting to allow interpretation of protein enrichment
773 in cytosolic or membrane fractions with respect to the total lysate.
774
775 **Statistical analysis**
776 All data in this study are presented as the mean ± standard error of the mean (SEM) and was
777 obtained from *N* independent experiments with a total sample number of *n* (e.g., number of images,
778 videos, synapses, etc.) as annotated in the Figure legends. For analysis of protein levels in STED
779 microscopy and synaptic structures in EM, statistical differences between groups were calculated
780 considering *n*, while in all other experiments statistical differences were calculated between
781 independent experiments *N* (In pHluorin/CypHer assays, at least 20 responding boutons/video

were analyzed). For n > 100 or N > 5, data were tested for Gaussian distribution following D'Agostino-Pearson tests to determine parametric versus non-parametric statistical testing. The statistical significance between two groups was evaluated with either two-tailed unpaired student's t-tests for normally distributed data or two-tailed unpaired Mann-Whitney tests, if data did not follow Gaussian distribution. In experiments that necessitated normalization (to 100 or 1) before analysis, one-sample t-tests or one-sample Wilcoxon rank tests were performed for normal and non-normal distributed data, respectively. The statistical significance between more than two experimental groups of normally distributed data was analyzed by one-way ANOVA, followed by a Tukey's post hoc test, while Kruskal-Wallis tests with post hoc Dunn's multiple comparison test were used when datasets did not follow Gaussian distribution.

Corresponding statistical tests are indicated in the Figure and significance levels are annotated as asterisks (*$p < 0.05$, **$p < 0.01$, ***$p < 0.001$, and ****$p < 0.0001$). Differences that are not significant are not stated or indicated as ns ($p > 0.05$). Statistical data evaluation was performed using GraphPad Prism 9.5.1 (733) and all calculated p-values are annotated in the source data table. All Figures were assembled using Affinity Designer (version 1.10.6.1665).

Data availability

All data generated and analyzed in this study are included in the manuscript and supporting files. Numerical data as well as raw images of western blots are provided as source data files. Values from the same experiment (N) are shaded in similar colors.

Contact for Reagent and Resource Sharing

Further information and requests for resources and reagents should be directed to and will be fulfilled by the corresponding contact V.H. (Haucke@fmp-berlin.de).

ACKNOWLEDGEMENTS

We are indebted to Sabine Hahn, Delia Löwe and Silke Zillmann for expert technical assistance with the preparation of neuronal cultures. We further wish to thank Dr. Martin Lehmann (FMP, Berlin), Hannah Gelhaus and Gresy Bregu (both FU Berlin) for aid with STED imaging, Dr. Dmytro Puchkov (FMP Imaging Core Facility) for supervising electron microscopy analysis, and Heike Stephanowitz and Prof. Fan Liu (FMP Core Facility Proteomics) for proteomic analyses. Supported by grants from the Deutsche Forschungsgemeinschaft (SFB958/ TP A01) to V.H..

815 **REFERENCES**

816 Anes E, Kuhnel MP, Bos E, Moniz-Pereira J, Habermann A, Griffiths G (2003) Selected lipids
817 activate phagosome actin assembly and maturation resulting in killing of pathogenic mycobacteria.
818 *Nat Cell Biol* 5: 793-802

819 Bingham D, Jakobs CE, Wernert F, Boroni-Rueda F, Jullien N, Schentarra EM, Friedl K, Da Costa
820 Moura J, van Bommel DM, Caillol G *et al* (2023) Presynapses contain distinct actin
821 nanostructures. *J Cell Biol* 222

822 Bleckert A, Photowala H, Alford S (2012) Dual pools of actin at presynaptic terminals. *J*
823 *Neurophysiol* 107: 3479-3492

824 Bloom O, Evergren E, Tomilin N, Kjaerulff O, Low P, Brodin L, Pieribone VA, Greengard P,
825 Shupliakov O (2003) Colocalization of synapsin and actin during synaptic vesicle recycling. *J Cell*
826 *Biol* 161: 737-747

827 Borst JG, Soria van Hoeve J (2012) The calyx of Held synapse: from model synapse to auditory
828 relay. *Annu Rev Physiol* 74: 199-224

829 Boucrot E, Ferreira AP, Almeida-Souza L, Debard S, Vallis Y, Howard G, Bertot L, Sauvonnet
830 N, McMahon HT (2015) Endophilin marks and controls a clathrin-independent endocytic
831 pathway. *Nature* 517: 460-465

832 Boulant S, Kural C, Zeeh JC, Ubelmann F, Kirchhausen T (2011) Actin dynamics counteract
833 membrane tension during clathrin-mediated endocytosis. *Nat Cell Biol* 13: 1124-1131

834 Chanaday NL, Cousin MA, Milosevic I, Watanabe S, Morgan JR (2019) The Synaptic Vesicle
835 Cycle Revisited: New Insights into the Modes and Mechanisms. *J Neurosci* 39: 8209-8216

836 Chanaday NL, Kavalali ET (2018) Optical detection of three modes of endocytosis at hippocampal
837 synapses. *Elife* 7

838 Chandrasekar I, Huettner JE, Turney SG, Bridgman PC (2013) Myosin II regulates activity
839 dependent compensatory endocytosis at central synapses. *J Neurosci* 33: 16131-16145
840 Chauhan BK, Lou M, Zheng Y, Lang RA (2011) Balanced Rac1 and RhoA activities regulate cell
841 shape and drive invagination morphogenesis in epithelia. *Proc Natl Acad Sci U S A* 108: 18289-
842 18294
843 Chen X, Wu X, Wu H, Zhang M (2020) Phase separation at the synapse. *Nat Neurosci* 23: 301-
844 310
845 Cingolani LA, Goda Y (2008) Actin in action: the interplay between the actin cytoskeleton and
846 synaptic efficacy. *Nat Rev Neurosci* 9: 344-356
847 Clayton EL, Cousin MA (2009) The molecular physiology of activity-dependent bulk endocytosis
848 of synaptic vesicles. *J Neurochem* 111: 901-914
849 Colgan LA, Yasuda R (2014) Plasticity of dendritic spines: subcompartmentalization of signaling.
850 *Annu Rev Physiol* 76: 365-385
851 Dani A, Huang B, Bergan J, Dulac C, Zhuang X (2010) Superresolution imaging of chemical
852 synapses in the brain. *Neuron* 68: 843-856
853 Daou P, Hasan S, Breitsprecher D, Baudelet E, Camoin L, Audebert S, Goode BL, Badache A
854 (2014) Essential and nonredundant roles for Diaphanous formins in cortical microtubule capture
855 and directed cell migration. *Mol Biol Cell* 25: 658-668
856 Deguchi Y, Harada M, Shinohara R, Lazarus M, Cherasse Y, Urade Y, Yamada D, Sekiguchi M,
857 Watanabe D, Furuyashiki T *et al* (2016) mDia and ROCK Mediate Actin-Dependent Presynaptic
858 Remodeling Regulating Synaptic Efficacy and Anxiety. *Cell Rep* 17: 2405-2417
859 Del Signore SJ, Kelley CF, Messelaar EM, Lemos T, Marchan MF, Ermanoska B, Mund M, Fai
860 TG, Kaksonen M, Rodal AA (2021) An autoinhibitory clamp of actin assembly constrains and
861 directs synaptic endocytosis. *Elife* 10

862 Delvendahl I, Vyleta NP, von Gersdorff H, Hallermann S (2016) Fast, Temperature-Sensitive and
863 Clathrin-Independent Endocytosis at Central Synapses. *Neuron* 90: 492-498
864 Eisenmann KM, Peng J, Wallar BJ, Alberts AS (2005) Rho GTPase-formin pairs in cytoskeletal
865 remodelling. *Novartis Found Symp* 269: 206-218; discussion 219-230
866 Engqvist-Goldstein AE, Drubin DG (2003) Actin assembly and endocytosis: from yeast to
867 mammals. *Annu Rev Cell Dev Biol* 19: 287-332
868 Ferguson SM, Brasnjo G, Hayashi M, Wolfel M, Collesi C, Giovedi S, Raimondi A, Gong LW,
869 Ariel P, Paradise S *et al* (2007) A selective activity-dependent requirement for dynamin 1 in
870 synaptic vesicle endocytosis. *Science* 316: 570-574
871 Ferguson SM, Raimondi A, Paradise S, Shen H, Mesaki K, Ferguson A, Destaing O, Ko G,
872 Takasaki J, Cremona O *et al* (2009) Coordinated actions of actin and BAR proteins upstream of
873 dynamin at endocytic clathrin-coated pits. *Dev Cell* 17: 811-822
874 Gan Q, Watanabe S (2018) Synaptic Vesicle Endocytosis in Different Model Systems. *Front Cell*
875 *Neurosci* 12: 171
876 Ganguly A, Tang Y, Wang L, Ladt K, Loi J, Dargent B, Leterrier C, Roy S (2015) A dynamic
877 formin-dependent deep F-actin network in axons. *J Cell Biol* 210: 401-417
878 Gerth F, Japel M, Pechstein A, Kochlamazashvili G, Lehmann M, Puchkov D, Onofri F, Benfenati
879 F, Nikonenko AG, Fredrich K *et al* (2017) Intersectin associates with synapsin and regulates its
880 nanoscale localization and function. *Proc Natl Acad Sci U S A* 114: 12057-12062
881 Goode BL, Eck MJ (2007) Mechanism and function of formins in the control of actin assembly.
882 *Annu Rev Biochem* 76: 593-627
883 Gormal R, Valmas N, Fath T, Meunier F (2017) A role for tropomyosins in activity-dependent
884 bulk endocytosis? *Mol Cell Neurosci* 84: 112-118

885 Gu C, Chang J, Shchedrina VA, Pham VA, Hartwig JH, Suphamungmee W, Lehman W, Hyman
886 BT, Bacskai BJ, Sever S (2014) Regulation of dynamin oligomerization in cells: the role of
887 dynamin-actin interactions and its GTPase activity. *Traffic* 15: 819-838
888 Higashi T, Ikeda T, Shirakawa R, Kondo H, Kawato M, Horiguchi M, Okuda T, Okawa K, Fukai
889 S, Nureki O *et al* (2008) Biochemical characterization of the Rho GTPase-regulated actin assembly
890 by diaphanous-related formins, mDia1 and Daam1, in platelets. *J Biol Chem* 283: 8746-8755
891 Higashida C, Suetsugu S, Tsuji T, Monypenny J, Narumiya S, Watanabe N (2008) G-actin
892 regulates rapid induction of actin nucleation by mDia1 to restore cellular actin polymers. *J Cell*
893 *Sci* 121: 3403-3412
894 Hodge RG, Ridley AJ (2016) Regulating Rho GTPases and their regulators. *Nature reviews*
895 *Molecular cell biology* 17: 496-510
896 Hori T, Eguchi K, Wang HY, Miyasaka T, Guillaud L, Taoufiq Z, Mahapatra S, Yamada H, Takei
897 K, Takahashi T (2022) Microtubule assembly by tau impairs endocytosis and neurotransmission
898 via dynamin sequestration in Alzheimer's disease synapse model. *Elife* 11
899 Hua Y, Sinha R, Thiel CS, Schmidt R, Huve J, Martens H, Hell SW, Egner A, Klingauf J (2011)
900 A readily retrievable pool of synaptic vesicles. *Nat Neurosci* 14: 833-839
901 Imoto Y, Raychaudhuri S, Ma Y, Fenske P, Sandoval E, Itoh K, Blumrich EM, Matsubayashi HT,
902 Mamer L, Zarebidaki F *et al* (2022) Dynamin is primed at endocytic sites for ultrafast endocytosis.
903 *Neuron* 110: 2815-2835 e2813
904 Keine C, Al-Yaari M, Radulovic T, Thomas CI, Valino Ramos P, Guerrero-Given D, Ranjan M,
905 Taschenberger H, Kamasawa N, Young SM, Jr. (2022) Presynaptic Rac1 controls synaptic
906 strength through the regulation of synaptic vesicle priming. *Elife* 11
907 Kessels MM, Qualmann B (2006) Syndapin oligomers interconnect the machineries for endocytic
908 vesicle formation and actin polymerization. *J Biol Chem* 281: 13285-13299

909 Kitzing TM, Sahadevan AS, Brandt DT, Knieling H, Hannemann S, Fackler OT, Grosshans J,
910 Grosse R (2007) Positive feedback between Dia1, LARG, and RhoA regulates cell morphology
911 and invasion. *Genes Dev* 21: 1478-1483
912 Kononenko NL, Haucke V (2015) Molecular mechanisms of presynaptic membrane retrieval and
913 synaptic vesicle reformation. *Neuron* 85: 484-496
914 Kononenko NL, Puchkov D, Classen GA, Walter AM, Pechstein A, Sawade L, Kaempf N,
915 Trimbuch T, Lorenz D, Rosenmund C *et al* (2014) Clathrin/AP-2 mediate synaptic vesicle
916 reformation from endosome-like vacuoles but are not essential for membrane retrieval at central
917 synapses. *Neuron* 82: 981-988
918 Lash LL, Wallar BJ, Turner JD, Vroegop SM, Kilkuskie RE, Kitchen-Goosen SM, Xu HE, Alberts
919 AS (2013) Small-molecule intramimics of formin autoinhibition: a new strategy to target the
920 cytoskeletal remodeling machinery in cancer cells. *Cancer Res* 73: 6793-6803
921 Lawson CD, Ridley AJ (2018) Rho GTPase signaling complexes in cell migration and invasion. *J*
922 *Cell Biol* 217: 447-457
923 Lopez-Hernandez T, Takenaka KI, Mori Y, Kongpracha P, Nagamori S, Haucke V, Takamori S
924 (2022) Clathrin-independent endocytic retrieval of SV proteins mediated by the clathrin adaptor
925 AP-2 at mammalian central synapses. *Elife* 11
926 Macia E, Ehrlich M, Massol R, Boucrot E, Brunner C, Kirchhausen T (2006) Dynasore, a cell-
927 permeable inhibitor of dynamin. *Dev Cell* 10: 839-850
928 Marston DJ, Dickinson S, Nobes CD (2003) Rac-dependent trans-endocytosis of ephrinBs
929 regulates Eph-ephrin contact repulsion. *Nat Cell Biol* 5: 879-888
930 McMahon HT, Boucrot E (2011) Molecular mechanism and physiological functions of clathrin-
931 mediated endocytosis. *Nature reviews Molecular cell biology* 12: 517-533

932 Merrifield CJ, Perrais D, Zenisek D (2005) Coupling between clathrin-coated-pit invagination,
933 cortactin recruitment, and membrane scission observed in live cells. *Cell* 121: 593-606
934 Miesenbock G, De Angelis DA, Rothman JE (1998) Visualizing secretion and synaptic
935 transmission with pH-sensitive green fluorescent proteins. *Nature* 394: 192-195
936 Muller PM, Rademacher J, Bagshaw RD, Wortmann C, Barth C, van Unen J, Alp KM, Giudice
937 G, Eccles RL, Heinrich LE *et al* (2020) Systems analysis of RhoGEF and RhoGAP regulatory
938 proteins reveals spatially organized RAC1 signalling from integrin adhesions. *Nat Cell Biol* 22:
939 498-511
940 O'Neil SD, Racz B, Brown WE, Gao Y, Soderblom EJ, Yasuda R, Soderling SH (2021) Action
941 potential-coupled Rho GTPase signaling drives presynaptic plasticity. *Elife* 10
942 Ogunmowo TH, Jing H, Raychaudhuri S, Kusick GF, Imoto Y, Li S, Itoh K, Ma Y, Jafri H, Dalva
943 MB *et al* (2023) Membrane compression by synaptic vesicle exocytosis triggers ultrafast
944 endocytosis. *Nat Commun* 14: 2888
945 Otomo T, Otomo C, Tomchick DR, Machius M, Rosen MK (2005) Structural basis of Rho
946 GTPase-mediated activation of the formin mDia1. *Mol Cell* 18: 273-281
947 Peng GE, Wilson SR, Weiner OD (2011) A pharmacological cocktail for arresting actin dynamics
948 in living cells. *Mol Biol Cell* 22: 3986-3994
949 Peng J, Kitchen SM, West RA, Sigler R, Eisenmann KM, Alberts AS (2007) Myeloproliferative
950 defects following targeting of the Drf1 gene encoding the mammalian diaphanous related formin
951 mDia1. *Cancer Res* 67: 7565-7571
952 Peng J, Wallar BJ, Flanders A, Swiatek PJ, Alberts AS (2003) Disruption of the Diaphanous-
953 related formin Drf1 gene encoding mDia1 reveals a role for Drf3 as an effector for Cdc42. *Curr*
954 *Biol* 13: 534-545

955 Piriya Ananda Babu L, Wang HY, Eguchi K, Guillaud L, Takahashi T (2020) Microtubule and
956 Actin Differentially Regulate Synaptic Vesicle Cycling to Maintain High-Frequency
957 Neurotransmission. *J Neurosci* 40: 131-142
958 Raimondi A, Ferguson SM, Lou X, Armbruster M, Paradise S, Giovedi S, Messa M, Kono N,
959 Takasaki J, Cappello V *et al* (2011) Overlapping role of dynamin isoforms in synaptic vesicle
960 endocytosis. *Neuron* 70: 1100-1114
961 Ramalingam N, Zhao H, Breitsprecher D, Lappalainen P, Faix J, Schleicher M (2010)
962 Phospholipids regulate localization and activity of mDia1 formin. *Eur J Cell Biol* 89: 723-732
963 Renard HF, Simunovic M, Lemiere J, Boucrot E, Garcia-Castillo MD, Arumugam S, Chambon V,
964 Lamaze C, Wunder C, Kenworthy AK *et al* (2015) Endophilin-A2 functions in membrane scission
965 in clathrin-independent endocytosis. *Nature* 517: 493-496
966 Richards DA, Rizzoli SO, Betz WJ (2004) Effects of wortmannin and latrunculin A on slow
967 endocytosis at the frog neuromuscular junction. *J Physiol* 557: 77-91
968 Ritter B, Ferguson SM, De Camilli P, McPherson PS (2017) A lentiviral system for efficient
969 knockdown of proteins in neuronal cultures [version 1; referees: 2 approved]. *MNI Open Res* 1
970 Roux A, Uyhazi K, Frost A, De Camilli P (2006) GTP-dependent twisting of dynamin implicates
971 constriction and tension in membrane fission. *Nature* 441: 528-531
972 Saffarian S, Cocucci E, Kirchhausen T (2009) Distinct dynamics of endocytic clathrin-coated pits
973 and coated plaques. *PLoS Biol* 7: e1000191
974 Saheki Y, De Camilli P (2012) Synaptic vesicle endocytosis. *Cold Spring Harbor perspectives in*
975 *biology* 4: a005645
976 Sakaba T, Kononenko NL, Bacetic J, Pechstein A, Schmoranzer J, Yao L, Barth H, Shupliakov O,
977 Kobler O, Aktories K *et al* (2013) Fast neurotransmitter release regulated by the endocytic scaffold
978 intersectin. *Proc Natl Acad Sci U S A* 110: 8266-8271

979 Sakaba T, Neher E (2003) Involvement of actin polymerization in vesicle recruitment at the calyx
980 of Held synapse. *J Neurosci* 23: 837-846
981 Sankaranarayanan S, Atluri PP, Ryan TA (2003) Actin has a molecular scaffolding, not propulsive,
982 role in presynaptic function. *Nat Neurosci* 6: 127-135
983 Schmied C, Soykan T, Bolz S, Haucke V, Lehmann M (2021) SynActJ: Easy-to-Use Automated
984 Analysis of Synaptic Activity. *Front Comp Sci-Switz* 3
985 Shinohara R, Thumkeo D, Kamijo H, Kaneko N, Sawamoto K, Watanabe K, Takebayashi H,
986 Kiyonari H, Ishizaki T, Furuyashiki T *et al* (2012) A role for mDia, a Rho-regulated actin
987 nucleator, in tangential migration of interneuron precursors. *Nat Neurosci* 15: 373-380, S371-372
988 Shupliakov O, Bloom O, Gustafsson JS, Kjaerulff O, Low P, Tomilin N, Pieribone VA, Greengard
989 P, Brodin L (2002) Impaired recycling of synaptic vesicles after acute perturbation of the
990 presynaptic actin cytoskeleton. *Proc Natl Acad Sci U S A* 99: 14476-14481
991 Soykan T, Kaempf N, Sakaba T, Vollweiter D, Goerdeler F, Puchkov D, Kononenko NL, Haucke
992 V (2017) Synaptic Vesicle Endocytosis Occurs on Multiple Timescales and Is Mediated by
993 Formin-Dependent Actin Assembly. *Neuron* 93: 854-866 e854
994 Soykan T, Maritzen T, Haucke V (2016) Modes and mechanisms of synaptic vesicle recycling.
995 *Curr Opin Neurobiol* 39: 17-23
996 Watanabe S, Boucrot E (2017) Fast and ultrafast endocytosis. *Curr Opin Cell Biol* 47: 64-71
997 Watanabe S, Rost BR, Camacho-Perez M, Davis MW, Sohl-Kielczynski B, Rosenmund C,
998 Jorgensen EM (2013) Ultrafast endocytosis at mouse hippocampal synapses. *Nature* 504: 242-247
999 Watanabe S, Trimbuch T, Camacho-Perez M, Rost BR, Brokowski B, Sohl-Kielczynski B, Felies
1000 A, Davis MW, Rosenmund C, Jorgensen EM (2014) Clathrin regenerates synaptic vesicles from
1001 endosomes. *Nature* 515: 228-233

1002 Willems J, de Jong APH, Scheefhals N, Mertens E, Catsburg LAE, Poorthuis RB, de Winter F,
1003 Verhaagen J, Meye FJ, MacGillavry HD (2020) ORANGE: A CRISPR/Cas9-based genome
1004 editing toolbox for epitope tagging of endogenous proteins in neurons. *PLoS Biol* 18: e3000665
1005 Wu LG, Chan CY (2022) Multiple Roles of Actin in Exo- and Endocytosis. *Front Synaptic*
1006 *Neurosci* 14: 841704
1007 Wu XS, Lee SH, Sheng J, Zhang Z, Zhao WD, Wang D, Jin Y, Charnay P, Ervasti JM, Wu LG
1008 (2016) Actin Is Crucial for All Kinetically Distinguishable Forms of Endocytosis at Synapses.
1009 *Neuron*
1010 Wu Y, O'Toole ET, Girard M, Ritter B, Messa M, Liu X, McPherson PS, Ferguson SM, De Camilli
1011 P (2014) A dynamin 1-, dynamin 3- and clathrin-independent pathway of synaptic vesicle
1012 recycling mediated by bulk endocytosis. *Elife* 3: e01621
1013 Xu Y, Moseley JB, Sagot I, Poy F, Pellman D, Goode BL, Eck MJ (2004) Crystal structures of a
1014 Formin Homology-2 domain reveal a tethered dimer architecture. *Cell* 116: 711-723
1015 Zhou L, McInnes J, Wierda K, Holt M, Herrmann AG, Jackson RJ, Wang YC, Swerts J, Beyens
1016 J, Miskiewicz K *et al* (2017) Tau association with synaptic vesicles causes presynaptic
1017 dysfunction. *Nat Commun* 8: 15295
1018
1019

1020 **FIGURES**

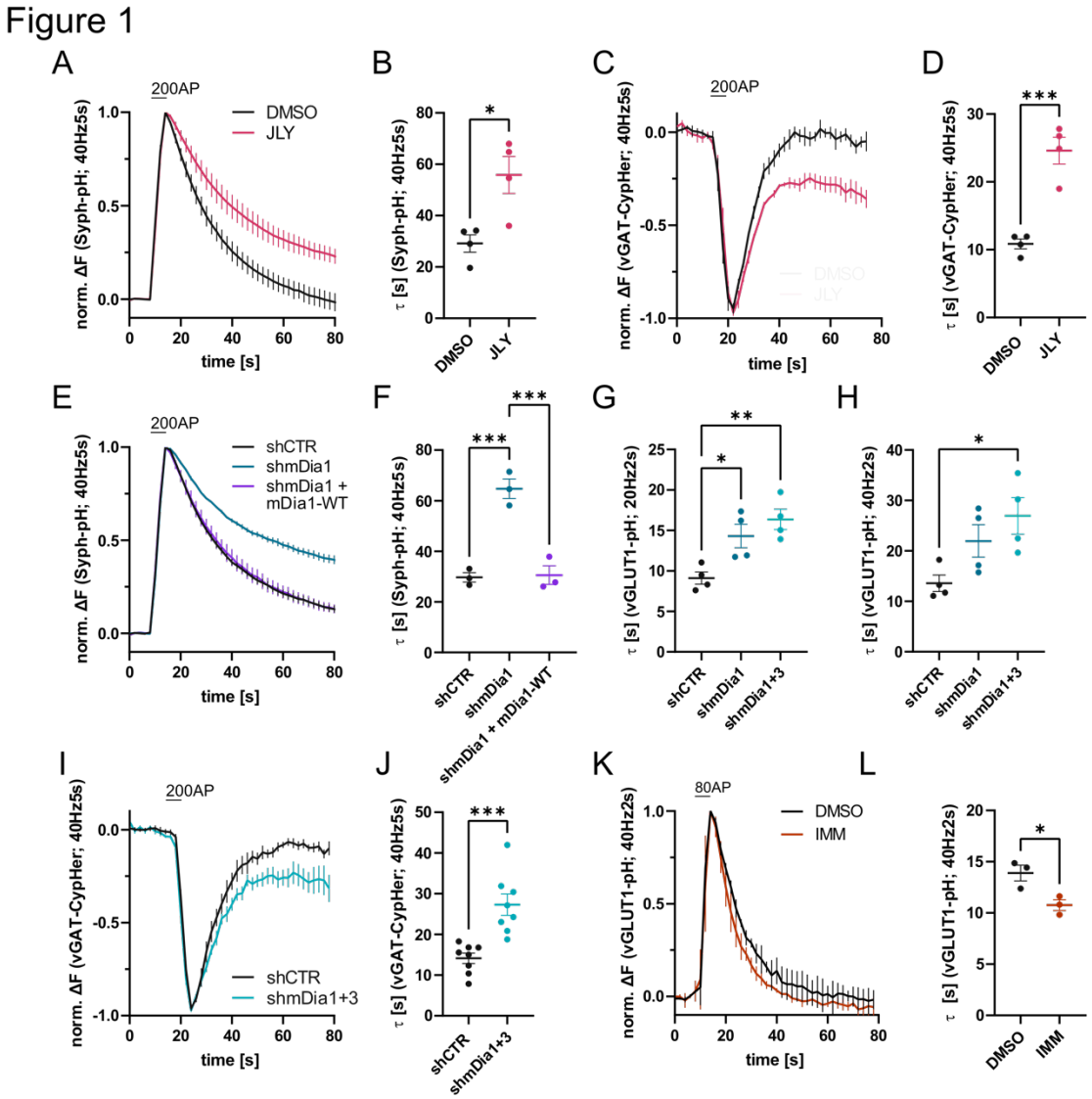

1021

1022 **Figure 1 | Actin dynamics and actin-nucleating mDia1/3 proteins facilitate SV endocytosis.**

1023 **(A)** Averaged normalized Synaptophysin-pHluorin (Syph-pH) fluorescence traces from

1024 transfected hippocampal neurons stimulated with 200 APs (40 Hz, 5s) at physiological temperature

1025 (37.5°C). Neurons were treated with 0.1% DMSO or JLY cocktail (containing 8 µM

1026 Jasplakinolide, 5 µM Latrunculin A and 10 µM Y-27632) as indicated. Data shown represent the

1027 mean ± SEM. N = 4 independent experiments from n_{DMSO} = 23 videos; n_{JLY} = 36 videos.

1028 **(B)** Endocytic decay constants (τ) of Synaptophysin-pHluorin traces in A: τ_{DMSO} = 29.1 ± 3.4 s;
1029 τ_{JLY} = 55.8 ± 7.2 s; $p < 0.05$, two-tailed student's t-test. Data shown represent mean ± SEM.
1030 **(C)** Averaged normalized bleach-corrected vGAT-CypHer fluorescence traces from hippocampal
1031 neurons treated with DMSO or JLY cocktail in response to 200 AP (40 Hz, 5s) stimulation. Data
1032 shown represent the mean ± SEM. N = 4 independent experiments from n_{DMSO} = 23 videos; n_{JLY}
1033 = 29 videos.
1034 **(D)** Endocytic decay constants of vGAT-CypHer traces in C: τ_{DMSO} = 10.9 ± 0.7 s, τ_{JLY} = 24.6 ±
1035 2.0 s; $p < 0.001$, two-tailed unpaired student's t-test. Data shown represent the mean ± SEM.
1036 **(E)** Averaged normalized Synaptophysin-pHluorin fluorescence traces from hippocampal neurons
1037 transfected with shRNA-encoding plasmids against no mammalian target (shCTR) or mDia1
1038 (shmDia1) in response to 200 AP (40 Hz, 5s) stimulation. Neurons were co-transfected with
1039 mDia1-mCherry (mDia1-WT) or mCherry alone (shCTR & shmDia1) to exclude artefacts from
1040 overexpression. Data shown represent the mean ± SEM. N = 3 independent experiments from
1041 n_{shCTR} = 28 videos, $n_{shmDia1}$ = 21 videos, $n_{shmDia1 + mDia1\text{-}WT}$ = 21 videos.
1042 **(F)** Endocytic decay constants of Synaptophysin-pHluorin traces in E: τ_{shCTR} = 29.7 ± 1.9 s;
1043 $\tau_{shmDia1}$ = 64.7 ± 3.9 s; $\tau_{shmDia1 + mDia1\text{-}WT}$ = 30.6 ± 3.7 s; $p_{shCTR\ vs\ shmDia1} < 0.001$, $p_{shmDia1\ vs\ shmDia1 +}$
1044 $_{mDia1\text{-}WT} < 0.001$, one-way ANOVA with Tukey's post-test. Data shown represent mean ± SEM.
1045 **(G)** Endocytic decay constants of averaged normalized vGLUT1-pHluorin fluorescence traces
1046 (Figure 1–Supplement 1I) from hippocampal neurons transduced with shCTR (τ_{shCTR} = 9.1 ± 0.8
1047 s), shmDia1 ($\tau_{shmDia1}$ = 14.3 ± 1.5 s) or shmDia1+3 ($\tau_{shmDia1+3}$ = 16.4 ± 1.3 s) in response to 40 AP
1048 (20 Hz, 2s) stimulation ($p_{shCTR\ vs\ shmDia1} < 0.05$, $p_{shCTR\ vs\ shmDia1+3} < 0.01$, one-way ANOVA with
1049 Tukey's post-test). Data shown represent mean ± SEM. N = 4 independent experiments from n_{shCTR}
1050 = 17 videos; $n_{shmDia1}$ = 19 videos; $n_{shmDia1+3}$ = 18 videos.

1051 **(H)** Endocytic decay constants of averaged normalized vGLUT1-pHluorin fluorescence traces
1052 (Figure 1–Supplement 1K) of neurons transduced with lentiviral vectors encoding shCTR (τ_{shCTR}
1053 = 13.6 ± 1.6 s), shmDia1 ($\tau_{shmDia1}$ = 22.0 ± 3.2 s) or shmDia1+3 ($\tau_{shmDia1+3}$ = 26.9 ± 3.6 s) in
1054 response to 80 AP (40 Hz, 2s) stimulation ($p_{shCTR\ vs\ shmDia1+3} < 0.05$, one-way ANOVA with
1055 Tukey's post-test). Data shown represent mean ± SEM. N = 4 independent experiments from n_{shCTR}
1056 = 12 videos, $n_{shmDia1}$ = 15 videos, $n_{shmDia1+3}$ = 18 videos.
1057 **(I)** Averaged normalized bleach-corrected vGAT-CypHer fluorescence traces from hippocampal
1058 neurons transduced with shCTR or shmDia1+3 in response to 200 AP (40 Hz, 5s) stimulation.
1059 Data shown represent the mean ± SEM. N = 8 independent experiments from n_{shCTR} = 37 videos,
1060 $n_{shmDia1+3}$ = 35 videos.
1061 **(J)** Endocytic decay constants of vGAT-CypHer traces in I: τ_{shCTR} = 14.1 ± 1.3 s; $\tau_{shmDia1+3}$ = 27.3
1062 ± 2.6 s; $p < 0.001$, two-tailed unpaired student's t-test. Data shown represent the mean ± SEM.
1063 **(K)** Averaged normalized vGLUT1-pHluorin fluorescence traces from transduced neurons in
1064 response to 80 AP (40 Hz, 2s) stimulation. Cells were treated with 0.1% DMSO or 10 μM mDia
1065 activator (IMM) in the imaging buffer. Data shown represent mean ± SEM. N = 3 independent
1066 experiments from n_{DMSO} = 18 videos; n_{IMM} = 16 videos.
1067 **(L)** Endocytic decay constants of vGLUT1-pHluorin traces in K: τ_{DMSO} = 14.9 ± 0.8 s; τ_{IMM}= 9.8
1068 ± 0.5 s; $p < 0.05$, two-tailed unpaired student's t-test. Data shown represent mean ± SEM.
1069

Figure 2

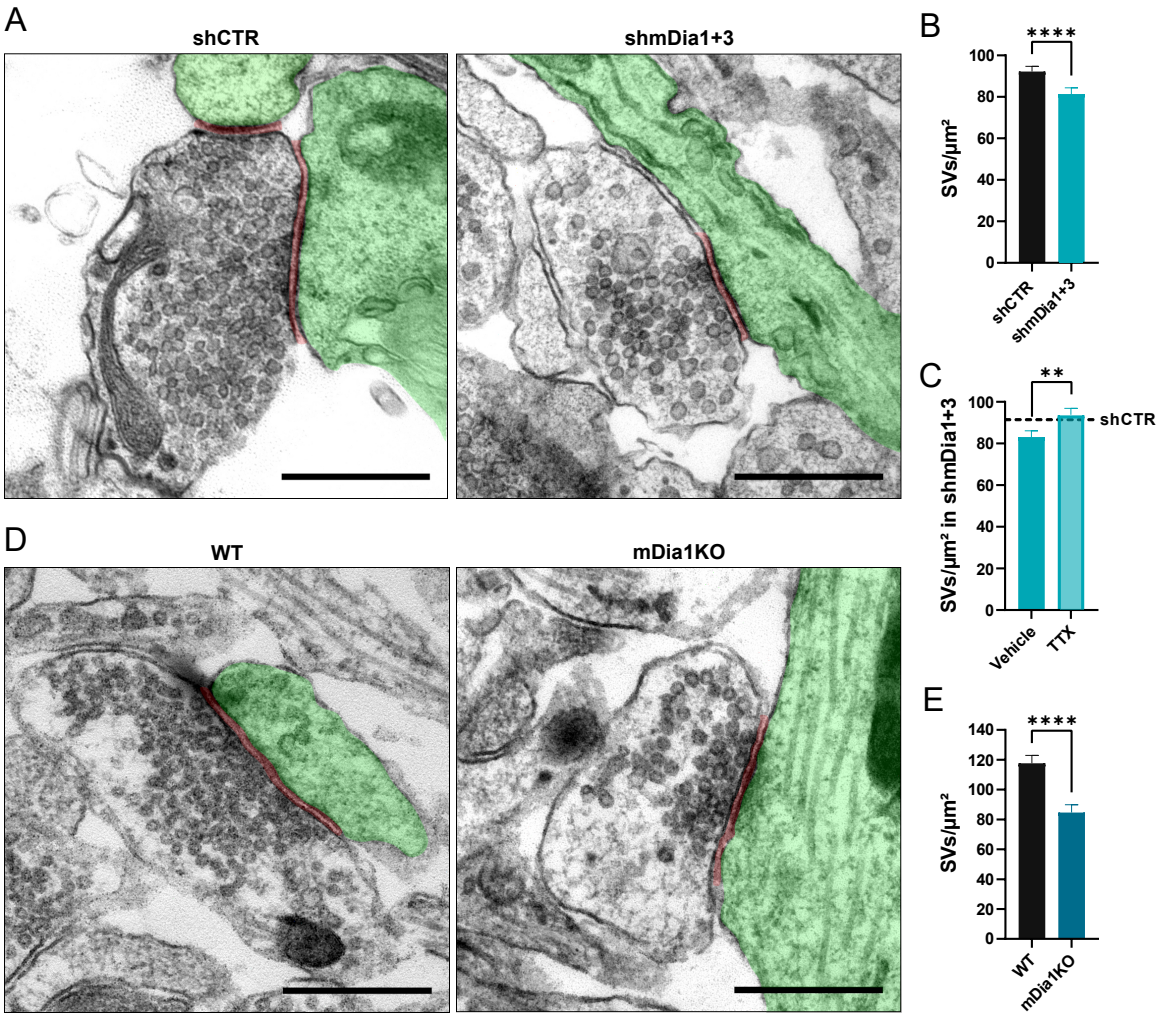

Figure 2 | Loss of mDia1/3 causes an activity-dependent reduction of the SV pool.

(A) Representative synaptic electron micrographs from hippocampal neurons transduced with lentiviruses encoding shCTR or shmDia1+3. Postsynapse and postsynaptic cleft are colored in green and maroon, respectively. Scale bar, 250 nm.

(B) Average number of SVs per μm^2 in boutons from shCTR (92.2 ± 2.5) and shmDia1+3 (81.4 ± 2.9; $p < 0.0001$, Mann-Whitney test) treated neurons. Data shown represent mean ± SEM. N = 3 independent experiments from n_{shCTR} = 326 synapses, $n_{shmDia1+3}$ = 321 synapses.

1078 **(C)** Average number of SVs per μm^2 in synaptic boutons from hippocampal neurons transduced
1079 with lentiviruses encoding shmDia1+3 and treated with 0.1 % Vehicle (10 µM NaOAc; 83.2 ±
1080 2.9) or 1 µM Tetrodotoxin (TTX; 93.8 ± 3.1; $p < 0.01$, Mann-Whitney test) for 36 h before
1081 chemical fixation. Data shown represent mean ± SEM from two independent experiments and
1082 $n_{Vehicle} = 225$ synapses, $n_{TTX} = 221$ synapses. Representative synaptic electron micrographs are
1083 shown in Figure 2–Supplement 1A. The dotted line represents the average SV numbers/ μm^2 in
1084 shCTR boutons treated with DMSO from the same experiments as a reference (Figure 2-
1085 Supplement 1A,B).
1086 **(D)** Representative electron micrographs of synapses in hippocampal neurons from WT or mDia1
1087 KO mice. Postsynapse and postsynaptic cleft are colored in green and maroon, respectively. Scale
1088 bar, 250nm.
1089 **(E)** Average number of SVs per μm^2 in WT (117.6 ± 5.3) and mDia1 KO (84.6 ± 5.2; $p < 0.0001$,
1090 Mann-Whitney test) boutons. Data shown represent the mean ± SEM from $n_{WT} = 103$, $n_{KO} = 96$
1091 synapses (N = 1).
1092
1093

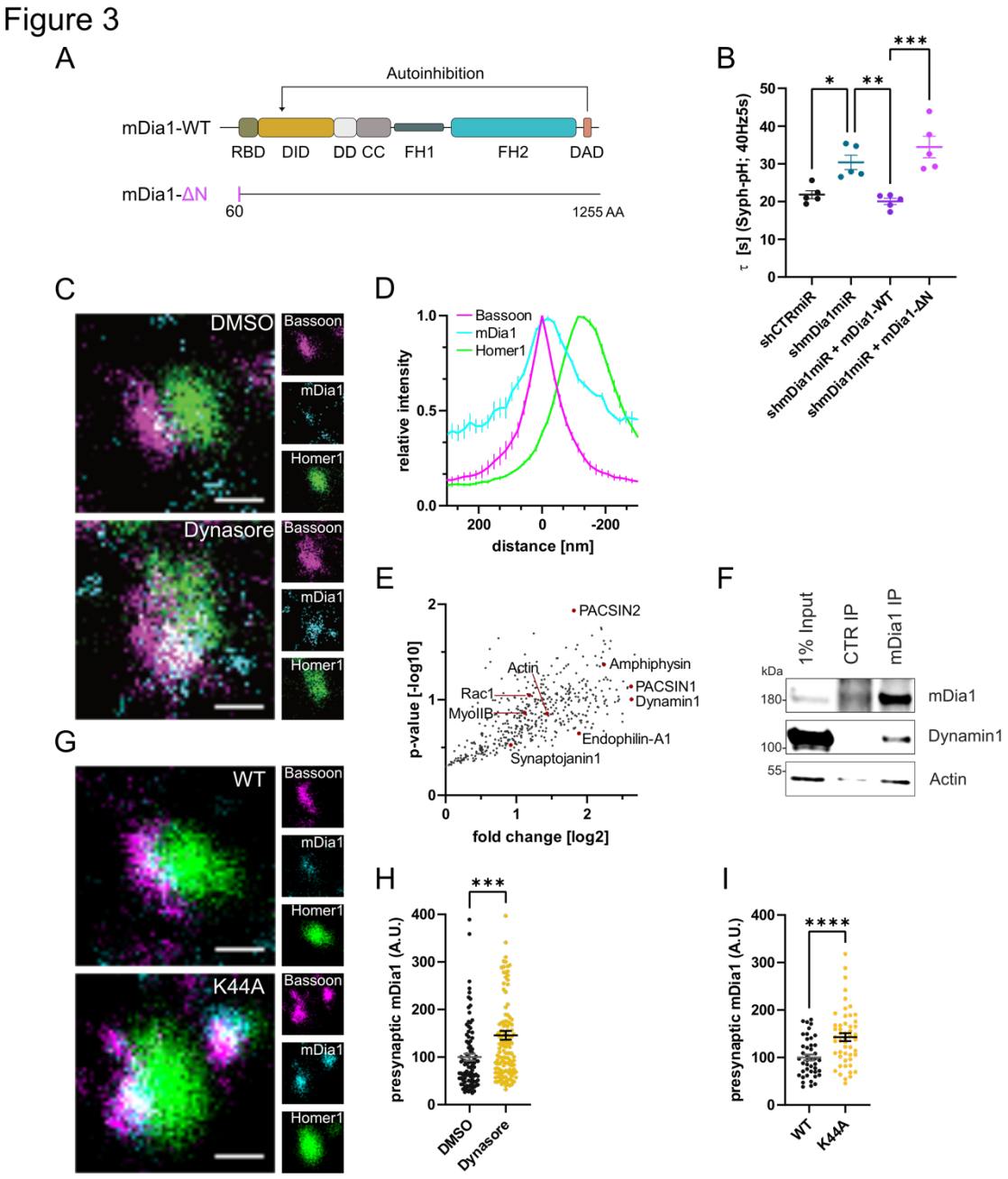

Figure 3 | mDia1 associates with endocytic proteins and localizes to presynaptic sites.

(A) Schematic representation of functional domains of mDia1. Rho-binding domain (RBD), Diaphanous inhibitory domain (DID), Dimerization domain (DD), Coiled coil domain (CC), Formin homology domain 1 (FH1), Formin homology domain 2 (FH2), Diaphanous autoinhibitory

1099 domain (DAD). The unstructured N-terminus (first 60 amino acids) contains three basic stretches
1100 and was truncated in the ΔN mutant.
1101 **(B)** Endocytic decay constants of Synaptophysin-pHluorin traces (Figure 3-Supplement 1C) from
1102 hippocampal neurons transfected with shRNAmiR against no mammalian target (shCTRmiR) or
1103 mDia1 (shmDia1miR) in response to 200 AP (40 Hz, 5s) stimulation. For rescue experiments,
1104 neurons were co-transfected with plasmids encoding mDia1-WT-mCherry ($\tau_{shmDia1miR + mDia1\text{-}WT}$ =
1105 20.0 ± 0.8 s), mDia1-ΔN-mCherry ($\tau_{shmDia1miR + mDia1\text{-}\Delta N}$ = 34.5 ± 2.9 s) or mCherry alone ($\tau_{shCTRmiR}$
1106 = 21.8 ± 1.1 s, $\tau_{shmDia1miR}$ = 30.4 ± 1.9 s) to exclude artefacts from overexpression ($p_{shCTRmiR\ vs\ shmDia1miR} < 0.05$; $p_{shmDia1miR\ vs\ shmDia1miR + mDia1\text{-}WT} < 0.01$; $p_{shmDia1miR + mDia1\text{-}WT\ vs\ shmDia1miR + mDia1\text{-}\Delta N}$
1108 < 0.01, one-way ANOVA with Tukey's post-test). Data shown represent mean ± SEM. N = 5
1109 independent experiments from $n_{shCTRmiR}$ = 41 videos, $n_{shmDia1miR}$ = 51 videos, $n_{shmDia1miR + mDia1\text{-}WT}$
1110 = 35 videos, $n_{shmDia1miR + mDia1\text{-}\Delta N}$ = 37 videos.
1111 **(C)** Representative three-channel time-gated STED images of synapses from hippocampal cultures
1112 treated with 0.1% DMSO or 80 µM Dynasore for 10 min before fixation and immunostained for
1113 Bassoon (presynaptic marker, magenta), mDia1 (cyan) and Homer1 (postsynaptic marker, green).
1114 Scale bar, 250 nm.
1115 **(D)** Averaged normalized line profiles for synaptic distribution of mDia1 and Homer1 relative to
1116 Bassoon (Maximum set to 0 nm). Data represent mean ± SEM. N = 3 independent experiments
1117 from n = 235 synapses.
1118 **(E)** Volcano plot of proteins associating with synaptic mDia1 analyzed by label-free proteomics
1119 of anti-mDia1 versus control (CTR) immunoprecipitates from detergent-extracted mouse
1120 synaptosomes (P2' fraction). The logarithmic ratios of protein intensities are plotted against
1121 negative logarithmic p-values derived from two-tailed student's t-test. N = 3 independent
1122 experiments. Each dot represents one protein/gene. Selected cytoskeletal hits include: Actin,

1123 Myosin IIB (MyoIIB) and Rac1. Selected endocytic hits include Amphiphysin ($p < 0.05$),
1124 Dynamin1, Endophilin-A1, PACSIN1, PACSIN2 ($p < 0.05$) and Synaptojanin1.
1125 **(F)** Endogenous immunoprecipitation of mDia1 from detergent-extracted mouse synaptosomes
1126 (P2' fraction) using mDia1-specific antibodies. Immunoprecipitates were analyzed by
1127 immunoblotting for mDia1, Dynamin1 and β-Actin.
1128 **(G)** Representative three-channel time-gated STED images of synapses from hippocampal cultures
1129 transduced with wildtype Dynamin1 (WT) or GTPase-deficient Dynamin1 (K44A) in response to
1130 200 AP (40 Hz, 5s) stimulation. Cells were immunostained for Bassoon (magenta), mDia1 (cyan)
1131 and Homer1 (green). Scale bar, 250 nm.
1132 **(H)** Presynaptic mDia1 levels in synapses treated with 0.1% DMSO (100 ± 7.3) or 80 µM
1133 Dynasore (145.8 ± 9.3; $p = 0.0001$; one sample Wilcoxon test) for 10 min in response to 200 AP
1134 (40 Hz, 5s) stimulation. Absolute line profiles of mDia1 overlapping with Bassoon (presynapse)
1135 distribution were integrated. Data shown are normalized to DMSO (set to 100) and expressed as
1136 mean ± SEM. N = 3 independent experiments from $n_{DMSO} = 92$ synapses, $n_{Dynasore} = 135$ synapses.
1137 **(I)** Presynaptic mDia1 levels in synapses from hippocampal neurons transduced with wildtype
1138 Dynamin1 (WT; 100 ± 6.2) or GTPase-deficient Dynamin1 (K44A; 142.9 ± 8.3, $p < 0.0001$, one
1139 sample Wilcoxon test) in response to 200 AP (40 Hz, 5s) stimulation. Line profiles of mDia1
1140 overlapping with Bassoon distribution were integrated. Data shown are normalized to Dynamin1-
1141 WT (set to 100) and expressed as mean ± SEM. N = 2 independent experiments from $n_{WT} = 43$
1142 synapses, $n_{K44A} = 51$ synapses.
1143

Figure 4

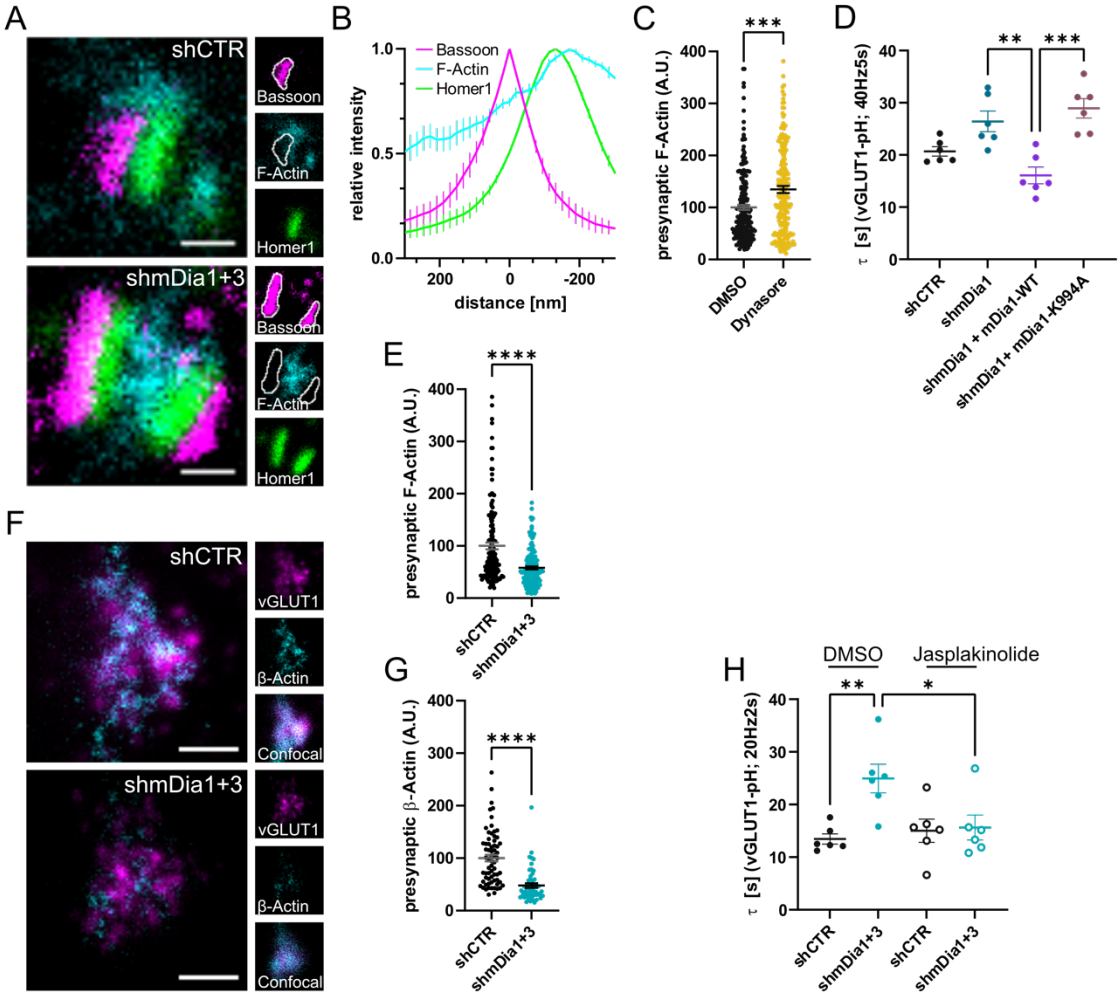

Figure 4 | mDia facilitates SV endocytosis by regulating presynaptic F-actin.

(A) Representative three-channel time-gated STED images of synapses from hippocampal cultures transduced with shCTR or shmDia1+3, fixed and immunostained for Bassoon (presynaptic marker, magenta), F-Actin (cyan) and Homer1 (postsynaptic marker, green). Scale bar, 250 nm.

(B) Averaged normalized line profiles for synaptic distribution of F-Actin and Homer1 relative to Bassoon (Maximum set to 0 nm). Data are expressed as mean ± SEM. N = 4 independent experiments from n = 154 synapses.

(C) Presynaptic F-Actin levels in synapses treated with 0.1% DMSO (100 ± 4.8) or 80 µM Dynasore (134.7 ± 6.8; p = 0.001, one sample Wilcoxon test) for 10 min before fixation

1154 (Represenative images in Figure 4–Supplement 1A). Cells were immunostained for Bassoon
1155 (magenta), F-Actin (cyan), and Homer1 (green). Absolute line profiles of F-Actin overlapping
1156 with Bassoon (presynapse) distribution were integrated. Data shown are normalized to DMSO (set
1157 to 100) and expressed as mean ± SEM. N = 3 independent experiments from n_{DMSO} = 207 synapses,
1158 $n_{Dynasore}$ = 211 synapses.

1159 **(D)** Endocytic decay constants of vGLUT1-pHluorin traces from hippocampal neurons transduced
1160 with lentiviral particles encoding shCTR (τ_{shCTR} = 20.7 ± 0.9 s) or shmDia1 ($\tau_{shmDia1}$ = 26.4 ± 2.0
1161 s) in response to 200 AP (40 Hz, 5s) stimulation. For rescue experiments, neurons were co-
1162 transduced with lentiviruses encoding mDia1-WT-SNAP ($\tau_{shmDia1 + mDia1\text{-}WT}$ = 16.1 ± 1.9 s) or
1163 mDia1-K994A-SNAP ($\tau_{shmDia1 + mDia1\text{-}K994A}$ = 29.0 ± 1.9 s) ($p_{shmDia1 \text{ vs } shmDia1 + mDia1\text{-}WT}$ < 0.01;
1164 $p_{shmDia1 + mDia1\text{-}WT \text{ vs } shmDia1 + mDia1\text{-}K994A}$ < 0.001, one-way ANOVA with Tukey's post-test). Data are
1165 expressed as mean ± SEM. N = 6 independent experiments from n_{shCTR} = 21 videos; $n_{shmDia1}$ =
1166 21 videos, $n_{shmDia1 + mDia1\text{-}WT}$ = 16 videos, $n_{shmDia1 + mDia1\text{-}K994A}$ = 19 videos.

1167 **(E)** Presynaptic F-Actin levels in synapses from hippocampal cultures transduced with shCTR
1168 (100 ± 6.4) or shmDia1+3 (58.1 ± 2.9; p < 0.001, one sample Wilcoxon test). Line profiles of F-
1169 Actin overlapping with Bassoon (presynapse) distribution were integrated. Data shown are
1170 normalized to shCTR (set to 100) and expressed as mean ± SEM. N = 4 independent experiments
1171 from n_{shCTR} = 155 synapses, $n_{shmDia1+3}$ = 158 synapses.

1172 **(F)** Representative confocal and two-channel time-gated STED images of endogenous β-Actin
1173 (cyan) in vGLUT1 (magenta) positive boutons from hippocampal neurons transduced with
1174 lentiviruses encoding shCTR or shmDia1+3. Scale bar, 250 nm.

1175 **(G)** Analysis of presynaptic endogenous β-Actin levels in vGLUT1 positive boutons from shCTR
1176 (100 ± 6.3) and shmDia1+3 (47.7 ± 4.3; p < 0.0001 one sample Wilcoxon test) transduced neurons.
1177 β-Actin STED mean intensity was measured using confocal vGLUT1 signal as a mask. Data

1178 shown are normalized to shCTR (set to 100) and expressed as mean ± SEM from two independent
1179 experiments and n_{shCTR} = 67 synapses, $n_{shmDia1+3}$ = 53 synapses.
1180 **(H)** Endocytic decay constants of vGLUT1-pHluorin traces (Figure 4–Supplement 1H) for
1181 neurons transduced with shCTR or shmDia1+3 in response to 40 AP (20 Hz, 2s) stimulation.
1182 Neurons were pre-incubated with 0.1 % DMSO or 1 μM Jasplakinolide (Jasp) for 30 min in the
1183 media before imaging ($\tau_{shCTR + DMSO}$ = 13.4 ± 1.0 s, $\tau_{shCTR + Jasp}$ = 15.0 ± 2.2 s, $\tau_{shmDia1+3 + DMSO}$ =
1184 25.0 ± 2.7 s, $\tau_{shmDia1+3 + Jasp}$ = 15.6 ± 2.4 s; $p_{shCTR\ vs\ shmDia1+3} < 0.01$; $p_{shmDia1+3 + DMSO\ vs\ shmDia1+3 + Jasp}$
1185 < 0.05, one-way ANOVA with Tukey's post-test). Data are expressed as mean ± SEM. N = 6
1186 independent experiments from $n_{shCTR + DMSO}$ = 32 videos, $n_{shmDia1+3 + DMSO}$ = 35 videos, $n_{shCTR + Jasp}$
1187 = 33 videos; $n_{shmDia1+3 + Jasp}$ = 34 videos).
1188
1189

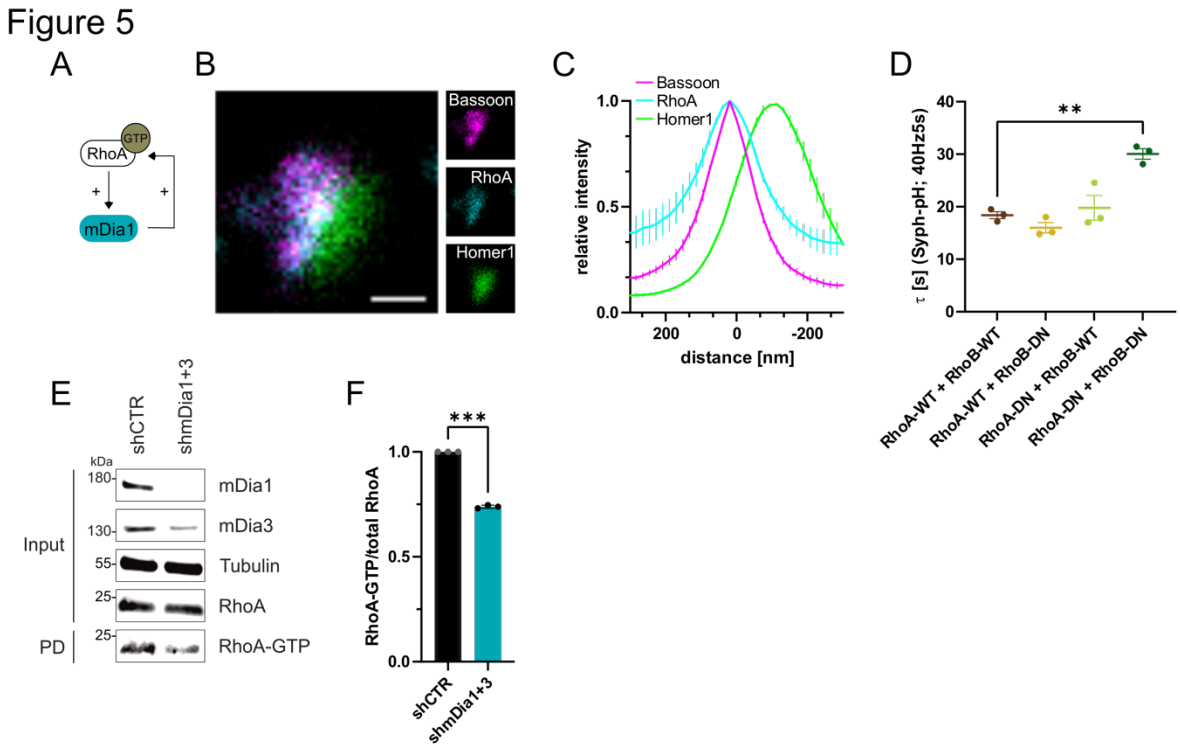

Figure 5 | RhoA/B facilitate presynaptic endocytosis and are regulated by mDia1/3.

(A) Schematic representation of activation of mDia1 by RhoA-GTP and positive feedback loop of mDia1 on RhoA-GTP levels through GEF stimulation.

(B) Representative three-channel time-gated STED image of a synapses from hippocampal cultures, fixed and immunostained for Bassoon (magenta), RhoA (cyan) and Homer1 (green). Scale bar, 250 nm.

(C) Averaged normalized line profiles for synaptic distribution of RhoA and Homer1 relative to Bassoon (Maximum set to 0 nm). Data are expressed as mean ± SEM. N = 5 independent experiments from n = 230 synapses.

(D) Endocytic decay constants of averaged normalized Synaptophysin-pHluorin fluorescence traces (Figure 5–Supplement 1A) in response to 200 AP (40 Hz, 5s) stimulation. Neurons were transfected with the annotated combinations of plasmids encoding wild-type (WT) or dominant-negative (DN, T19N mutation) RhoA and RhoB ($\tau_{RhoA\text{-}WT + RhoB\text{-}WT}$ = 18.4 ± 0.7 s, $\tau_{RhoA\text{-}WT + RhoB\text{-}}$

$_{DN}$ = 16.0 ± 1.0 s, $\tau_{RhoA\text{-}DN + RhoB\text{-}WT}$ = 19.8 ± 2.4 s, $\tau_{RhoA\text{-}DN + RhoB\text{-}DN}$ = 30.1 ± 1.0 s; $p_{RhoA\text{-}WT + RhoB\text{-}WT \text{ vs } RhoA\text{-}DN + RhoB\text{-}DN}$ < 0.01, one-way ANOVA with Tukey's post-test). Data shown represent mean ± SEM. N = 3 independent experiments from $n_{RhoA\text{-}WT + RhoB\text{-}WT}$ = 21 videos, $n_{RhoA\text{-}DN + RhoB\text{-}WT}$ = 31 videos, $n_{RhoA\text{-}WT + RhoB\text{-}DN}$ = 23 videos, $n_{RhoA\text{-}DN + RhoB\text{-}DN}$ = 22 videos.

(E) Analysis of RhoA activity by RhoA-GTP pulldown (PD) from whole-cell lysates (input) of mouse hippocampal neurons expressing shCTR or shmDia1+3 using immobilized Rhotekin as a bait. Samples were analyzed by immunoblotting for mDia1, mDia3, RhoA and Tubulin using specific antibodies. Input, 10% of material used for the pulldown. Contrast of pulldown and input blots was seperatly adjusted for visualisation purposes.

(F) Densitometric quantification of RhoA-GTP normalized to total RhoA levels (input) in lysates from neurons transduced with shCTR or shmDia1+3 (0.7 ± 0.0, $p < 0.001$, one sample t-test) from immunoblots exemplified in E. Values for shCTR were set to 1. Data are expressed as mean ± SEM from N = 3 independent experiments.

Figure 6

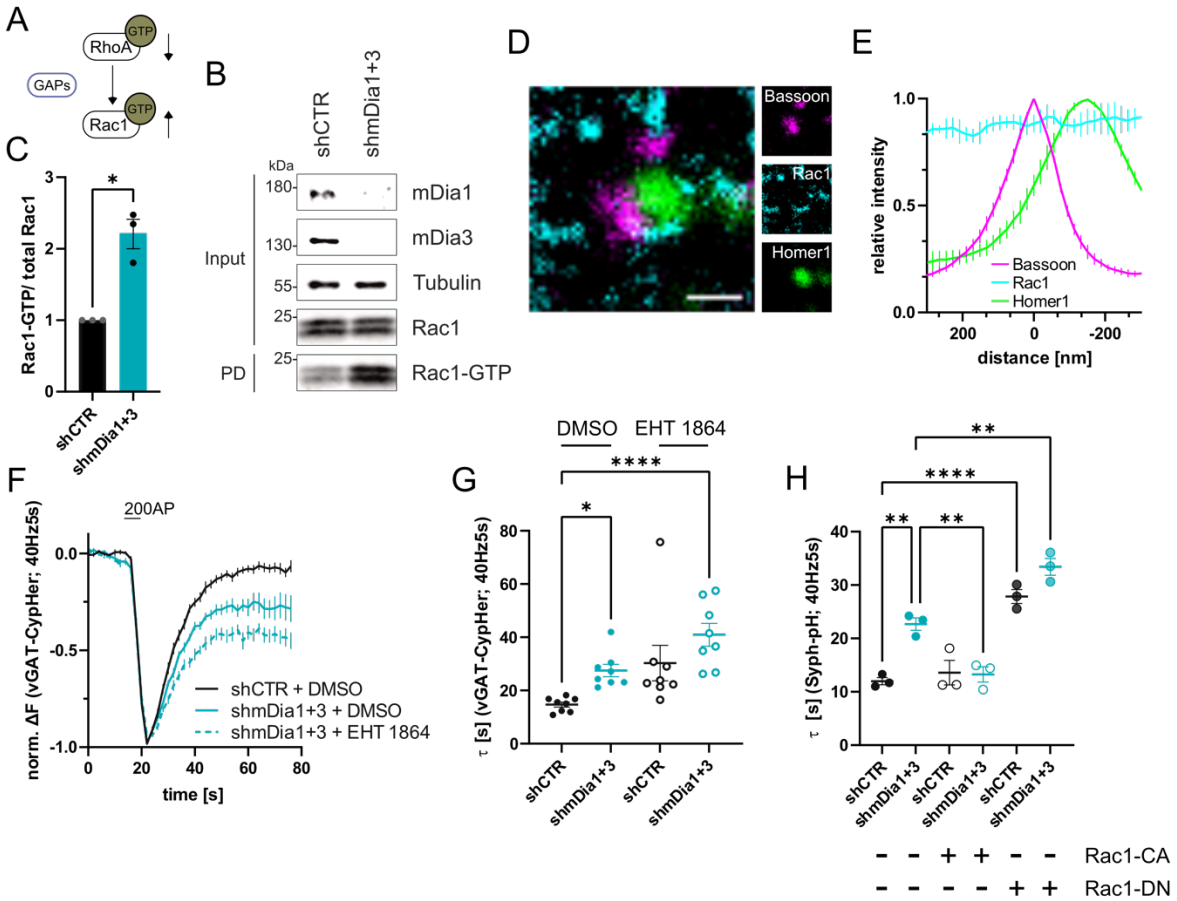

Figure 6 | mDia1/3-Rho and Rac1 signaling facilitates presynaptic endocytosis.

(A) Schematic of the interplay between RhoA and Rac1 signaling via GTPase activating proteins (GAPs) common for RhoA and Rac1.

(B) Analysis of Rac1 activity by Rac1-GTP pulldown (PD) from whole-cell lysates (input) of mouse hippocampal neurons expressing shCTR or shmDia1+3 utilizing immobilized PAK as a bait. Samples were analyzed by immunoblotting for mDia1, mDia3, Rac1 and Tubulin using specific antibodies. Input, 10% of material used for the pulldown. Contrast of pulldown and input blots was seperatly adjusted for visualisation purposes.

(C) Densitometric quantification of Rac1-GTP normalized to total Rac1 levels (input) in lysates from neurons transduced with shCTR or shmDia1+3 (2.2 ± 0.2; $p < 0.05$, one sample t-test) from

1229 immunoblots exemplified in (B). Values for shCTR were set to 1. Data are expressed as mean ±
1230 SEM from N = 3 independent experiments.
1231 **(D)** Representative three-channel time-gated STED image of a synapses from hippocampal
1232 cultures, fixed and immunostained for Bassoon (magenta), Rac1 (cyan) and Homer1 (green). Scale
1233 bar, 250 nm.
1234 **(E)** Averaged normalized line profiles for synaptic distribution of Rac1 and Homer1 relative to
1235 Bassoon (Maximum set to 0 nm). Data represent mean ± SEM. N = 3 independent experiments
1236 from n = 79 synapses.
1237 **(F)** Averaged normalized vGAT-CypHer fluorescence traces for neurons transduced with shCTR
1238 or shmDia1+3 in response to 200 AP (40 Hz, 5 s) stimulation. Cells were acutely treated with
1239 0.1 % DMSO or 10 µM Rac1 Inhibitor (EHT 1864) in the imaging buffer. Data shown represent
1240 the mean ± SEM. N = 8 independent experiments from $n_{shCTR + DMSO}$ = 46 videos, $n_{shmDia1+3 + DMSO}$
1241 = 45 videos, $n_{shCTR + EHT\ 1864}$ = 42 videos, $n_{shmDia1+3 + EHT\ 1864}$ = 43 videos.
1242 **(G)** Endocytic decay constants of vGAT-CypHer traces in F: $\tau_{shCTR + DMSO}$ = 14.7 ± 0.9 s, $\tau_{shmDia1+3}$
1243 $_{+ DMSO}$ = 27.5 ± 2.3 s, $\tau_{shCTR + EHT\ 1864}$ = 30.3 ± 6.7 s, $\tau_{shmDia1+3 + EHT\ 1864}$ = 41.0 ± 4.3 s; $p_{shCTR + DMSO}$
1244 $_{vs\ shmDia1+3 + DMSO}$ < 0.05, $p_{shCTR + DMSO\ vs\ shmDia1+3 + EHT\ 1864}$ < 0.0001, Kruskal-Wallis test with Dunn's
1245 post-test. Data represent mean ± SEM.
1246 **(H)** Endocytic decay constants of Synaptophysin-pHluorin traces (Figure 6–Supplement 1E) of
1247 neurons transduced with shCTR (τ_{shCTR} = 12.0 ± 0.7 s) or shmDia1+3 ($\tau_{shmDia1+3}$ = 22.7 ± 2.0 s) and
1248 transfected with constitutively active Rac1 (Rac1-CA; Q61L variant; $\tau_{shCTR + Rac1\text{-}CA}$ = 13.6 ± 1.2
1249 s, $\tau_{shmDia1+3 + Rac1\text{-}CA}$ = 13.3 ± 1.4 s) or dominant negative Rac1 (Rac1-DN; T17N variant; $\tau_{shCTR +}$
1250 $_{Rac1\text{-}DN}$ = 27.8 ± 1.3 s, $\tau_{shmDia1+3 + Rac1\text{-}DN}$= 33.4 ± 1.6 s) in response to 200 AP (40 Hz, 5s) stimulation
1251 ($p_{shCTR\ vs\ shmDia1+3}$ < 0.01; $p_{shCTR\ vs\ shCTR + Rac1\text{-}DN}$ < 0.0001, $p_{shCTR\ vs\ shmDia1+3 + Rac1\text{-}DN}$ < 0.01, $p_{shmDia1+3}$
1252 $_{vs\ shmDia1+3 + Rac1\text{-}DN}$ < 0.01, one-way ANOVA with Tukey's post-test). Data are expressed as mean

1253 ± SEM. N = 3 independent experiments from n_{shCTR} = 12 videos, $n_{shmDia1+3}$ = 23 videos; $n_{shCTR + Rac1\text{-}CA}$ = 10 videos, $n_{shmDia1+3 + Rac1\text{-}CA}$ = 14 videos, $n_{shCTR + Rac1\text{-}DN}$ = 9 videos; $n_{shmDia1+3 + Rac1\text{-}DN}$ = 13 videos.

1256

1257

Figure 7

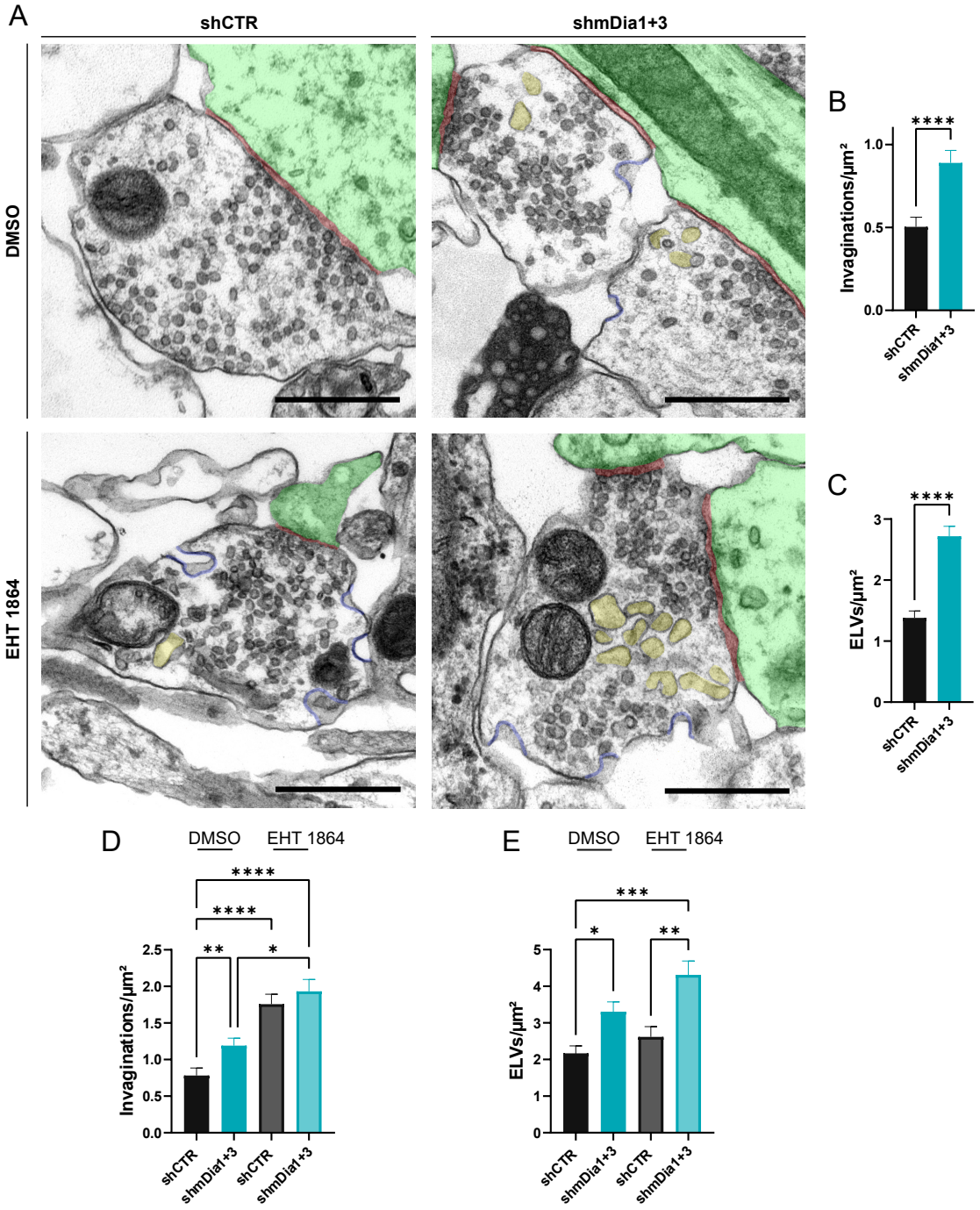

1258

1259 **Figure 7 | Defects in presynaptic ultrastructure induced by interference with mDia1/3-Rho**

1260 **and Rac1 signaling.**

1261 **(A)** Representative synaptic electron micrographs from hippocampal neurons transduced with
1262 lentiviruses encoding shCTR or shmDia1+3 and treated with 0.1 % DMSO or 10 µM Rac1
1263 Inhibitor (EHT 1864) for 2 h before fixation. Invaginations and ELVs are colored in blue and
1264 yellow, while postsynapse and synaptic cleft are colored in green and maroon, respectively. Scale
1265 bar, 250 nm.
1266 **(B)** Average number of invaginations per μm^2 in shCTR (0.5 ± 0.1) and shmDia1+3 (0.9 ± 0.1; p
1267 < 0.0001, Mann-Whitney test) boutons. Data represent mean ± SEM. N = 3 independent
1268 experiments from $n_{shCTR} = 326$ synapses, $n_{shmDia1+3} = 323$ synapses.
1269 **(C)** Average number of ELVs per μm^2 in shCTR (1.4 ± 0.1) and shmDia1+3 (2.7 ± 0.2; $p < 0.0001$,
1270 Mann-Whitney test) boutons. Data represent mean ± SEM. N = 3 independent experiments from
1271 $n_{shCTR} = 326$ synapses, $n_{shmDia1+3} = 323$ synapses.
1272 **(D)** Average number of invaginations per μm^2 in shCTR and shmDia1+3 boutons treated with
1273 0.1 % DMSO (0.8 ± 0.1 for shCTR; 1.2 ± 0.1 for shmDia1+3, $p_{shCTR + DMSO \text{ vs } shmDia1+3 + DMSO} <$
1274 0.01) or 10 µM EHT 1864 (1.8 ± 0.1 for shCTR, $p_{shCTR + DMSO \text{ vs } shCTR + EHT\ 1864} < 0.0001$; 1.9 ± 0.2
1275 for shmDia1+3, $p_{shCTR + DMSO \text{ vs } shmDia1+3 + EHT\ 1864} < 0.0001$, $p_{shmDia1+3 + DMSO \text{ vs } shmDia1+3 + EHT\ 1864} <$
1276 0.05, Kruskal-Wallis test with Dunn's post-test) for 2 h before fixation. Data represent mean ±
1277 SEM from $n_{shCTR + DMSO} = 144$ synapses, $n_{shmDia1+3 + DMSO} = 143$ synapses, $n_{shCTR + EHT\ 1864} = 136$
1278 synapses, $n_{shmDia1+3 + EHT\ 1864} = 153$ synapses.
1279 **(E)** Average number of ELVs per μm^2 in shCTR and shmDia1+3 boutons treated with 0.1 %
1280 DMSO (2.2 ± 0.2 for shCTR; 3.3 ± 0.3 for shmDia1+3, $p_{shCTR + DMSO \text{ vs } shmDia1+3 + DMSO} < 0.05$) or
1281 10 µM EHT 1864 (2.6 ± 0.3 for shCTR; 4.3 ± 0.4 for shmDia1+3, $p_{shCTR + DMSO \text{ vs } shmDia1+3 + EHT\ 1864}$
1282 < 0.001, $p_{shCTR + EHT\ 1864 \text{ vs } shmDia1+3 + EHT\ 1864} < 0.01$, Kruskal-Wallis test with Dunn's post-test) for
1283 2 h before fixation. Data represent mean ± SEM from $n_{shCTR + DMSO} = 144$ synapses, $n_{shmDia1+3 +}$
1284 $_{DMSO} = 143$ synapses, $n_{shCTR + EHT\ 1864} = 136$ synapses, $n_{shmDia1+3 + EHT\ 1864} = 153$ synapses.

1288 **LEGENDS for SUPPLEMENTS**

1289 **List of supplemental figures**

1290 **Figure 1–figure supplement 1 | Role of formins and mDia1/3 in SV endocytosis.**

1291 **Figure 2–figure supplement 1 | SV depletion in mDia1/3-depleted neurons is activity**
1292 **dependent.**

1293 **Figure 3–figure supplement 1 | mDia1 binds membranes and localizes to presynaptic**
1294 **endocytic sites.**

1295 **Figure 4–figure supplement 1| mDia1 regulates presynaptic actin and SV endocytosis.**

1296 **Figure 5–figure supplement 1 | RhoA/B regulate SV endocytosis.**

1297 **Figure 6–figure supplement 1 | Cooperative action of mDia1/3 and Rac1 pathways in**
1298 **presynaptic endocytosis.**

1299 **Figure 7–figure supplement 1 | mDia1/3 and Rac1 cooperatively regulate the SV cycle and**
1300 **presynaptic ultrastructure.**

1301

1302 **Supporting Table 1 – Oligonucleotides used in this study**

1303 **Source Data Table**

1304 **Raw uncropped immunoblot images (merged PDF)**

1305

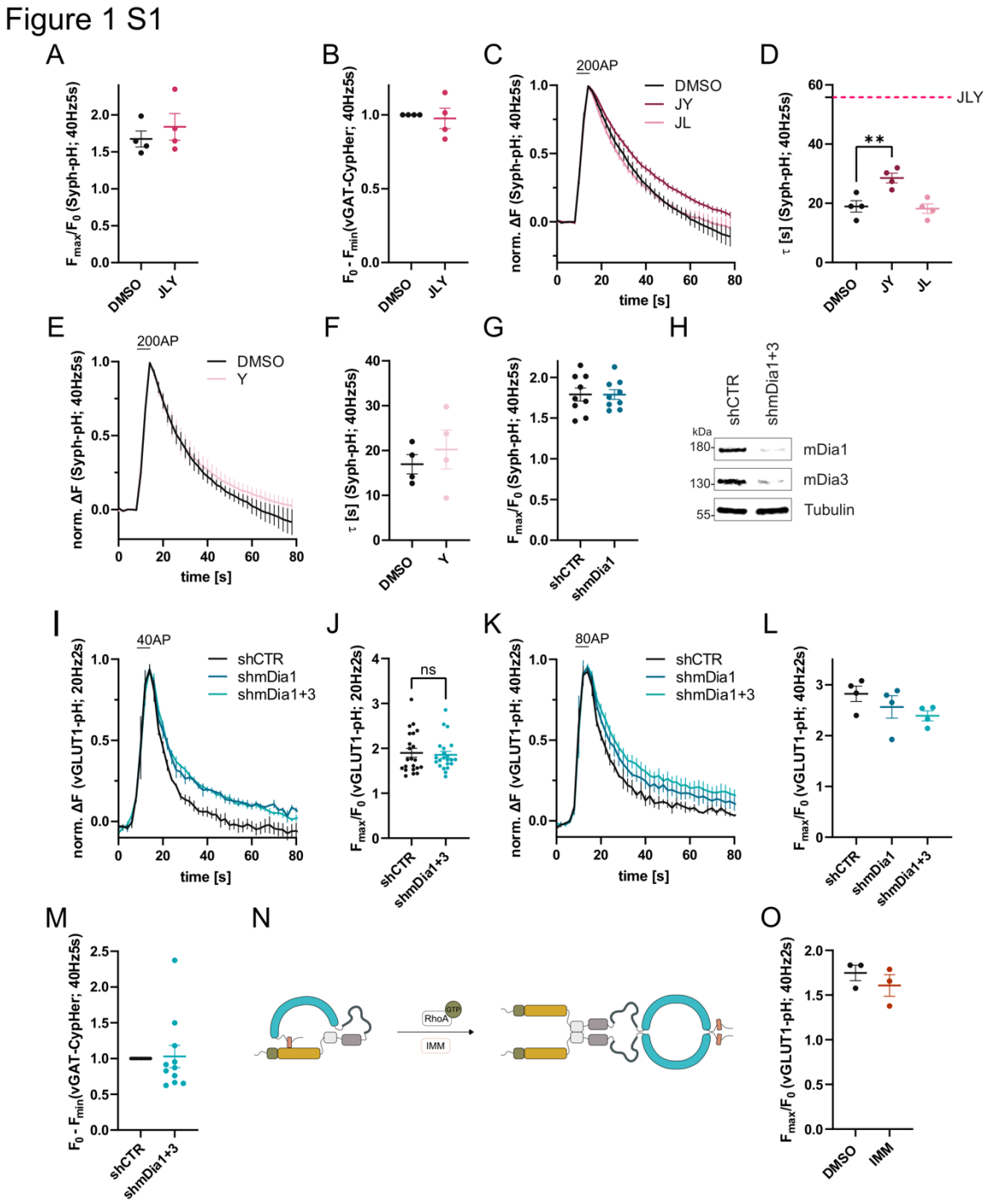

1306

1307 **Figure 1-Supplement 1 | Role of formins and mDia1/3 in SV endocytosis.**

1308 **(A)** Maxima of background-corrected Syph-pHluorin fluorescence traces (surface normalized) for
1309 neurons treated with 0.1 % DMSO (1.7 ± 0.1) or JLY cocktail (1.8 ± 0.2) in response to 200 AP
1310 stimulation (40 Hz, 5 s). Data represent mean ± SEM. N = 4 independent experiments from n_{DMSO}
1311 = 23 videos; n_{JLY} = 36 videos.
1312 **(B)** Minima of background-corrected vGAT-CypHer fluorescence traces (surface normalization)
1313 for neurons treated with 0.1 % DMSO or JLY cocktail (1.0 ± 0.1) in response to 200 AP stimulation
1314 (40 Hz, 5 s). Data represent mean ± SEM. Values for DMSO were set to 1. N = 4 independent
1315 experiments from n_{DMSO} = 23 videos; n_{JLY} = 29 videos.
1316 **(C)** Averaged normalized Syph-pH fluorescence traces from transfected hippocampal neurons
1317 treated with 0.1% DMSO, JY or JL combinations (containing 8 µM Jasplakinolide, 5 µM
1318 Latrunculin A and 10 µM Y-27632) stimulated with 200 APs (40 Hz, 5s). Data shown represent
1319 the mean ± SEM. N = 4 independent experiments from n_{DMSO} = 24 videos; n_{JY} = 19 videos; n_{JL} =
1320 21 videos.
1321 **(D)** Endocytic decay constants of Syph-pHluorin traces in C: τ_{DMSO} = 19.0 ± 1.9 s; τ_{JY} = 28.5 ± 1.6
1322 s; τ_{JL} = 18.2 ± 1.6 s; $p_{DMSO\ vs\ JY} < 0.01$, one-way ANOVA with Tukey's post-test. Data shown
1323 represent mean ± SEM.
1324 **(E)** Averaged normalized Syph-pH fluorescence traces from transfected hippocampal neurons
1325 treated with 0.1% DMSO or 10 µM Y-27632 following 200 AP (40 Hz, 5s) stimulation. Data
1326 shown represent the mean ± SEM. N = 4 independent experiments from n_{DMSO} = 25 videos; n_Y =
1327 18 videos.
1328 **(F)** Endocytic decay constants of Syph-pHluorin traces in C: τ_{DMSO} = 17.0 ± 2.2 s; τ_Y = 20.2 ± 4.3
1329 s. Data shown represent mean ± SEM.
1330 **(G)** Maxima of background-corrected Syph-pHluorin fluorescence traces (surface normalized) for
1331 neurons transfected with shCTR (1.8 ± 0.1) or shmDia1 (1.8 ± 0.1) in response to 200 AP

1332 stimulation (40 Hz, 5 s). Data represent mean ± SEM. N = 9 independent experiments from n_{shCTR}
1333 = 49 videos; $n_{shmDia1}$ = 42 videos.
1334 **(H)** Analysis of knockdown efficiency of lentiviral particles carrying shRNA against no
1335 mammalian target (shCTR) or mDia1 and mDia3 (shmDia1+3) in mouse hippocampal cultures
1336 harvested 12 days after transduction. Protein abundance of mDia1, mDia3 and Tubulin were
1337 immunoblotted with specific antibodies.
1338 **(I)** Averaged normalized vGLUT1-pHluorin fluorescence traces from stimulated (40 APs; 20 Hz,
1339 2 s) hippocampal neurons transduced with lentiviruses encoding shCTR, shmDia1 or both
1340 shmDia1 and shmDia3 combined (shmDia1+3). Data represent mean ± SEM. N = 4 independent
1341 experiments from n_{shCTR} = 17 videos, $n_{shmDia1}$ = 19 videos, $n_{shmDia1+3}$ = 18 videos. The corresponding
1342 endocytic decay constants are shown in Figure 1G.
1343 **(J)** Maxima of background-corrected vGLUT1-pHluorin fluorescence traces (surface normalized)
1344 for neurons transduced with shCTR (1.9 ± 0.1) or shmDia1+3 (1.9 ± 0.1) in response to 40 AP
1345 stimulation (20 Hz, 2 s). Data represent mean ± SEM. N = 22 independent experiments from n_{shCTR}
1346 = 105 videos and $n_{shmDia1+3}$ = 128 videos.**(K)** Averaged normalized vGLUT1-pHluorin
1347 fluorescence traces for neurons transduced with shCTR, shmDia1 or shmDia1+3 in response to 80
1348 AP stimulation (40 Hz, 2 s). Data represent mean ± SEM. N = 4 independent experiments from
1349 n_{shCTR} = 12 videos; $n_{shmDia1}$ = 15 videos; $n_{shmDia1+3}$ = 18 videos. Corresponding endocytic decay
1350 constants are shown in Figure 1H.
1351 **(L)** Maxima of background-corrected vGLUT1-pHluorin fluorescence traces (surface normalized)
1352 for neurons transduced with shCTR (2.8 ± 0.2), shmDia1 (2.6 ± 0.2), or shmDia1+3 (2.4 ± 0.1) in
1353 response to 80 AP stimulation (40 Hz, 2 s). Data represent mean ± SEM. N = 4 independent
1354 experiments from n_{shCTR} = 12 videos; $n_{shmDia1}$ = 15 videos and $n_{shmDia1+3}$ = 18 videos.

1355 **(M)** Minima of background-corrected vGAT-CypHer fluorescence traces (surface normalized) for
1356 neurons transduced with shCTR or shmDia1+3 (1.0 ± 0.2) in response to 200 AP stimulation (40
1357 Hz, 5 s). Data represent mean ± SEM. Values for shCTR were set to 1. N = 11 independent
1358 experiments from n_{shCTR} = 45 videos and $n_{shmDia1+3}$ = 42 videos.
1359 **(N)** Schematic representation of the activation of mDia1. Binding of RhoA-GTP to the RBD
1360 domain (green) or application of mDia1 activator (IMM) competes with the intramolecular
1361 interaction of the N-terminal DID (yellow) with the C-terminal DAD (red) domain (see Figure 3A
1362 for domain structure). The release of autoinhibition leads to dimerization of mDia formins in
1363 solution.
1364 **(O)** Maxima of background-corrected vGLUT1-pHluorin fluorescence traces (surface normalized)
1365 for neurons treated with 0.1 % DMSO (1.7 ± 0.1) or mDia activator (IMM; 1.6 ± 0.1) in response
1366 to 80 AP stimulation (40 Hz, 2 s). Data represent mean ± SEM. N = 3 independent experiments
1367 from n_{DMSO} = 18 videos; n_{IMM} = 16 videos.
1368
1369
1370
1371
1372

Figure 2 S1

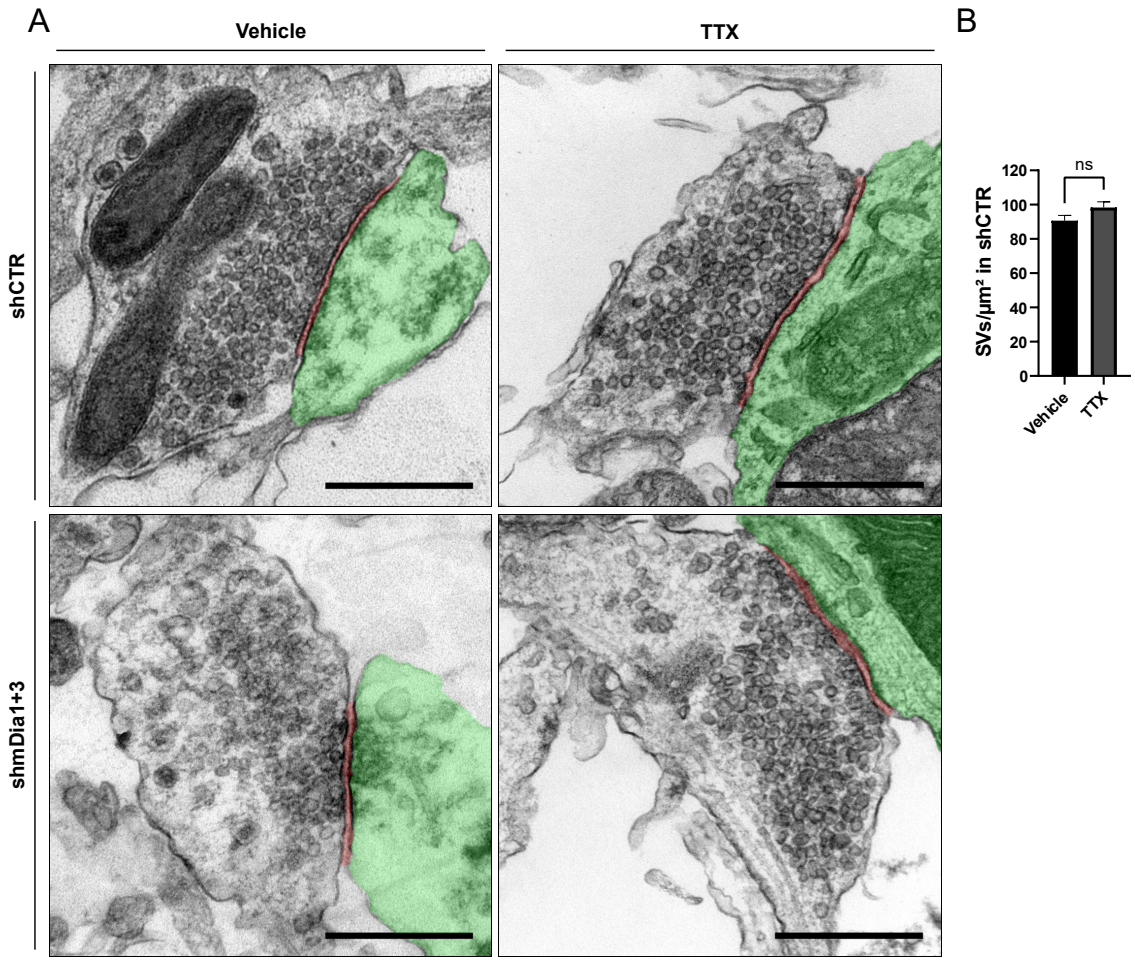

1373

1374 **Figure 2-Supplement 1 | SV depletion in mDia1/3-depleted neurons is activity dependent.**

1375 **(A)** Representative synaptic electron micrographs from neurons transduced with shCTR or

1376 shmDia1+3 and treated with 0.1% Vehicle or 1 µM TTX for 36 h before fixation. Postsynapse and

1377 postsynaptic cleft are colored in green and maroon, respectively. Scale bar, 250 nm.

1378 **(B)** Average number of SV per μm^2 in synaptic boutons of neurons transduced with shCTR and

1379 treated with 0.1 % Vehicle (A; 90.7 ± 3.1) or 1 µM TTX (B; 98.4 ± 3.3) for 36 h before chemical

1380 fixation. Data shown represent the mean ± SEM from two independent experiments and $n_{Vehicle}$ =

1381 180, n_{TTX} = 204 synapses.

1382

1383

Figure 3 S1

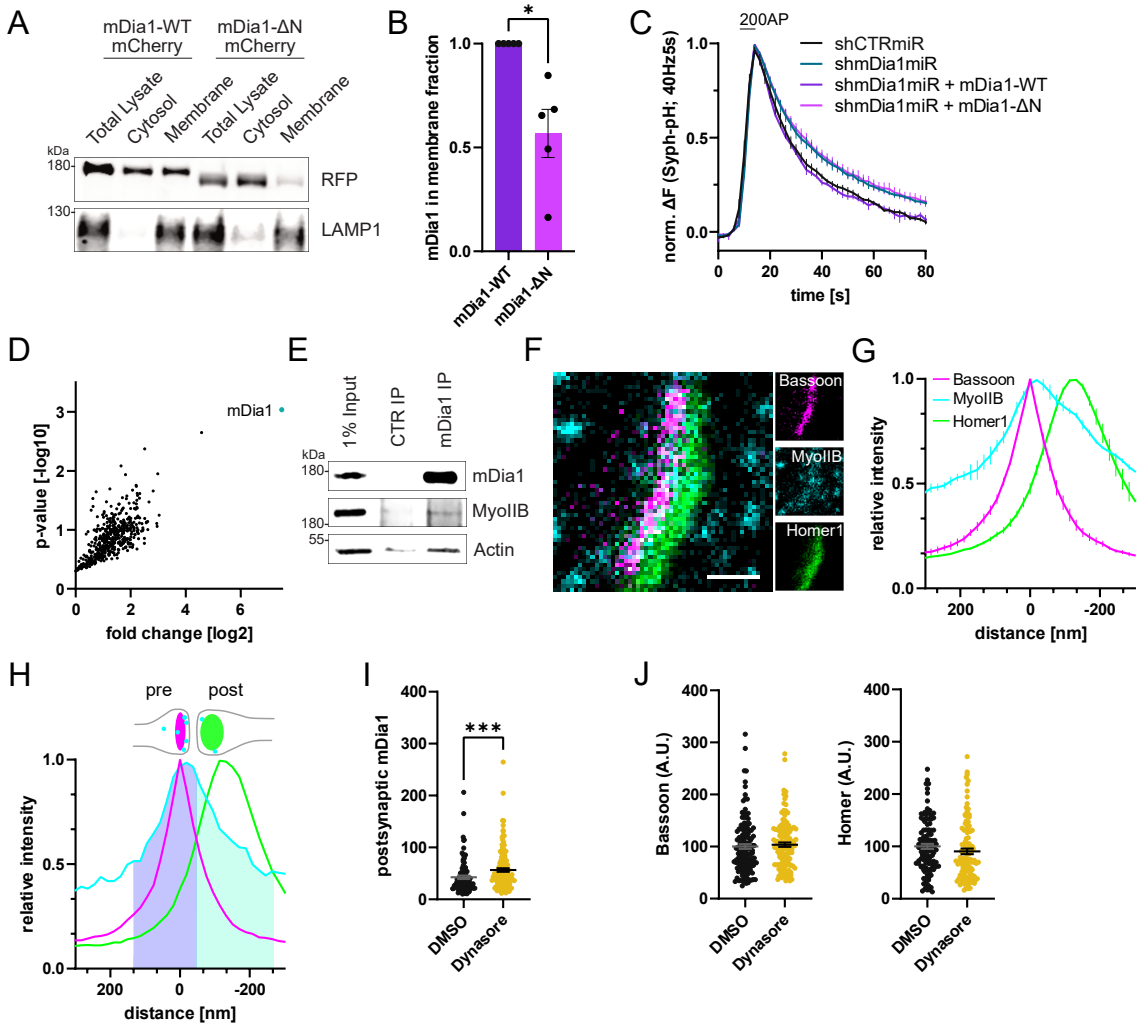

1384

1385 **Figure 3-Supplement 1 | mDia1 binds membranes and localizes to presynaptic endocytic sites.**

1386 **(A)** Membrane levels of mDia1-WT-mCherry versus mDia1-ΔN-mCherry proteins overexpressed

1387 in HEK293T cells. Membrane and cytosolic cellular fractions were isolated by ultracentrifugation

1388 and analyzed by immunoblotting with specific antibodies (LAMP1) and in-gel fluorescence of

1389 mCherry tags.

1390 **(B)** Densitometric quantification of mDia1-WT versus mDia1-ΔN (0.6 ± 0.1; $p < 0.05$, one sample

1391 t-test) membrane-associated protein levels. Data shown are normalized to mDia1-WT (set to 1)

1392 and expressed as mean ± SEM. Representative immunoblot is shown in A. N = 5 independent
1393 experiments.
1394 **(C)** Averaged normalized Synaptophysin-pHluorin fluorescence from stimulated (200 APs, 40 Hz,
1395 5s) hippocampal neurons transfected with shCTRmiR or shmDia1miR. For rescue experiments,
1396 neurons were co-transfected with plasmids encoding mDia1-WT-mCherry, mDia1-ΔN-mCherry
1397 or mCherry alone (shCTRmiR & shmDia1miR). Endocytic decay constants are shown in Figure
1398 3B.
1399 **(D)** Full volcano plot of proteins from Figure 3E associating with synaptic mDia1 analyzed by
1400 label-free proteomics of anti-mDia1 versus CTR immunoprecipitates from detergent-extracted
1401 mouse synaptosomes (P2' fraction). The cyan dot shows the specific enrichment of mDia1 as the
1402 bait protein of the immunoprecipitation ($p < 0.001$, two-tailed student's t-test). N = 3 independent
1403 experiments.
1404 **(E)** Endogenous co-immunoprecipitation of Myosin IIB by mDia1 from detergent-extracted
1405 mouse synaptosomes (P2' fraction). Samples were analyzed by immunoblotting using specific
1406 antibodies against mDia1, Myosin IIB (MyoIIB) and β-Actin.
1407 **(F)** Representative three-channel time-gated STED image of a synapse from hippocampal cultures
1408 fixed and immunostained for Bassoon (presynaptic marker, magenta), Myosin IIB (cyan) and
1409 Homer1 (postsynaptic marker, green). Scale bar, 250 nm.
1410 **(G)** Averaged normalized line profiles for synaptic distribution of Myosin IIB and Homer1 relative
1411 to Bassoon (Maximum set to 0 nm). Data are expressed as mean ± SEM. N = 3 independent
1412 experiments from n = 267 synapses.
1413 **(H)** Rationale for quantification of presynaptic protein levels of interest. The presynapse was
1414 defined by the normalized Bassoon distribution (purple fraction, cutoff at the crossection with the
1415 Homer1 profile) and corresponding absolute individual synaptic line profiles were integrated.

1416 **(I)** Postsynaptic F-Actin levels in synapses treated with 0.1% DMSO (42.6 ± 3.4) or 80 µM
1417 Dynasore (56.5 ± 3.3; $p < 0.001$, Mann-Whitney test) for 10 min before fixation from Figure 3C.
1418 Data shown are normalized to presynaptic DMSO values from Figure 3H (set to 100) and
1419 expressed as mean ± SEM. N = 3 independent experiments from n_{DMSO} = 92 synapses, $n_{Dynasore}$ =
1420 135 synapses.
1421 **(J)** Quantification of Bassoon and Homer1 levels in synapses treated with 0.1% DMSO (100.0 ±
1422 4.5 for Bassoon; 100.0 ± 4.3 for Homer1) or 80 µM Dynasore (103.7 ± 4.1 for Bassoon; 98.6 ±
1423 5.3) for 10 min before fixation. Data shown are normalized to DMSO values (set to 100) and
1424 expressed as mean ± SEM. N = 3 independent experiments from n_{DMSO} = 132 synapses, $n_{Dynasore}$ =
1425 128 synapses.
1426
1427
1428
1429

Figure 4 S1

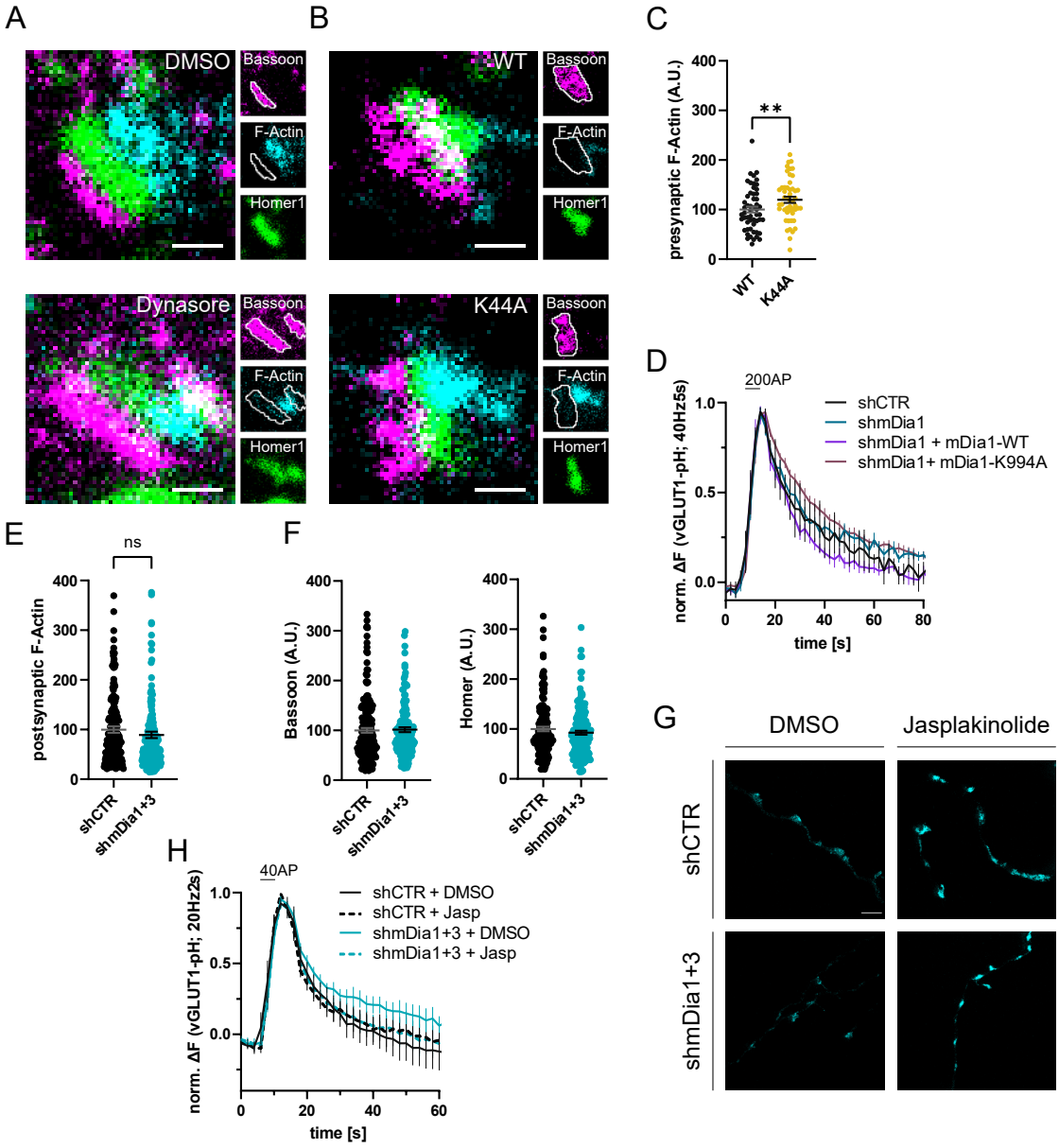

Figure 4-Supplement 1 | mDia1 regulates presynaptic actin and SV endocytosis.

(A) Representative three-channel time-gated STED images of synapses from hippocampal cultures treated with 0.1% DMSO or 80 µM Dynasore for 10 min. Cells were fixed and stained for Bassoon (magenta), F-Actin (cyan) and Homer1 (green). Scale bar, 250 nm. Corresponding analysis of presynaptic F-Actin levels is shown in Figure 4C.

1436 **(B)** Representative three-channel time-gated STED images of synapses from hippocampal cultures
1437 transduced with Dynamin1-WT or Dynamin1-K44A . Cells were fixed and stained for Bassoon
1438 (magenta), F-Actin (cyan) and Homer1 (green). Scale bar, 250 nm.
1439 **(C)** Presynaptic F-Actin levels in synapses from neurons transduced with Dynamin1-WT (100 ±
1440 5.9) or Dynamin1-K44A (119.8 ± 6.2, $p < 0.01$, one sample t-test) in B. Absolute line profiles of
1441 F-Actin overlapping with Bassoon (presynapse) distribution were integrated. Data shown are
1442 normalized to WT (set to 100) and expressed as mean ± SEM. n_{WT} = 54 synapses, n_{K44A} = 49
1443 synapses.
1444 **(D)** Averaged normalized vGLUT1-pHluorin fluorescence traces for neurons transduced with
1445 shCTR or shmDia1 in response to 200 AP (40 Hz, 5s) stimulation. For rescue purposes, cells were
1446 co-transduced with mDia1-WT-SNAP or mDia1-K994A-SNAP. Data are expressed as mean ±
1447 SEM. N = 6 independent experiments from n_{shCTR} = 21 videos; $n_{shmDia1}$ = 21 videos; $n_{shmDia1 + mDia1-}$
1448 $_{WT}$ = 16 videos; $n_{shmDia1 + mDia1-K994A}$ = 19 videos. Corresponding endocytic decay constants are
1449 shown in Figure 4D.
1450 (**E**) Postsynaptic F-Actin levels in synapses transduced with shCTR (100.0 ± 6.4) or shmDia1+3
1451 (89.3 ± 6.4) from Figure 4A,E. Data shown are normalized to shCTR values (set to 100) and
1452 expressed as mean ± SEM. N = 3 independent experiments from n_{shCTR} = 206 synapses, $n_{shmDia1+3}$
1453 = 135 synapses.
1454 **(F)** Quantification of Bassoon and Homer1 levels in synapses transduced with shCTR (100.0 ± 4.7
1455 for Bassoon; 100.0 ± 4.5 for Homer1) or shmDia1+3 (101.4 ± 4.8 for Bassoon; 92.4 ± 4.0). Data
1456 shown are normalized to DMSO values (set to 100) and expressed as mean ± SEM. N = 3
1457 independent experiments from n_{shCTR} = 158 synapses and $n_{shmDia1+3}$ = 159 synapses.
1458 **(G)** Representative STED images of endogenous β-Actin in vGLUT1 positive synapses in
1459 hippocampal neurons transduced with shCTR or shmDia1+3 and treated with 0.1 % DMSO or

1460 1 μM Jasplakinolide for 45 min. Neurons were co-transfected with pOrange-GFP-β-Actin knockin
1461 and vGLUT1-mCherry plasmids before fixation and immunostaining. Scale bar, 2.5 μm.
1462 **(H)** Averaged normalized vGLUT1-pHluorin fluorescence traces for neurons transduced with
1463 shCTR or shmDia1+3 in response to 40 AP (20 Hz, 2s) stimulation. Neurons were pre-incubated
1464 with 0.1 % DMSO or 1 μM Jasplakinolide (Jasp) for 30 min in the cell media before imaging.
1465 Data are expressed as mean ± SEM. N = 6 independent experiments from $n_{shCTR + DMSO}$ = 32 videos,
1466 $n_{shmDia1+3 + DMSO}$ = 35 videos, $n_{shCTR + Jasp}$ = 33 videos; $n_{shmDia1+3 + Jasp}$ = 34 videos. The corresponding
1467 endocytic decay constants are shown in Figure 4I.
1468
1469
1470

Figure 5 S1

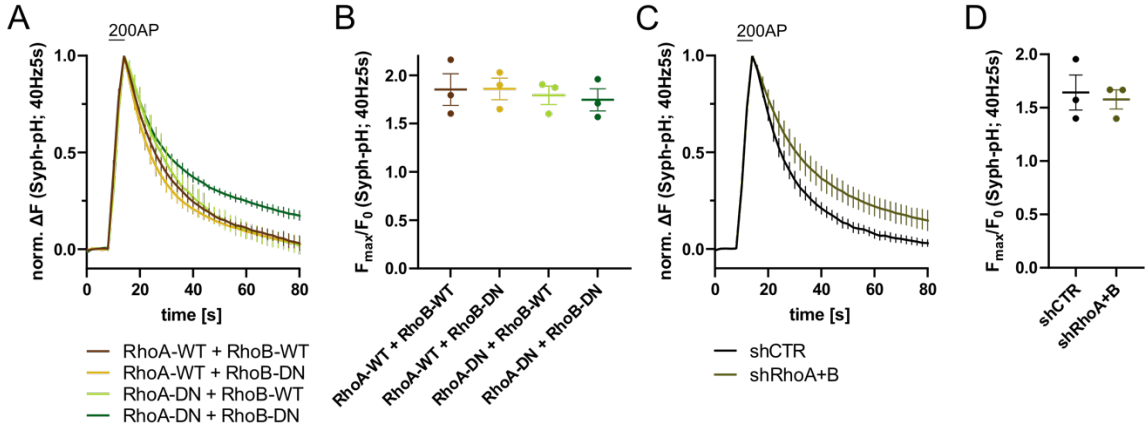

Figure 5-Supplement 1 | RhoA/B regulate SV endocytosis.

(A) Averaged normalized Synaptophysin-pHluorin fluorescence traces from stimulated (200 APs; 40 Hz, 5s) hippocampal neurons transfected with plasmids encoding the indicated combinations of WT or DN RhoA and RhoB variants. Data represent mean ± SEM. N = 3 independent experiments from $n_{RhoA\text{-}WT + RhoB\text{-}WT}$ = 21 videos, $n_{RhoA\text{-}DN + RhoB\text{-}WT}$ = 31 videos, $n_{RhoA\text{-}WT + RhoB\text{-}DN}$ = 23 videos, $n_{RhoA\text{-}DN + RhoB\text{-}DN}$ = 22 videos. Endocytic decay constants are shown in Figure 5D.

(B) Maxima of background-corrected Syph-pHluorin fluorescence traces (surface normalized) for neurons transfected with indicated combinations of WT or DN RhoA and RhoB variants (1.9 ± 0.2 for RhoA-WT + RhoB-WT; 1.9 ± 0.1 for RhoA-WT + RhoB-DN; 1.8 ± 0.1 for RhoA-DN + RhoB-WT; 1.7 ± 0.1 for RhoA-DN + RhoB-DN) in response to 200 AP stimulation (40 Hz, 5 s). Data represent mean ± SEM.

(C) Averaged normalized Synaptophysin-pHluorin fluorescence traces from stimulated (200 APs; 40 Hz, 5s) hippocampal neurons transfected with shRNA against no mammalian target (shCTR) or against RhoA and RhoB (shRhoA+B). Data represent mean ± SEM. N = 3 independent experiments from n_{shCTR} = 27 videos, $n_{shRhoA+B}$ = 25 videos.

1488 **(D)** Maxima of background-corrected Syph-pHluorin fluorescence traces (surface normalized) for
1489 neurons transfected with shCTR (1.6 ± 0.2) or shRhoA+B (1.6 ± 0.1) in response to 200 AP
1490 stimulation (40 Hz, 5 s). Data represent mean ± SEM.
1491
1492

Figure 6 S1

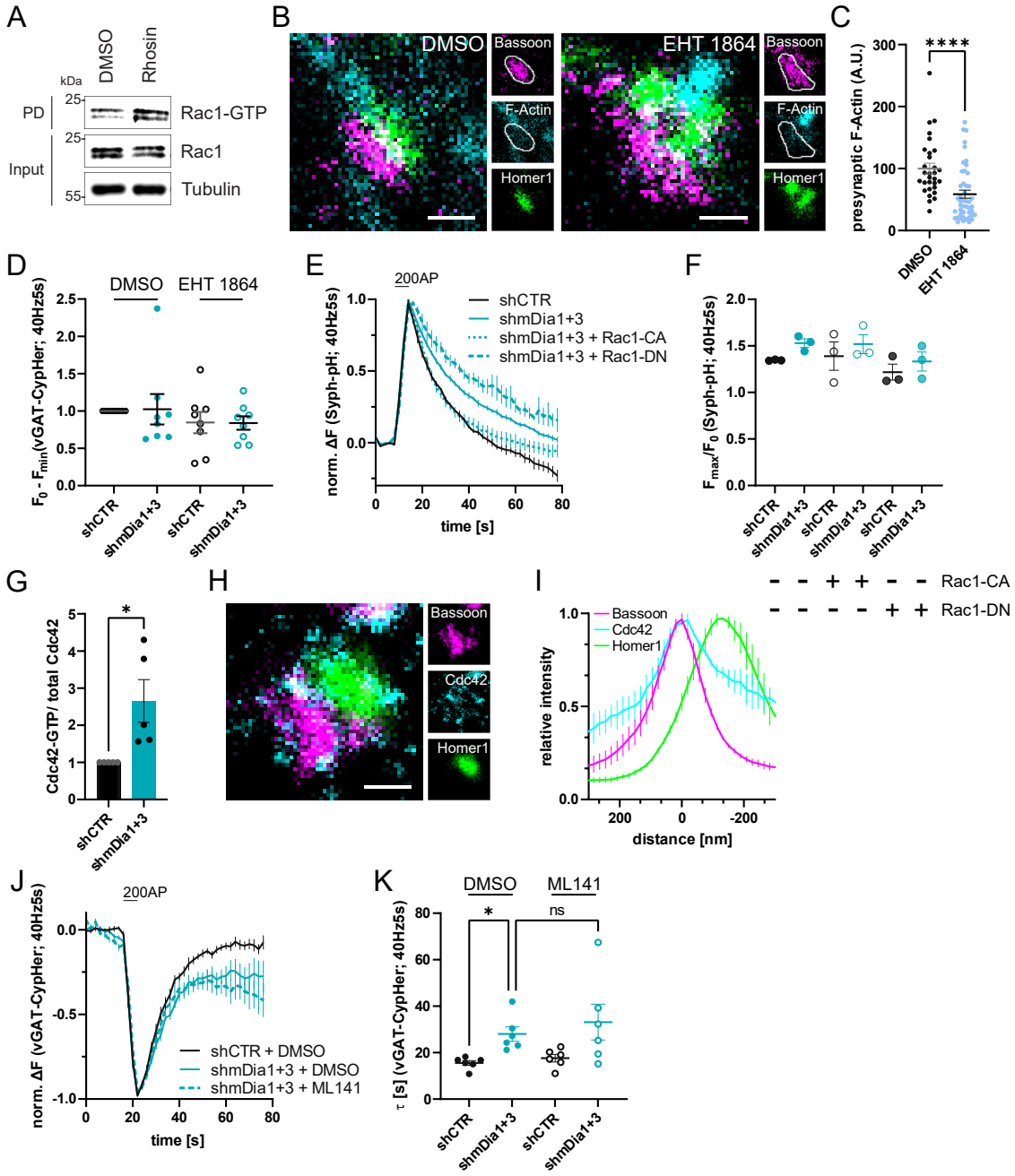

Figure 6-Supplement 1 | Cooperative action of mDia1/3 and Rac1 pathways in presynaptic endocytosis.

(A) Analysis of Rac1 activity by Rac1-GTP pulldown (PD) from whole-cell lysates (input) of mouse hippocampal cultures upon inhibition of Rho activity utilizing immobilized PAK as bait.

1498 Cells were treated with 0.1 % DMSO or 10 µM Rho Inhibitor (Rhosin) for 2 h before harvest.
1499 Samples were analyzed by immunoblotting for Rac1 and Tubulin using specific antibodies. Input,
1500 10% of material used for the pulldown. Contrast of pulldown and input blots was seperatly adjusted
1501 for visualisation purposes.
1502 **(B)** Representative three-channel time-gated STED images of synapses from hippocampal cultures
1503 treated with 0.1 % DMSO or 10 µM Rac1 Inhibitor (EHT 1864) for 2 h. Cells were fixed and
1504 stained for Bassoon (magenta), F-Actin (cyan) and Homer1 (green). Scale bar, 250 nm.
1505 **(C)** Presynaptic F-Actin levels in synapses of neurons treated with 0.1 % DMSO (100 ± 8.5) or
1506 10 µM Rac1 Inhibitor (EHT 1864; 58.6 ± 6.5; $p < 0.0001$, one sample Wilcoxon test) for 2 h. Line
1507 profiles of F-Actin overlapping with Bassoon (presynapse) distribution were integrated. Data
1508 shown are normalized to DMSO (set to 100) and expressed as mean ± SEM. $n_{DMSO} = 30$, $n_{EHT\ 1864}$
1509 = 46 from two independent experiments.
1510 **(D)** Minima of background-corrected vGAT-CypHer fluorescence traces (surface normalized) for
1511 neurons treated with 0.1 % DMSO (1.0 ± 0.2 for shmDia1+3) or 10 µM Rac1 Inhibitor (EHT 1864;
1512 0.8 ± 0.1 for shCTR; 0.8 ± 0.1 for shmDia1+3) in response to 200 AP stimulation (40 Hz, 5 s).
1513 Data represent mean ± SEM. Values were normalised to DMSO treated shCTR (set to 1). N = 8
1514 independent experiments from $n_{shCTR + DMSO} = 46$ videos, $n_{shmDia1+3 + DMSO} = 45$ videos, $n_{shCTR + EHT}$
1515 $_{1864} = 42$ videos, $n_{shmDia1+3 + EHT\ 1864} = 43$ videos.
1516 **(E)** Averaged normalized Synaptophysin-pHluorin fluorescence traces from stimulated (200 APs;
1517 40 Hz, 5s) hippocampal neurons transduced with lentiviruses encoding shCTR or shmDia1+3 and
1518 transfected with plasmids for expression of constitutively-active Rac1 (Rac1-CA; Q61L variant)
1519 or dominant-negative Rac1 (Rac1-DN; T17N variant). Data represent mean ± SEM. N = 3
1520 independent experiments from $n_{shCTR} = 12$ videos, $n_{shmDia1+3} = 23$ videos, $n_{shCTR + Rac1\text{-}CA} = 10$

1521 videos, $n_{shmDia1+3 + Rac1-CA}$ = 14 videos, $n_{shCTR + Rac1-DN}$ = 9 videos; $n_{shmDia1+3 + Rac1-DN}$ = 13 videos.
1522 The corresponding endocytic decay constants are shown in Figure 6H.
1523 **(F)** Maxima of background-corrected Synaptophysin-pHluorin fluorescence traces (surface
1524 normalized maximum values of traces shown in E) from stimulated (200 APs; 40 Hz, 5s)
1525 hippocampal neurons transduced with lentiviruses encoding shCTR (F_{max}/F_0 = 1.3 ± 0.0) or
1526 shmDia1+3 (F_{max}/F_0 = 1.5 ± 0.0) and transfected with plasmics encoding CA ($F_{max}/F_{0\ shCTR + Rac1-}$
1527 $_{CA}$ = 1.4 ± 0.2; $F_{max}/F_{0\ shmDia1+3 + Rac1-CA}$ = 1.5 ± 0.1) or DN versions (($F_{max}/F_{0\ shCTR + Rac1-DN}$ = 1.2 ±
1528 0.1; $F_{max}/F_{0\ shmDia1+3 + Rac1-DN}$ = 1.3 ± 0.1) of Rac1. Data represent mean ± SEM.
1529 **(G)** Densitometric quantification of Cdc42-GTP normalized to total Cdc42 levels in lysates from
1530 shmDia1+3 neurons (2.7 ± 0.6; $p < 0.05$, one sample t-test).Values for shCTR were set to 1. Data
1531 are expressed as mean ± SEM from N = 3 independent experiments.
1532 **H)** Representative three-channel time-gated STED image of a synapses from hippocampal mouse
1533 cultures, fixed and immunostained for Bassoon (magenta), Cdc42 (cyan) and Homer1 (green).
1534 Scale bar, 250 nm.
1535 **(I)** Averaged normalized line profiles for synaptic distribution of Cdc42 and Homer1 relative to
1536 Bassoon (Maximum set to 0 nm). Data are expressed as mean ± SEM (N = 3; n = 96 synapses).
1537 **(J)** Averaged normalized vGAT-CypHer fluorescence traces for neurons transduced with shCTR
1538 or shmDia1+3 in response to 200 AP (40 Hz, 5s) stimulation. Cells were acutely treated with 0.1
1539 % DMSO or 10 µM Cdc42 Inhibitor (ML141) in the imaging buffer. Data shown represent the
1540 mean ± SEM. N = 6 independent experiments from $n_{shCTR + DMSO}$ = 31 videos, $n_{shmDia1+3 + DMSO}$ =
1541 33 videos, $n_{shmDia1+3 + ML141}$ = 32 videos.
1542 **(K)** Endocytic decay constants of vGAT-CypHer traces in J: $\tau_{shCTR + DMSO}$ = 15.6 ± 1.0 s, $\tau_{shmDia1+3}$
1543 $_{+ DMSO}$ = 28.0 ± 3.1 s, $\tau_{shCTR + ML141}$ = 17.6 ± 1.6 s, $\tau_{shmDia1+3 + ML141}$ = 33.1 ± 7.7 s; $p_{shCTR + DMSO\ vs}$
1544 $_{shmDia1+3 + DMSO}$ < 0.01, Kruskal-Wallis test with Dunn's post-test. Data shown represent the mean

1545 ± SEM. N = 6 independent experiments from $n_{shCTR + DMSO}$ = 31 videos, $n_{shmDia1+3 + DMSO}$ = 33

1546 videos, $n_{shCTR + ML141}$ = 29 videos, $n_{shmDia1+3 + ML141}$ = 32 videos.

1547

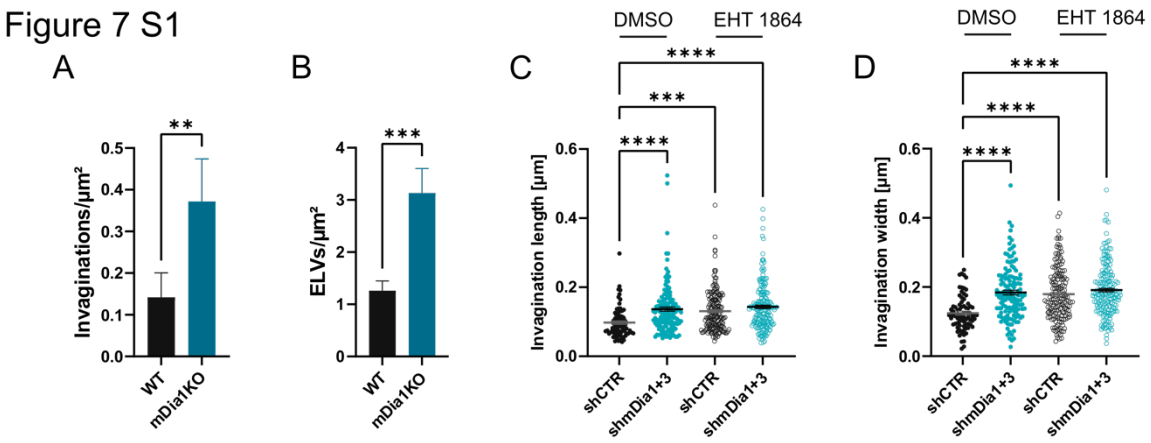

1548

1549

1550 **Figure 7-Supplement 1 | mDia1/3 and Rac1 cooperatively regulate the SV cycle and**

1551 **presynaptic ultrastructure.**

1552 **(A)** Average number of invaginations per μm^2 in WT (0.1 ± 0.1) and mDia1 KO (0.4 ± 0.1; $p <$

1553 0.01, Mann-Whitney test) boutons. Data shown represent the mean ± SEM from n_{WT} = 103

1554 synapses, n_{KO} = 96 synapses.

1555 **(B)** Average number of ELVs per μm^2 in WT (1.3 ± 0.2) and mDia1KO (3.1 ± 0.5; $p < 0.001$,

1556 Mann-Whitney test) boutons. Data shown represent the mean ± SEM from n_{WT} = 103 synapses,

1557 n_{KO} = 96 synapses.

1558 **(C)** Average invagination length in shCTR and shmDia1+3 boutons treated with 0.1 % DMSO

1559 (97.6 ± 4.5 nm for shCTR; 136.8 ± 6.0 nm for shmDia1+3, $p_{shCTR + DMSO \text{ vs } shmDia1+3 + DMSO} < 0.0001$)

1560 or 10 µM EHT 1864 (130.9 ± 4.5 nm for shCTR, $p_{shCTR + DMSO \text{ vs } shCTR + EHT\ 1864} < 0.001$; 143.1 ±

1561 4.9 nm for shmDia1+3, $p_{shCTR + DMSO \text{ vs } shmDia1+3 + EHT\ 1864} < 0.0001$, Kruskal-Wallis test with Dunn's

1562 post-test) for 2 h before chemical fixation. Data represent mean ± SEM from $n_{shCTR + DMSO}$ = 77

1563 invaginations, $n_{shmDia1+3 + DMSO}$ = 141 invaginations, $n_{shCTR + EHT\ 1864}$ = 176 invaginations, $n_{shmDia1+3}$

1564 $_{+ EHT\ 1864}$ = 189 invaginations.

1565 **(D)** Average invagination width in shCTR and shmDia1+3 boutons treated with 0.1 % DMSO
1566 (124.5 ± 5.6 nm for shCTR; 184.1 ± 6.6 nm for shmDia1+3, $p_{shCTR + DMSO \text{ vs } shmDia1+3 + DMSO} <$
1567 0.0001) or 10 µM EHT 1864 (179.0 ± 5.8 nm for shCTR, $p_{shCTR + DMSO \text{ vs } shCTR + EHT\ 1864} < 0.0001$;
1568 191.0 ± 5.4 nm for shmDia1+3, $p_{shCTR + DMSO \text{ vs } shmDia1+3 + EHT\ 1864} < 0.0001$, Kruskal-Wallis test with
1569 Dunn's post-test) for 2 h before chemical fixation. Data represent mean ± SEM from $n_{shCTR + DMSO}$
1570 = 77 invaginations, $n_{shmDia1+3 + DMSO}$ = 141 invaginations, $n_{shCTR + EHT\ 1864}$ = 176 invaginations,
1571 $n_{shmDia1+3 + EHT\ 1864}$ = 189 invaginations.
1572
1573